論文 / 著書情報
Article / Book Information

題目(和文)	弾性翼とロバスト制御器を有するハチドリ模倣羽ばたき飛行ロボットの開発
Title(English)	Development of a hummingbird-mimetic flapping-wing aerial robot with elastic wings and a robust controller
著者(和文)	Dang Jinqiang
Author(English)	Jinqiang Dang
出典(和文)	学位:博士(工学), 学位授与機関:東京工業大学, 報告番号:甲第12841号, 授与年月日:2024年9月20日, 学位の種別:課程博士, 審査員:田中 博人,鈴森 康一,山浦 弘,菅原 雄介,三浦 智
Citation(English)	Degree:Doctor (Engineering), Conferring organization: Tokyo Institute of Technology, Report number:甲第12841号, Conferred date:2024/9/20, Degree Type:Course doctor, Examiner:,,,,
学位種別(和文)	博士論文
Type(English)	Doctoral Thesis

Development of a hummingbird-mimetic flapping-wing aerial robot with elastic wings and a robust controller

August 19th, 2024

DANG JINQIANG

Department of Mechanical Engineering
School of Engineering
Tokyo Institute of Technology

Abstract

Hummingbirds exhibit remarkable flight capabilities, including hovering, backward and sideways flight, and vertical maneuvering. Annually, they undergo molting, sequentially replacing older feathers with new ones, progressing inward to outward. Despite the resultant reduction in wing area, they show an innate ability to adapt to such morphological changes, consistently maintaining their hovering and maneuvering proficiency. Various flapping-wing aerial robots, inspired by hummingbirds' extraordinary flight characteristics, have demonstrated their flight capabilities. However, mimicking hummingbirds' adaptability to molting (i.e., wing area loss) remains challenging. This is because a conventional PD or PID controller, paired with a control mechanism, is typically utilized in these robots to achieve stable attitude control. The morphological changes caused by wing area loss often render conventional PID controllers insufficient to maintain stable. Another challenge faced by flapping-wing aerial robots is the enhancement of their lift capacity, largely due to their inherent size and weight constrains. To address these challenges, this thesis presents the development of a hummingbird-mimetic flapping-wing aerial robot, equipped with a three-loop feedback controller featuring a disturbance observer and a biomimetic wing featuring a connecting membrane, aiming to enhance both robustness and lift capacity.

The development process was segmented into four distinct phases, each focusing on a specific aspect of the robot's design and functionality. The initial phase was dedicated to creating a compact and durable flapping mechanism. A rack-and-pinion mechanism, driven by a DC motor through a dual-layer planetary gear reducer with a reduction ratio of 16, was designed. This mechanism, characterized by its lightweight, compactness, and reliability, realized a flapping amplitude of 158°, establishing a solid foundation for the subsequent development phases. The subsequent phase concentrated on the development of a biomimetic wing featuring a connecting membrane. The biomimetic wing, with a surface area of 2103 mm^2, is composed of a polyurethane elastomer film made wing membrane and a 3D printed wing shaft. The connecting membrane, an extended elastomeric section located at the basal of the wing, was designed to softly limit passive feathering. It effectively augmented wing torsion by curbing feathering in the wing root chord in comparison

to a rigid stopper that limited the feathering rigidly. Integration of the connecting membrane resulted in a notable improvement in aerodynamic performance, achieving 24.2% higher efficacy and 8.4% higher lift at 24 Hz compared to wings using conventional rigid stoppers. In the third phase, the emphasis was on designing and implementing an attitude control mechanism based on wing modulation. The control mechanism is composed of three servo motors integrated into a 3D printed body frame. These servo motors manipulate the wing root bars to modulate the tension of wing membranes and the neutral positions of wing torsion, enabling the robot to produce control torques around its center of gravity (CoG) for roll, pitch, and yaw movements. The control mechanism produced a maximum roll, pitch, and yaw torques of 1.2 Nmm, 1.2 Nmm, and 1.3 Nmm respectively at the flapping frequency of 20 Hz. The final phase was centered around the development of an attitude controller employing a three-loop feedback structure to enhance robustness of the robot. A disturbance observer was integrated into the controller to enhance its responsiveness, accuracy, and robustness, enabling the robot to effectively counter against the external disturbances and maintain precise control, even when experiencing physical alterations. The effectiveness of this controller was assessed through semi-tethered experiments using a gimbal mechanism. The results demonstrated the controller's capabilities in maintaining stability and responsiveness, surpassing the performance of conventional PD and PID controllers.

In summary, this thesis introduced the development of a hummingbird-mimetic flapping-wing aerial robot that has a weight of 17.5 g and a wingspan of 185 mm. A notable aspect of this robot is the 8.4% improvement in lift capacity, achieved by integrating a connecting membrane into the biomimetic wing. The developed attitude controller, employing a three-loop feedback structure, effectively enhanced the robot's responsiveness, accuracy, and robustness in countering against external disturbances and maintaining precise attitude control. The findings and methodologies presented in this thesis provide insights into advancing the flight capabilities of hummingbird-sized flapping-wing aerial robots.

Contents

List of Figures

List of Tables

List of Symbols

A	Flapping amplitude (degrees)
L	Stroke length of the rack gear (mm)
D	Diameter of the pinion gear (mm)
F	Average lift (mN)
P	Input power (W)
η	Power efficacy (mN/W)
$\dot{\omega}$	Angular acceleration (rad/s²)
τ	Time constant
ω_c	Target angular velocity
ω	Angular velocity (rad/s)
Δ	Actual model uncertainty
$\hat{\Delta}$	Estimated model uncertainty
$\dot{\Delta}$	Derivative of model uncertainty
$\tilde{\Delta}$	Observer error of model uncertainty
$\dot{\tilde{\Delta}}$	Derivative of observer error
z	Auxiliary variable
$\dot{\omega}_c$	Derivative of target angular velocity
u	Controller output / Control input
θ_c	Target attitude angle (degrees)
$Gain_1$	First loop gain
$Gain_2$	Second loop gain
e	Attitude angle error (degrees)

K	Adaptive loop gain
T	Duration of one wingbeat cycle
t	A specific moment in one wingbeat cycle
Kp	Proportional gain
Kd	Derivative gain
Ki	Integral gain

List of Abbreviations

MAVs	Micro aerial vehicles
CoG	Center of gravity
PD	Proportional derivative
DC	Direct current
IMU	Inertial measurement unit
PET	Polyethylene terephthalate
AoA	Angle of attack
MCU	Microcontroller unit
PID	Proportional integral derivative
TD	Tracking differential
DOBC	Disturbance-observer-based control
CNC	Computer numerical control
PEEK	Polyether ether ketone
PET CF	Carbon fiber reinforced polyethylene terephthalate
PLA	Polylactide
CFRP	Carbon fiber reinforced plastic
UV	Ultraviolet
LFS	Low force stereolithography
3L-DOB	Three-loop feedback controller with a disturbance observer
RMS	Root mean square

IoT	Internet of things
Et al	Et alia

Chapter 1
Introduction

1.1 Background

Hummingbirds and insects exhibit a unique flight profile characterized by their ability to hover, fly backwards, and maneuver vertically, primarily due to their rapid wingbeat frequencies and figure-eight wing motion. This exceptional maneuverability is complemented by their capability for rapid direction changes, agility, and efficient energy use despite a high metabolic rate. The hummingbirds' flight mechanics are supported by strong pectoral muscles and precise control over wing strokes, allowing them to adjust wingbeat angles and speeds for intricate movements [1–6]. These attributes have made hummingbird flight a subject of keen interest in aerodynamics and robotics, inspiring the development of advanced flapping-wing aerial robots.

The idea of creating robots that mimic the flight of hummingbirds and insects emerged as part of the broader interest in biomimicry in robotics since late 20th century. The unique hovering and maneuvering capabilities of hummingbirds and insects, combined with their small size, made them an attractive model for roboticists seeking to develop new types of MAVs (micro air vehicles). Early efforts in developing hummingbirds-mimetic flapping-wing aerial robots involved understanding the biomechanics of their flight. Researchers studied the hummingbirds' wing motion, body dynamics, aerodynamics, and energy efficiency [7–10]. Initial prototypes, although crude, provided valuable insights into flapping-wing mechanics. Significant progress was made with the advent of advanced materials and miniaturization technologies from mid to late 2000s. Lightweight materials, such as carbon fiber and advanced polymers, enabled the construction of smaller, more agile prototypes. Miniaturized electronic components allowed for better control systems to be integrated into these robots [11–15]. Researchers focused on refining the aerodynamic models and improving the control systems for better stability and maneuverability since 2010s. This period saw the development of more sophisticated prototypes capable of stable hovering, agile maneuvers, and even backward flight [16–34]. The integration of advanced sensors and the development of autonomous flight capabilities became a key focus. This included the use of machine vision and other sensory technologies to enable the robots to navigate and perform tasks with minimal human intervention [35–38]. As the technology matured, these robots began to find applications in areas such as surveillance, pollination, environmental monitoring, and search-and-rescue

operations. Research continues to focus on improving endurance, energy efficiency, and autonomy, as well as scaling down the size of these robots even further.

The development of flapping-wing aerial robots is a multidisciplinary field that combines insights from various branches of science and engineering. Firstly, as mentioned above, the concept of flapping-wing robots is heavily inspired by the flight mechanisms of biological entities, particularly hummingbirds and insects. The intricate wing movements and flight patterns of these creatures have been studied extensively to understand the principles of flapping-wing aerodynamics. Fundamental research in aerodynamics, particularly in understanding the complex flow dynamics around flapping wings, forms a crucial part of the development of these robots. Then, The design and construction of micro flapping-wing aerial robots require advanced robotics knowledge. This involves the miniaturization of components, development of lightweight materials, and the creation of efficient mechanisms that can mimic the flapping motion. On the other hand, developing effective control systems for these robots is challenging due to the inherent instability and complexity of flapping-wing flight. Research in this area includes sensor integration for navigation and the development of algorithms for stable flight control. Besides that, the miniaturization of electronic components and the development of small, efficient power sources are critical for the practical deployment of these robots. This involves advancements in battery technology and microelectronic devices.

1.2 Flapping-wing aerial robots

A hummingbird-mimetic flapping-wing aerial robot typically weighs between 5 to 30 g and spans a wingspan of 100 to 300 mm. It comprises four essential components: flapping mechanism, artificial wing, control mechanism, and attitude controller. Each component is integral to the robot's functionality, collaboratively contributing to its stable flight. The flapping mechanism and artificial wing facilitate the replication of a hummingbird's distinctive wing movement, while the control mechanism and attitude controller are critical for maintaining balance and navigating the aerial environment effectively.

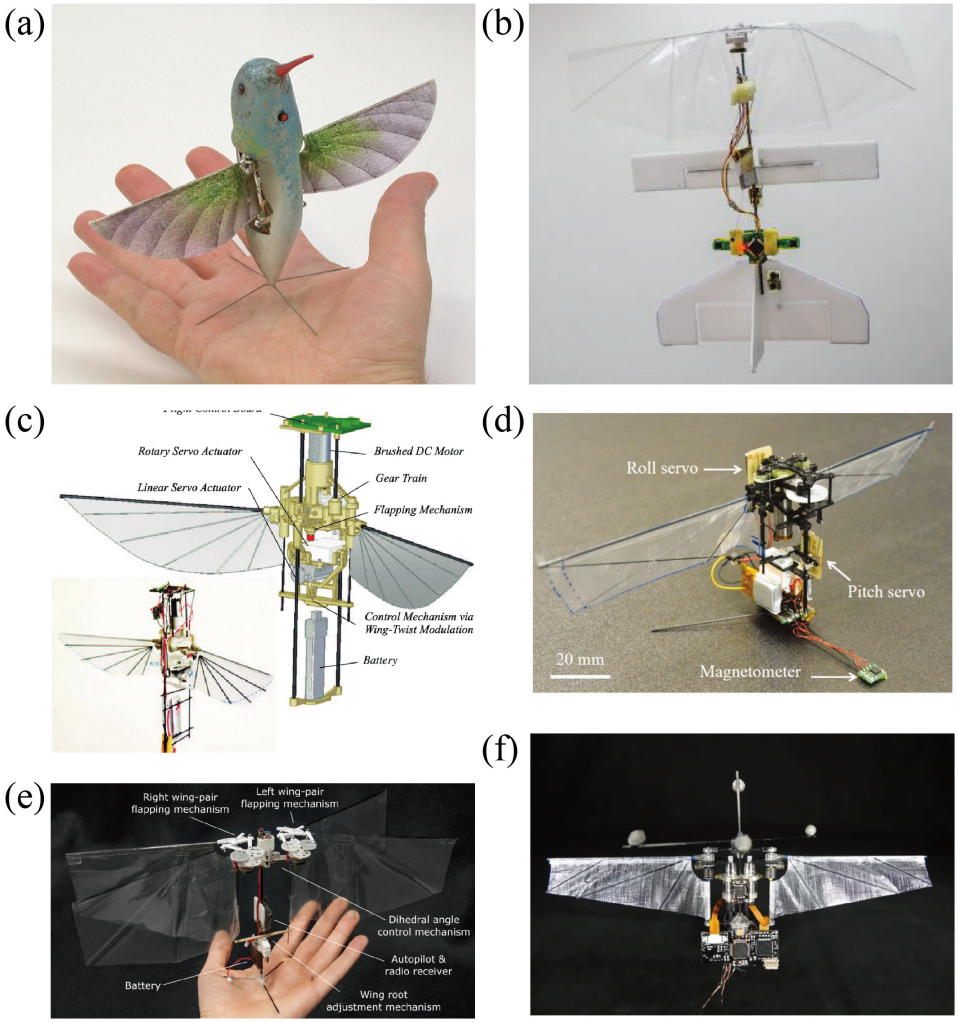

Figure 1.1 Flapping-wing aerial robots developed in previous studies. (a) Nano hummingbird [16], (b) Delfly Explorer [37], (c) COLIBRI [25], (d) KUBeetle-S [21], (e) Delfly Nimble [19], (f) Purdue hummingbird robot [23].

Various flapping-wing aerial robots have been developed in recent years. Among them, the Nano Hummingbird (Figure 1.1 (a)), developed by Keennon *et al*. [16], stands out with its 165 mm wingspan and 19 g weight. It is capable of hovering for extended periods, achieving forward flight speeds of up to 6.7 m/s, and transmitting live color video to a remote station. Significantly, the Nano Hummingbird has marked a milestone in the development of tailless flapping-wing aerial robots, showcasing the practicality of achieving precise hovering capabilities.

The Delfly Explorer (Figure 1.1 (b)), developed by G.C.H.E. de Croon *et al*.

[37], weighs approximately 20 g and has a wingspan of about 280 mm. It is distinct for its autonomous flight capabilities, facilitated by onboard systems including cameras and sensors for navigation and obstacle avoidance. Its design, inspired by the flight mechanics of insects like dragonflies, allows for exceptional agility and maneuverability, enabling it to navigate through tight spaces with ease. Additionally, its lightweight and soft-winged design enhance its safety for use in close proximity to people. The extended battery life and advanced control system make it ideal for applications such as indoor surveillance, inspection of confined spaces, and environmental monitoring, showcasing an innovative blend of stability, agility, and efficiency.

The COLIBRI (Figure 1.1 (c)), developed by Ali *et al*. [25], has a weight of 22 g and a wingspan of 210 mm. It can fly at the flapping frequency of 22 Hz and incorporates an innovative wing tension modulation mechanism for active stabilization in pitch and roll, active control in the yaw axis is lacked, relying instead on passive stability. This mechanism effectively alters the lift vector relative to the robot's CoG (center of gravity). The robot is equipped with a control board that employs a closed-loop PD (proportional derivative) controller for stability adjustments and demonstrated a hovering flight of 15–20 seconds, powered by an onboard battery.

The KUBeetle-S (Figure 1.1 (d)) is a tailless, hover-capable flapping-wing aerial robot developed by Phan *et al*. [21]. It has a weight of 21 g and a wingspan of 156 mm, capable of hovering utilizing a low-torque control mechanism that simultaneously modulates the stroke plane and wing torsion for pitch and roll controls, yaw control was achieved by asymmetrically modulating wing torsion. A 3.5 g DC (direct current) coreless motor, reduced via a gearbox, drives a pulley-string mechanism for wing actuation. Its onboard control system successfully demonstrated controlled hovering flight for about 3 minutes.

Delfly Nimble (Figure 1.1 (e)) [19] is a flapping-wing aerial robot designed to mimic the flight maneuvers of flies, particularly focusing on rapid banked turns. The robot, weighing 28.2 g with a 330 mm wingspan, employs a bio-inspired flapping mechanism with flexible wings, capable of clapping and peeling for enhanced thrust, akin to the clap-and-fling mechanism seen in nature. Its wing morphology and kinematics are optimized for power efficiency, driven by miniature brushless DC motors. It generates control torques and thrust across three orthogonal

body axes by varying wingbeat patterns, such as changing wing root angles for yaw control, adjusting dihedral angles for pitch, and creating thrust differentials between wings for roll. This robot, equipped with an onboard autopilot for attitude control, demonstrated exceptional agility comparable to natural flyers and is capable of autonomously performing complex maneuvers like rapid banked turns, offering new insights into the aerodynamics and control strategies of flying insects.

The Purdue hummingbird robot (Figure 1.1 (f)) [22–24], with a wingspan of 170 mm and a weight of 20.4 g, mimics the flight kinematics of hummingbirds. Each wing, powered by a DC motor, is capable of independent motion. A pair of reduction gears and torsional springs are integrated for efficient torque transmission and kinetic energy restoration. The wing rotation is passive, influenced by aerodynamic and inertial loading, while the stroke motion is actively controlled. The onboard system includes motor drivers, a STM32 microcontroller, an IMU (inertial measurement unit), and a power circuit, ensuring stability during untethered flight through feedback control.

The details of each component of the flapping-wing aerial robots are introduced in the following sections.

1.2.1 Flapping mechanism

The flapping mechanism is designed to convert the actuator's motion into the reciprocal flapping movement of the wings, emulating the flapping motion of birds and insects through technical and engineering methods. Over time, a diverse range of actuators and flapping mechanisms have been developed, each tailored to mimic the natural wing movements. These innovations reflect ongoing advancements in understanding and mimicking the complex biomechanics of flapping-wing creatures.

A coreless DC motor is commonly used to drive the flapping mechanism. The Nano Hummingbird [16] employs a DC motor to power a string-based flapping mechanism, as illustrated in Figure 1.2 (a). This design achieves a flapping frequency of 33 Hz and an amplitude of 200° while being lighter and more compact compared to flapping mechanisms that use dual-levers, making it particularly advantageous for small-scale flapping-wing robots. Nonetheless, the system's reliance on precise string tension and alignment renders it sensitive to adjustments and calibrations, presenting potential challenges in maintaining optimal performance during regular operation. A similar mechanism was used in [73].

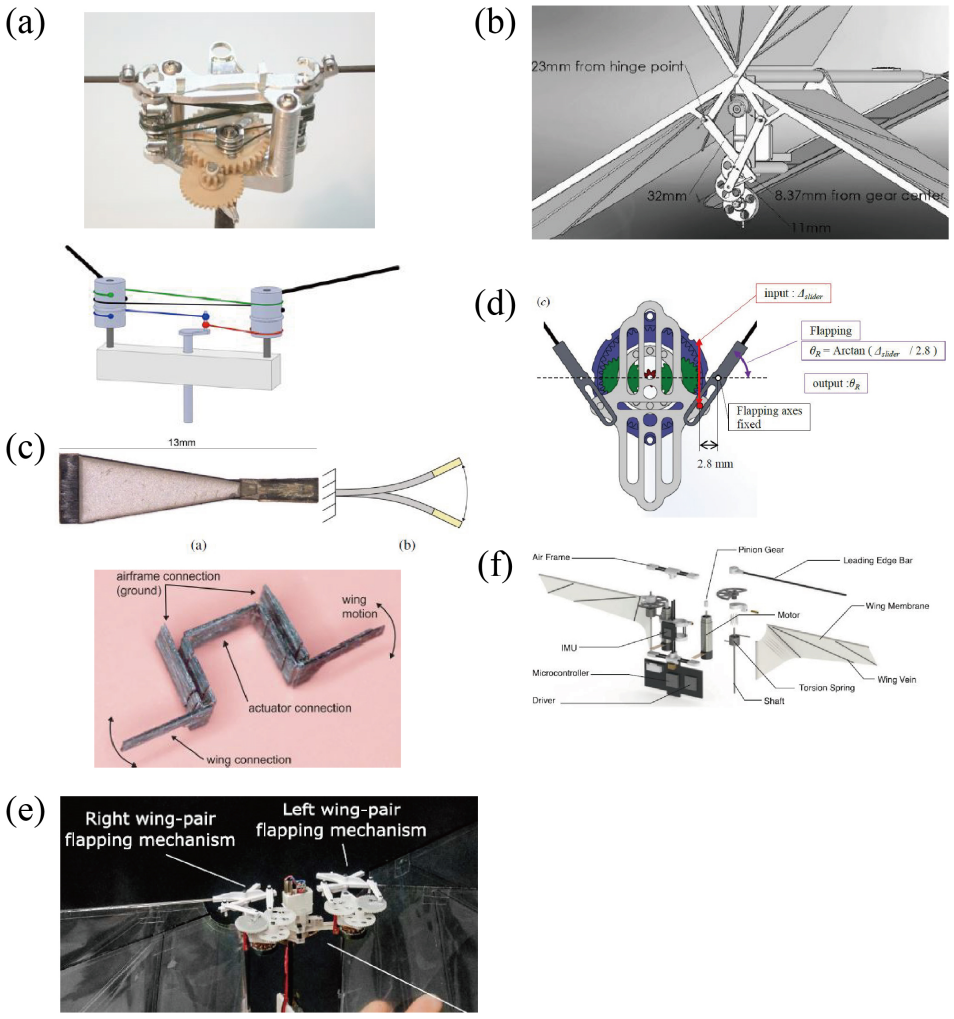

Figure 1.2 Flapping mechanisms developed in previous studies. (a) String-based flapping mechanism [16], (b) Crank-shaft-based flapping mechanism [15], (c) Dual-lever-based flapping mechanism with piezoelectric actuator [14], (d) Pin-slot-based flapping mechanism [39], (e) Dual-crank-shaft-based flapping mechanism [19], (f) Flapping mechanism based on motor control [22].

The Delfly Micro [15] employs a crank-shaft-based flapping mechanism (Figure 1.2 (b)), powered by a DC motor, which accomplishes a flapping frequency of 30 Hz. Characterized by its simplicity and reliability, this mechanism offers advantages in terms of ease of manufacturing and maintenance. However, one notable limitation of this design is its challenge in achieving a large flapping amplitude. While it excels in operational consistency and robustness, the crank-

shaft-based mechanism inherently restricts the extent of wing movement, thereby limiting the amplitude of the flapping motion.

The Robobee [14] employs a piezoelectric actuator in conjunction with a dual-lever mechanism to achieve wing flapping (Figure 1.2 (c)), attaining a frequency of 120 Hz and an amplitude of 110°. The utilization of piezoelectric materials is the key in this design, allowing the conversion of electrical energy into mechanical motion with high efficiency, bypassing the need for gears and thereby reducing gear losses. These materials are advantageous due to their lightweight, compact nature, and simplicity, which contribute to a reduction in the overall complexity and number of moving parts. However, the use of piezoelectric actuators has its limitations. They typically produce smaller displacements, which may result in lower force generation and reduced wing stroke amplitude compared to larger, more powerful actuators. This limitation can impact the payload capacity and restrict the range of flight. Furthermore, piezoelectric materials have a certain fragility and may be more susceptible to damage from impacts or adverse environmental conditions than other types of actuators. Temperature sensitivity is another factor to consider with piezoelectric actuators. Changes in temperature can affect the consistency of wing flapping, potentially impacting the robot's performance in various environmental conditions. Additionally, the efficiency and effectiveness of piezoelectric actuators can diminish if they are scaled significantly away from their optimal size. This scaling challenge limits the range of sizes in which these actuators can be effectively utilized, potentially restricting their application in varying dimensions of robotic design.

Kitamura *et al*. [39] developed a pin-slot-based flapping mechanism, as depicted in Figure 1.2 (d). Distinct from other mechanisms, this design incorporates a single-layer planetary gear reducer, which contributes to a more compact form factor of the robot. However, this mechanism has its limitations. One of the primary constraints is that the maximum gear ratio and flapping amplitude are limited by the weight and size of the components. In the quest to maintain a compact and lightweight design, there is a trade-off in the range of motion and power transmission capabilities.

The Delfly Nimble [19] and the Purdue hummingbird robot [22] both feature a design where independent motors, each linked to a gear reducer, power their wings as shown in Figure 1.2 (e) and (f). This unique setup allows for the independent

control of both the flapping amplitude and frequency for each wing. Such autonomy is essential for performing complex maneuvers and is critical for mimicking the intricate flight patterns observed in birds and insects. This capability is instrumental in achieving the high level of agility that is characteristic of natural fliers. However, this design approach introduces certain challenges that need to be addressed. One of the primary issues is the increased mechanical complexity that comes with having separate motors for each wing. This complexity not only poses potential difficulties in terms of maintenance and reliability but also increases the risk of unbalanced forces. If the synchronization between the two motors is not meticulously maintained, it could lead to asymmetrical wing movements, adversely affecting the robot's stability and maneuverability. Moreover, utilizing two motors inherently adds to the overall weight of the robot and increases its energy consumption. This added weight and higher energy requirement can negatively impact the robot's flight duration and efficiency. For a flapping-wing robot, where energy efficiency and lightweight design are paramount, this can be a significant drawback. Another challenge lies in the control aspect. Managing the independent movements of each wing requires advanced and sophisticated control algorithms. These algorithms must not only ensure precise coordination between the wings but also need to be adaptable to varying flight conditions. This complexity adds to the software and hardware demands of the system, making the design and operation of such robots more intricate.

1.2.2 Artificial wing

The design of artificial wings for flapping-wing aerial robots is a complex endeavor, significantly challenged by the unsteady dynamic characteristics of these robots. This process necessitates meticulous attention to both structural and aerodynamic factors to ensure optimal performance. Key considerations include the airfoil camber, wing twist, overall mass, and the effective modulation of lift and drag for attitude control. Typically, an artificial wing is comprised of two main components: a flexible membrane and a supporting frame. This dual-structure approach allows for a combination of rigidity where needed and flexibility where it is most beneficial, mimicking the natural mechanics of birds and insects wings. The size and shape of the wings are varied, catering to different flight requirements and robot specifications. Each design choice in terms of wing geometry directly impacts the robot's aerodynamic efficiency and maneuverability. Furthermore, the choice of

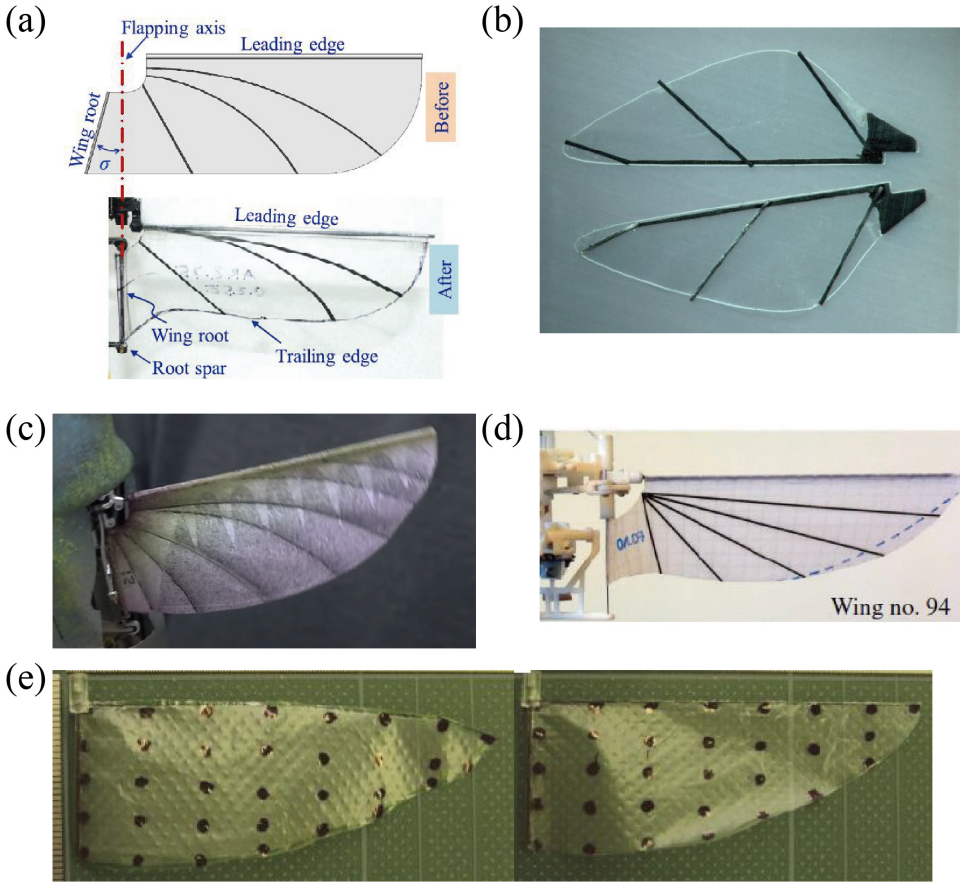

Figure 1.3 Artificial wings developed in previous studies. (a) Wing made of carbon rods and PET film [20], (b) Artificial wing made of carbon fiber and polymer film [14], (c) Artificial wing made of carbon fiber and a flexible membrane [16], (d) Artificial wing made of carbon fiber and Polyester film [25], (e) Artificial wing made of CFRP rods and polyethylene film [40].

materials for both the membrane and the frame is crucial, as different materials exhibit varying levels of flexural stiffness. This variability in stiffness significantly influences the aerodynamic performance of the wings. Materials with higher flexural stiffness can offer more consistent and predictable aerodynamic responses, but might not provide the necessary flexibility for certain flight maneuvers. On the other hand, materials with lower stiffness can enable more dynamic wing movements but might compromise on stability and control.

Phan *et al*. [20] developed an artificial wing comprising a frame constructed from carbon rods and a membrane made of PET (polyethylene terephthalate) film

(Figure 1.3 (a)). To enhance its structural integrity, a layer of carbon prepreg is attached to the wing membrane, serving as reinforcement. Dimensionally, the wing spans approximately 70 mm in length and 30 mm in width, making it well-suited for a miniature flapping-wing aerial robot. Despite its robust construction, the wing is remarkably lightweight, weighing around 0.2 g. This low weight is critical for maintaining the overall efficiency and maneuverability of the robot. A distinctive feature of this wing design is the extended trailing edge of the membrane. This extension allows the wing to deform during the flapping motion, creating a camber angle of about 15°. This camber is significant for generating lift during flight. Additionally, the wing is designed to maintain a low geometric AoA (Angle of Attack), approximately 40°.

The wings used in Robobee [14] are designed to mimic the structure of insect wings, utilizing carbon fiber as a frame and a polymer film as a membrane (Figure 1.3 (b)). These wings, fabricated through a precise laser-micromachining process, are structured with rigid “veins” aligned in a predetermined pattern and adhered to a 1.5 μm thick polymer sheet, replicating the reinforcement structure seen in most insect wings. Each wing weighs approximately 400 mg, measures 15 mm in length, and is characterized by its exceptional strength-to-weight ratio.

The Nano Hummingbird’s wings feature a flexible membrane (Figure 1.3 (c)) [16], made of a lightweight and durable synthetic material, designed to passively deform during flight. Supporting this membrane is a carbon fiber structural framework, consisting of spanwise main spars and chordwise root spars, chosen for its high strength-to-weight ratio. Each wing measures 74 mm in length and about 30 mm in width, dimensions that are critical for achieving the desired aerodynamic efficiency and flight capabilities of the robot.

COLIBRI’s wing structure closely resembles that of the KUBeetle-S, featuring wings reinforced with carbon strips or bars for necessary stiffness and shape retention while maintaining flexibility essential for flapping (Figure 1.3 (d)) [25]. The wing membrane, initially crafted from Mylar film and later upgraded to Polyester (Icarex) in the final version, was selected for its lightness and compatibility with flapping motions. A notable design aspect is the wings’ cambered structure, achieved passively through a 16° inherent angle between the leading and root edge bars. Each wing spans 90 mm in length and 25 mm in width, with an approximate weight of 0.24 g, balancing size, weight, and aerodynamic

efficiency for optimal flight performance.

Tanaka *et al*. [40] conducted a study exploring how variations in wing membrane tension and leading edge shape impact lift generation in artificial wings. They crafted and tested four different wing designs, combining either curved or straight leading edges with loosened or tightly fit membranes (Figure 1.3 (e)). All wings shared the same length of 70 mm and width of 25 mm, but differed in wing area and weight. Their findings revealed that a loosened membrane enhances lift by increasing the wing area and promoting greater feathering deformation. Additionally, they discovered that a curved leading edge also boosts lift generation. Notably, the wing design featuring both a curved leading edge and a loosened membrane was the most energy-efficient, requiring the least electrical power to generate the same amount of lift compared to the other variants.

1.2.3 Control mechanism

Flapping-wing aerial robots feature a control mechanism enabling them to mimic the agility and precision of hummingbirds or insects in flight. This mechanism is distinct from those used in traditional fixed-wing or rotary-wing aircraft, largely due to the unique dynamics of flapping flight. Unlike fixed-wing aircraft which maneuver using ailerons, or rotary-wing aircraft that adjust rotor blade pitch, flapping-wing robots achieve control by modulating the motion of their wings. This modulation involves adjustments in flapping amplitude, frequency, wing tension, and AoA throughout the wingbeat cycle. To facilitate these sophisticated control strategies, the robots are equipped with a variety of actuators and mechanical systems such as servo motors, gears, and linkages. These components are designed to modulate wing deformations in response to control signals, enabling the agile flight behaviors of these robots.

Two types of control mechanisms have been developed for flapping-wing aerial robots. The first type employs a tail wing to achieve active attitude control and passive stabilization, as seen in Mentor [13], Delfly Micro [15], Delfly Explorer [18], and the robot developed by Park *et al*. [41]. While employing a tail wing offers several advantages, it also presents certain trade-offs. On the plus side, a tail wing greatly enhances stability, particularly in forward flight, by providing extra lift and control surfaces for pitch and yaw adjustments. Additionally, with a tail wing handling some aspects of flight control, the main wings can be optimized more for lift and propulsion rather than for multifaceted control, potentially simplifying their

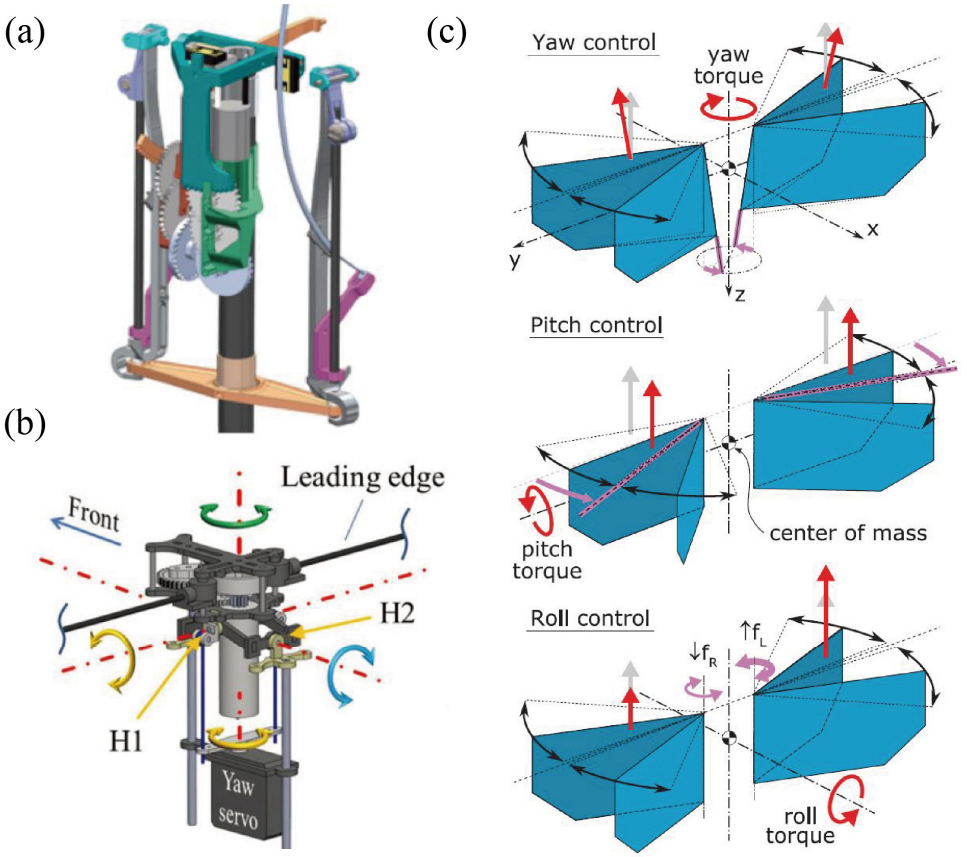

Figure 1.4 Control mechanisms developed in previous studies. (a) Control mechanism modulating wing tension and neutral positions of wing torsion [16], (b) Control mechanism modulating wing stroke plane and wing tension [21], (c) Control mechanism modulating flapping frequency, mean stroke angle, and wing tension [16].

design and mechanics. However, while tail wings enhance stability, they can sometimes reduce overall maneuverability, which is a drawback of the tail wings. The second type is tailless, relying solely on wing modulation for stabilization and maneuvering. The tailless approach enhances maneuverability, allowing flapping-wing aerial robots to execute rapid and agile maneuvers similar to those of real hummingbirds and insects. Additionally, the absence of a tail wing results in a more compact design, advantageous for operations in confined spaces and facilitating ease of transport and deployment. However, controlling a tailless robot presents its own set of complexities. Achieving stabilization and maneuverability solely through wing modulation requires advanced control algorithms and highly precise

wing movements, posing significant implementation challenges. Moreover, without a tail wing, maintaining stability typically involves continuous and demanding adjustments in wing motion, placing considerable strain on the control system and increasing the complexity of flight dynamics.

Nano Hummingbird [16] employs a control mechanism featuring three servo motors to manipulate the movement of the wing root spars (Figure 1.4 (a)), and thus modulate the tension in the wing membranes and the neutral positions of the wing torsion to generate roll, pitch, and yaw torques. KUBeetle-S [21] simultaneously modifies the wing stroke plane and wing tension for pitch and roll controls, and asymmetrically modulates the wing root spars for yaw control (Figure 1.4 (b)). Delfly Nimble [19] manipulates the flapping frequencies of the left and right wings independently for roll control. Additionally, pitch and yaw controls are realized by shifting the mean stroke angle and asymmetrically modulating wing tension, respectively (Figure 1.4 (c)). This control mechanism allows it to perform agile maneuvers and replicate the complex flight dynamics observed in biological insects, particularly in terms of rapid banked turns and directional changes. Purdue hummingbird robot [22] relies entirely on the independent modulation of each wing's kinematics for attitude control. Pitch control is realized by shifting the mean stroke angle for both wings, causing the robot to tilt forward or backward. Roll control is achieved through asymmetric flapping amplitudes, resulting in the robot rolling to either side. Yaw control is managed by adjusting the phase difference between the wings' flapping cycles, enabling rotation around the vertical axis. This control scheme, facilitated by an onboard MCU (microcontroller unit) and IMU, allows the robot to hover stably.

1.2.4 Attitude controller

The attitude controller in flapping-wing aerial robot is an important component that coordinates the intricate movements necessary for flight. Implementing an appropriate controller needs to consider various factors, including the robot's size, intended function, and the precision needed in flight control. PID (proportional integral derivative) controllers are widely used for their simplicity and efficacy in ensuring stable flight. A PID controller operates by modifying control inputs to reduce the discrepancy between desired and actual flight parameters, including position, velocity, and orientation, thus playing a key role in maintaining consistent and controlled flight dynamics in the complex robotic system. For advanced

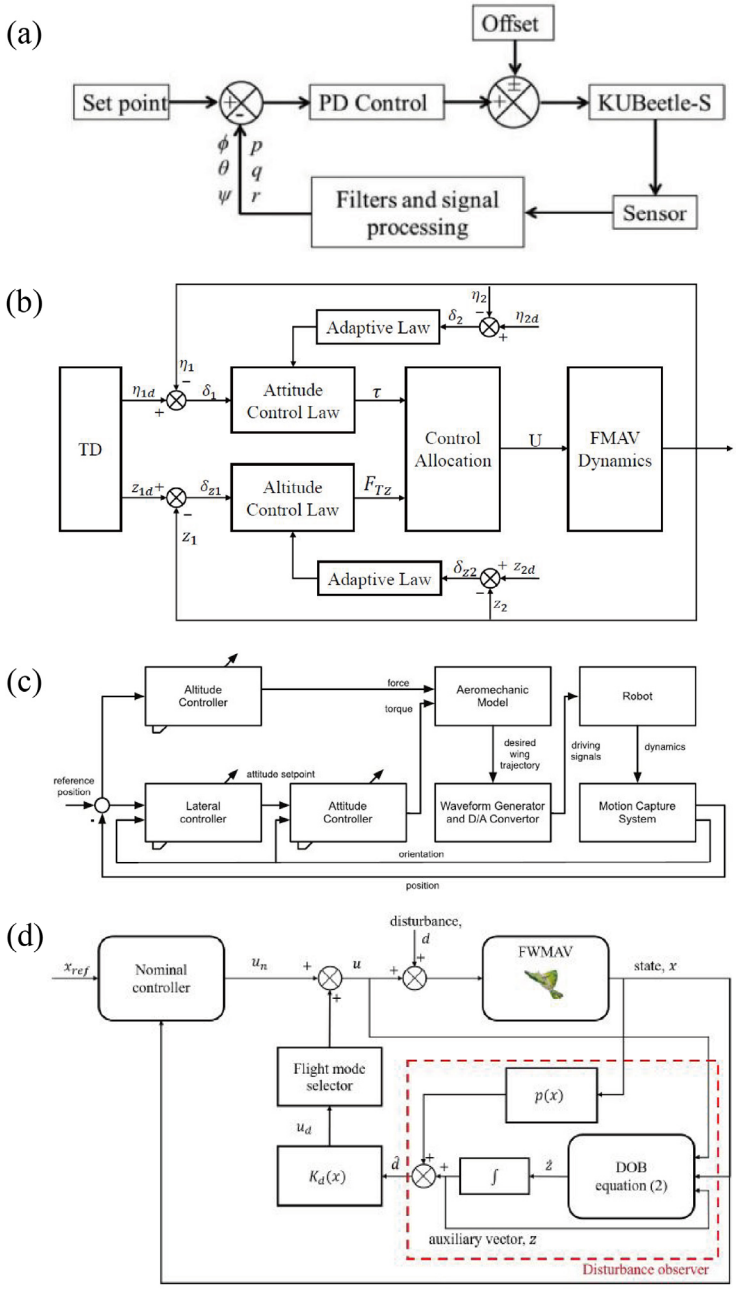

Figure 1.5 Block diagrams of attitude controllers developed in previous studies. (a) PD controller [19], (b) Adaptive controller with TD [44], (c) Adaptive controller using Lyapunov function candidates [45], (d) Adaptive controller using DOBC [47].

autonomy and adaptive flight capabilities, some controllers based on neural

networks were also developed [42, 43]. They are particularly useful for navigating complex environments or learning new flight maneuvers. For manually piloted or semi-autonomous robots, remote control systems are often used. These systems usually include a ground-based transmitter and an onboard receiver, with the pilot providing commands directly. For example, Nano hummingbird [16] is manually operated but the body attitude during flight is stabilized by a closed-loop control algorithm. Its flight controller consists of a 3-axis gyroscope sensor, a MCU, a transmission receiver, and a motor driver circuit to achieve stable hovering in both indoor and outdoor environments. The KUBeetle-S [20, 21] achieves stable with an onboard 9-axis IMU including 3-axis gyroscope, 3-axis accelerometer, and 3-axis magnetometer through a conventional PD feedback controller (Figure 1.5 (a)). Delfly Nimble [19] utilizes a custom-designed, 2.8 g onboard autopilot system. The heart of the control system is a lightweight and compact programmable MCU capable of processing inputs from various sensors and executing the control algorithms necessary for flight. A 3-axis accelerometer and gyroscope were used for attitude estimation. In addition to being operated remotely, the autopilot is capable of executing preprogrammed control sequences, which can be initiated by the pilot. This feature enhances the flexibility and functionality of the system, allowing for both direct remote control and automated maneuvers based on predefined commands.

Most flapping-wing aerial robots that have achieved attitude control typically employed conventional PD or PID controllers [20–21, 26–28, 32–34]. However, a limitation of these controllers is their weakness to adapt to changes in the robot's body configuration, emphasizing the necessity for enhanced attitude control solutions.

To address these issues, several adaptive controllers have been developed for the flapping-wing aerial robots. A multiaxial adaptive controller (Figure 1.5 (b)) with the TD (tracking differential) as the reference generator was developed by Mou *et al*. [44], which allows the robot to track the reference well even with unknown bias torque and inaccurate model parameters. Although this controller offers advantages in terms of overshoot suppression, decoupling performance, and control accuracy, it was dedicated to their dual-motor, four-wing robot and is not applicable to single-motor, pair-wing robots mimicking hummingbirds. Chirarattananon *et al*. [45] proposed an adaptive controller (Figure 1.5 (c)) using Lyapunov function

candidates and sliding-mode control techniques for a millimeter-scale flapping-wing robot, which could compensate the minor manufacturing imperfections or damages. Its ability to adapt to notable deviations from the designed model, however, was not demonstrated. Chand *et al*. [46] proposed an adaptive pole-placement control scheme. They focused on real-time estimation of low-level robot parameters rather than relying on a high-fidelity aerodynamic model which is difficult to be obtained in case of flapping-wing robots. Stable flight was realized by autonomously controlling the body pitch, but yaw and roll control was not achieved. Furthermore, while their control scheme could adapt to gradual changes of the model parameters over time, the more notable changes such as wing damage was not considered. An adaptive control scheme (Figure 1.5 (d)) using DOBC (disturbance-observer-based control) was proposed by Lee *et al*. [47] for a flapping-wing robot with a tail wing. This controller compensated external disturbances, enhancing both tracking performance and robustness. As a result, the robot could maintain the attitude under simulated and actual wind disturbances. However, they focused on the specific flapping-wing robot with a tail wing and the proposed controller is not directly applicable to flapping-wing robots without a tail wing. Tu *et al*. [48] investigated the effects of loss of the wing area near the wingtip on the wing kinematics, lift and torque generation, and aerodynamic damping. Then, an adaptive controller is proposed to cope with the wing damage induced detrimental effects on flight capacity. However, this controller was tailored for dual-motor flapping-wing robots in which each wing is directly driven by an independent motor, remaining a challenge for flapping-wing robots in which a pair of wings are mechanically connected and driven by a single motor.

1.3 Objective and structure

Despite stable hovering has been achieved in several flapping-wing aerial robots, challenges persist in maintaining attitude control, especially when encountering changes in their body configuration, such as wing fatigue or loss of wing area due to harsh operations. Additionally, flapping-wing aerial robots often struggle with enhancing lift capacity due to their size and weight constraints, yet a higher lift capability is essential for accommodating diverse payloads in practical applications. Addressing these challenges, this study concentrates on the development of a hummingbird-mimetic flapping-wing aerial robot, with specific

objectives aimed at refining its operational dynamics. The primary goals include:

Increasing lift capacity: A key focus is on increasing the robot's lift generation capability, enabling it to accommodate a wider range of payloads.

Enhancing robustness to physical alterations: This study aims to improve the robot's ability to adapt and maintain control when encountering changes in body configuration, such as wing area loss due to "molting" or damage operating in demanding environments, ensuring stable and reliable performance even in challenging conditions, thereby broadening the scope of its deployment capabilities.

By addressing these specific aspects, this study aims to advance the capabilities of biomimetic flapping-wing aerial robots, making contributions in replicating the agile and resilient nature of biological hummingbirds in a robotic counterpart.

The remainder of this thesis is structured as follows:

Chapter 2 details the development of a rack-pinion-based flapping mechanism with a dual-layer planetary gear reducer, exploring the effects of gear ratio and flapping amplitude on lift generation and power efficacy. Another significant portion of this chapter is dedicated to the development of a biomimetic wing integrated with a connecting membrane, including the inspiration, design, fabrication method, and performance evaluation. It delves into the proposal of the connecting membrane that enhanced lift generation of the wing through soft limitation of passive feathering, and concludes with the presentation of an artificial molting wing.

Chapter 3 presents the development of a control mechanism based on wing modulation, including the prototype design, fabrication, and static measurement. The control principles, including the methods employed to generate control torque for roll, pitch, and yaw movements are introduced in detail.

Chapter 4 introduces the architecture and operational principles of the attitude controller, which employs a three-loop feedback structure and a disturbance observer. This chapter expounds upon the methodology used to assess the controller's performance, specifically through semi-tethered experiments employing a gimbal mechanism. Additionally, it presents a comparative analysis of the controller's effectiveness in managing roll, pitch, and yaw motions, compared with conventional PD and PID controllers.

Chapter 5 delivers the concluding remarks of this study, providing a comprehensive summary of key findings and contributions. It also contemplates

potential future research directions, highlighting potential areas for further exploration and development based on the insights and results garnered from the this research.

Chapter 2
Flapping mechanism and biomimetic wings

2.1 Flapping mechanism

2.1.1 Rack-pinion-based flapping mechanism

A rack-pinion-based flapping mechanism with one degree of freedom was created, as shown in Figure 2.1. The rotational output of the DC coreless motor (L0820N5M55, Toung Mei Cang Xing (Shenzhen) Technology Corporation, China) was reduced by a dual-layer planetary gear reducer, it drives a linear slider through a Scotch-Yoke mechanism under the constrains of two vertical rods on the top cover,

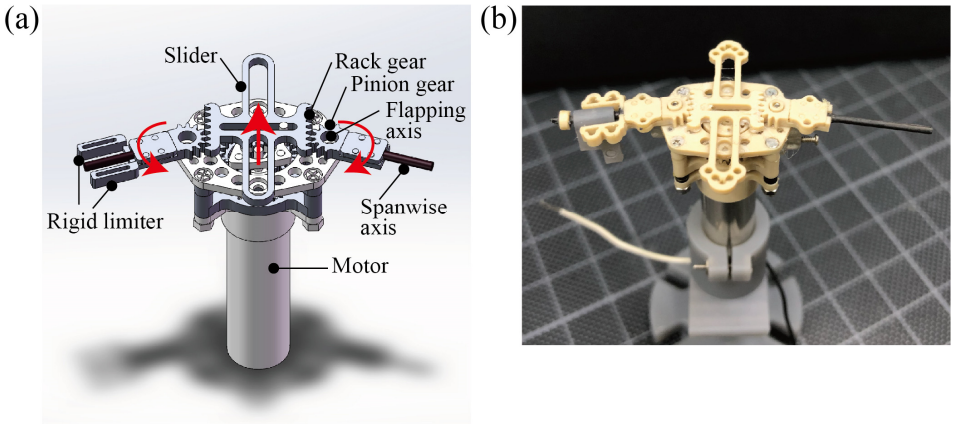

Figure 2.1 Design of the rack-pinion-based flapping mechanism.

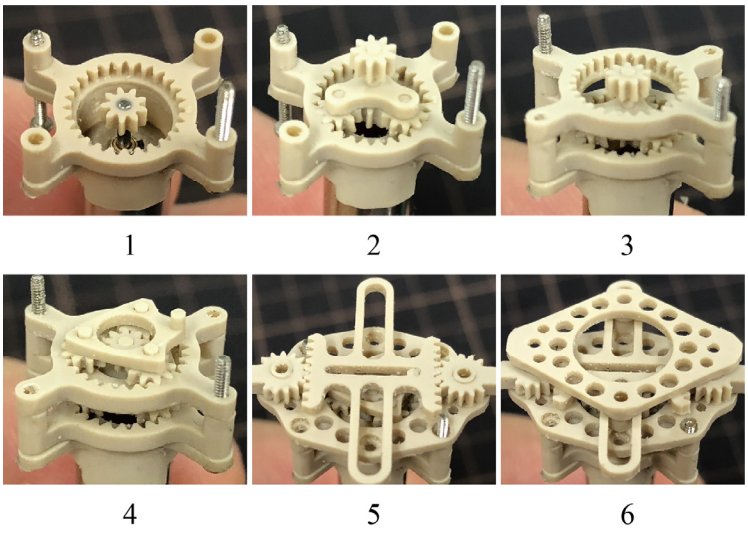

Figure 2.2 Assemble flow of the dual-layer planetary gear reducer and the rack-pinion-based flapping mechanism.

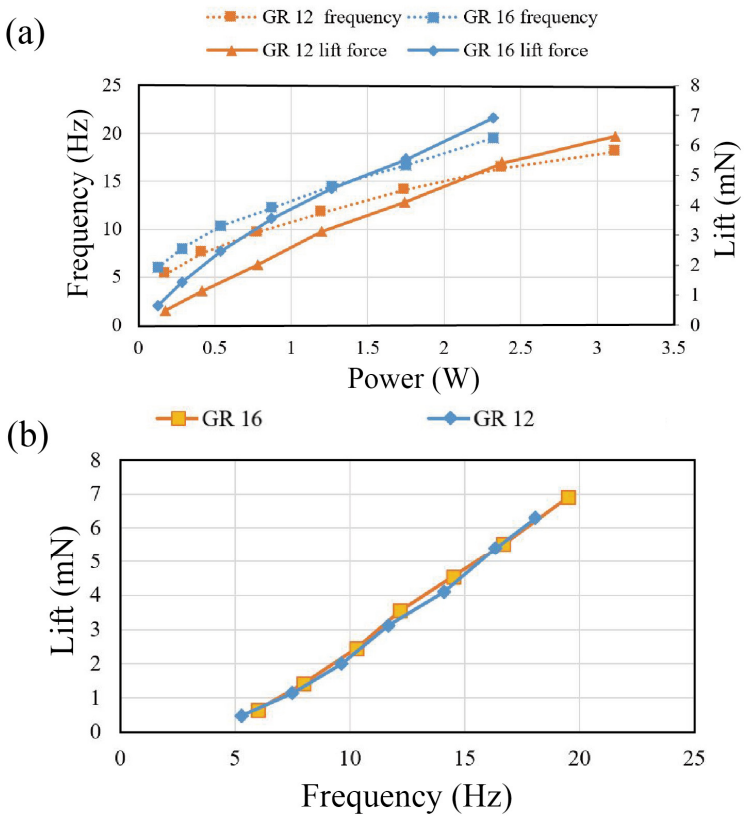

Figure 2.3 Performance evaluation of the gear ratios of 12 and 16. (a) The relationship between consumed electric power, frequency, and lift, (b) the relationship between frequency and lift.

transferring the consistent rotation motion of the motor into reciprocal linear motion of the slider. Rack gears on each side of the slider then rotated each pinion gear to which the spanwise axis was fixed, transferring the reciprocal linear motion of the slider into reciprocal flapping motion of the spanwise axis. The wing connected to the spanwise axis through a connector that can rotate around the spanwise axis. The dual-layer planetary gear reducer, slider with rack gears, and pinion gears were fabricated by CNC (computer numerical control) milling a 5-mm-thick PEEK (polyether ether ketone) plate, they were assembled from bottom to top and fixed using bolts and nuts as shown in Figure 2.2. The total weight of the electric flapping mechanism, including a 5 g DC motor, was 6.75 g, which was similar to the weight of our model hummingbird [49].

The rack-pinion-based flapping mechanism is compact, lightweight, and

durable, its flapping amplitude can be easily adjusted by modifying the stroke length of the rack gear and the size of the pinion gear, allowing it to achieve a large flapping amplitude with small size.

2.1.2 Effect of gear ratio

The dual-layer planetary gear reducer used in the flapping mechanism allows high torque transmission in a compact and lightweight form, beneficial for small and powerful robots. Dual-layer design makes it easy to implement various gear ratios, gear ratios of 12 and 16 were specifically tested to evaluate their performance in this study. Figure 2.3 illustrates the relationship between consumed electric power, frequency, and lift for these two gear ratios using a single wing. The results indicate that a gear ratio of 16 yielded a higher frequency and greater lift at the same electric power consumption compared to a gear ratio of 12, signifying enhanced power efficiency. Given that the flapping amplitude remained constant, identical lift levels were produced at equivalent frequencies for both gear ratios, as depicted in Figure 2.3 (b). Consequently, the gear ratio of 16 was selected for the final prototype.

2.1.3 Effect of flapping amplitude

Flapping amplitude A of the rack-pinion-based flapping mechanism is

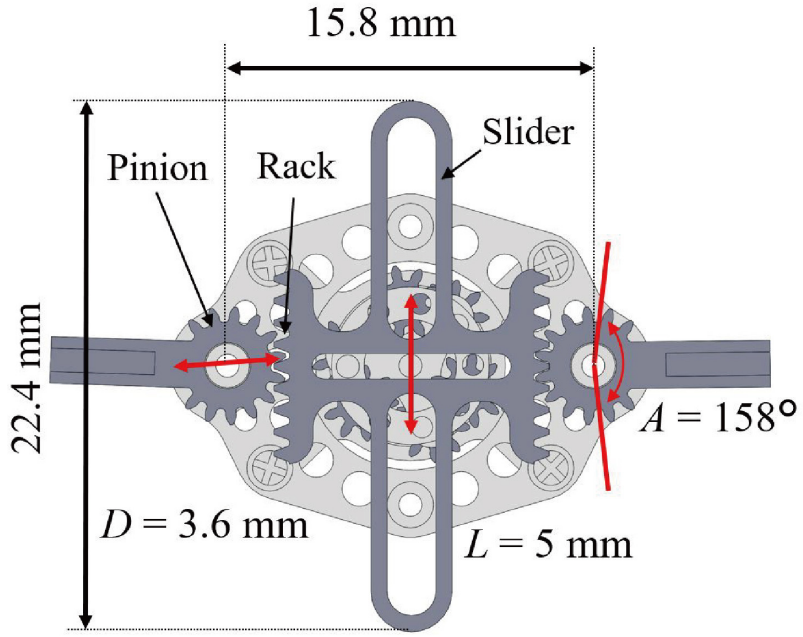

Figure 2.4 Top view of the flapping mechanism, indicating the calculation of flapping amplitude.

calculated as

$$A = \frac{L}{\pi D} 360^{\circ} \quad (1).$$

L represents the stroke length of both the slider and the rack gear, while D denotes the diameter of the pinion gear, as illustrated in Figure 2.4. Two flapping amplitudes were tested in this study, 158° and 178°. Figure 2.5 displays the relationship between consumed electric power, frequency, and lift for these two amplitudes using a single wing setup. The data revealed that the 158° amplitude achieved a higher frequency at the same power input but generated less lift at equivalent frequencies compared to 178° amplitude. Consequently, the 158° amplitude was found to produce a similar level of lift but with lower electric power consumption, leading to its selection for the final prototype due to its greater power

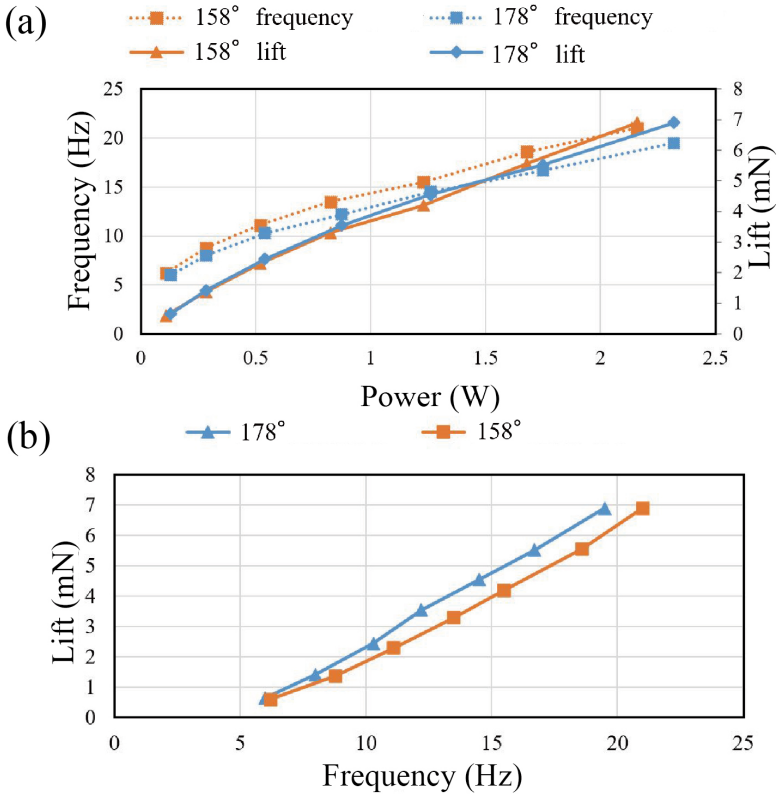

Figure 2.5 Performance evaluation of the flapping amplitudes of 158° and 178°. (a) The relationship between consumed electric power, frequency, and lift, (b) the relationship between frequency and lift.

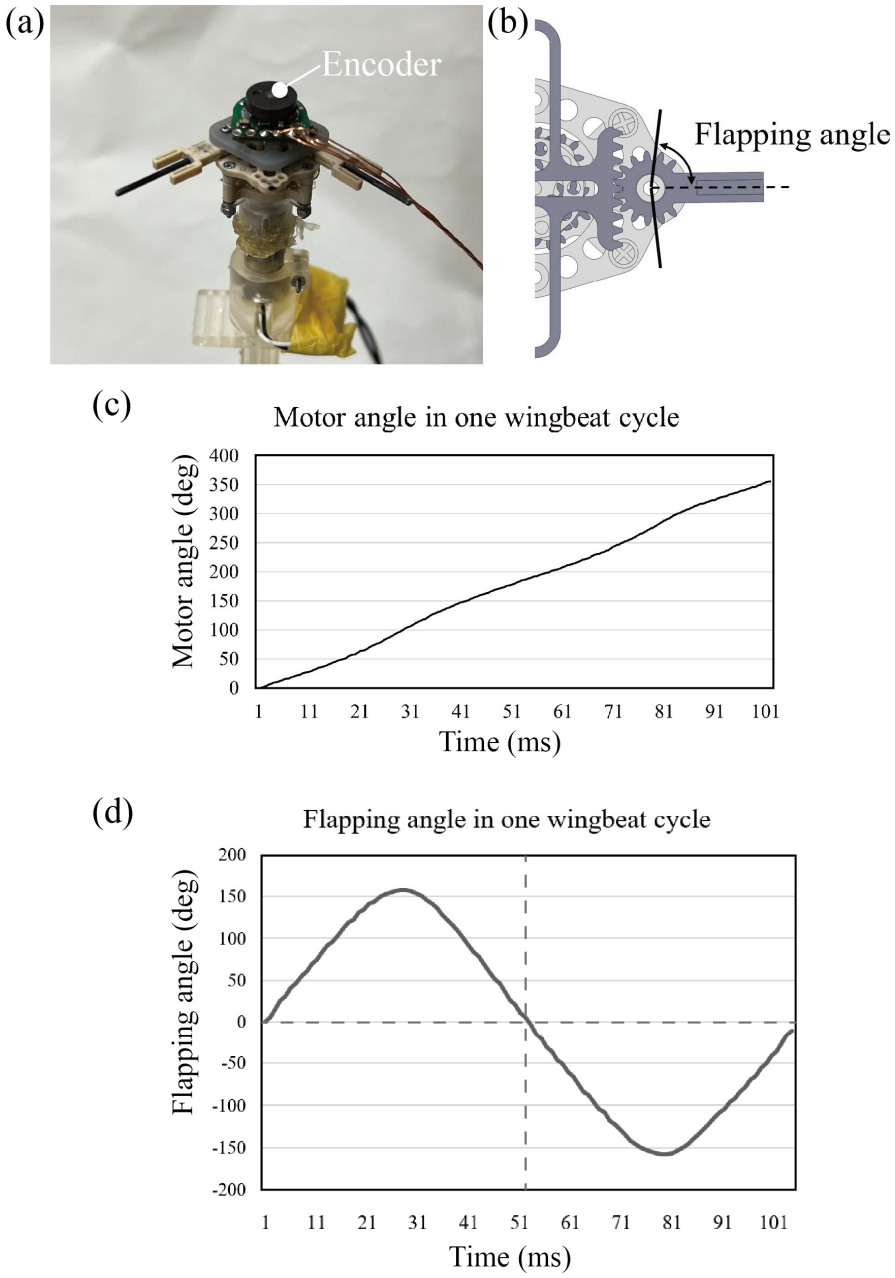

Figure 2.6 Evaluation of the kinematics of the rack-pinion-based flapping mechanism. (a) Set up of the encoder, (b) definition of the flapping angle, (c) motor angle in one wingbeat cycle at 10 Hz, (d) flapping angle in one wingbeat cycle at 10 Hz.

efficiency.

2.1.4 Flapping motion

To evaluate the kinematic behavior of the rack-pinion-based flapping mechanism, an encoder was integrated as shown in Figure 2.6 (a), and the flapping frequency was set to 10 Hz with a single wing attached. This setup facilitated accurate tracking of both the motor angle and the flapping angle (defined in Figure 2.6 (b)) during a single wingbeat cycle. The recorded motor angle presented a waveform pattern over the cycle as depicted in Figure 2.6 (c), reflecting changes in angular velocity during different phases of the flapping motion. On the other hand, the flapping angle closely followed a sinusoidal pattern, as depicted in Figure 2.6 (d).

2.2 Biomimetic wings

2.2.1 Insights from the wings of natural flyers

The flexural stiffness of hummingbirds and insects wings plays an important role in aerodynamic performance and influences the lift generation and maneuverability in their flight. Hummingbirds are thought to use similar aerodynamic mechanisms to those used by insects even though their profound musculoskeletal are different [9]. The effects of wing flexibility on aerodynamic performance in hummingbirds and insects have been explained experimentally in [50–52] and numerically in [53–55]. The wings of a cranefly were mimicked in [50], the wing that has the same level of deformation as the actual cranefly wing generated the largest average lift. The artificial wings that have similar weight and shape to the hummingbirds wing were introduced in [51], the flexural stiffness of their leading-edge and wing chord was varied, and the results indicated that flexible wing generated higher lift at low frequency, while rigid wing generated higher lift at high frequency, indicating that there is an effective frequency range depending on the stiffness of wings. The effects of camber angle, aspect ratio, and taper ratio on flexible wings were studied in [52], it was found that the best wing for the flapping wing robot had a right-angled trapezoidal shape and an aspect ratio of 9.3, which are very close to the parameters of natural hummingbirds. The effects of wing deformation on aerodynamic forces in hovering hoverflies were introduced in [53], and the results showed that the flexible wing produced 10% more lift and consumed 5% less energy than a rigid wing. The wings of a hawk-moth were modeled and simulated in [54], and the effects of twist, camber, and spanwise bending on the

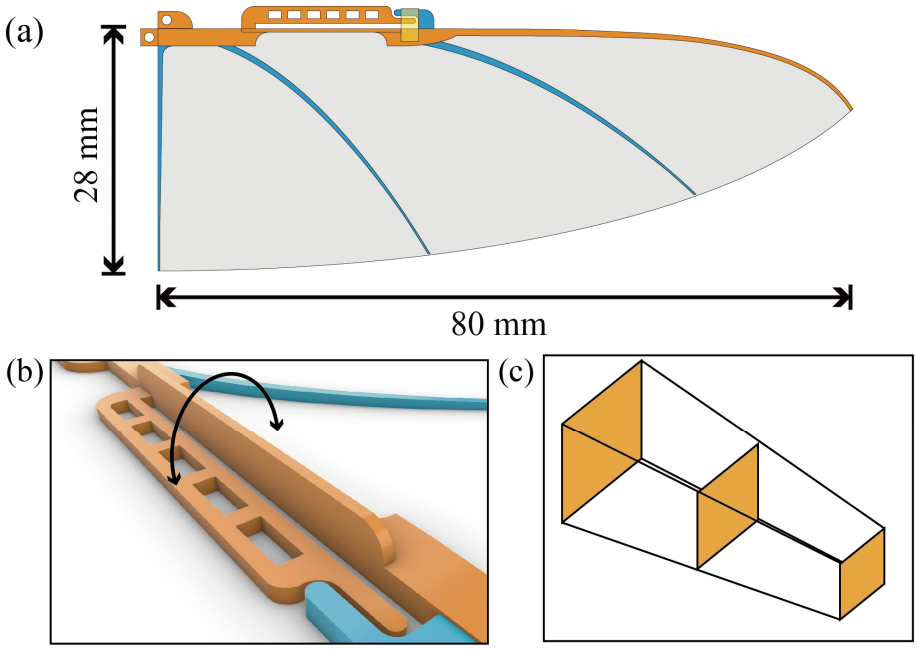

Figure 2.7 Design of the 3D printed biomimetic wing [57]. (a) Planar design and size outline of the wing, (b) schematic of the torsional arm, (c) tapered wing shaft design.

aerodynamic performance of flapping wings were analysed. The results indicated that wing twist enhanced efficiency by adjusting the AoA, camber increased lift by changing the direction of aerodynamic forces, and spanwise bending influenced the motion of wings such as flapping amplitude and phase near the wingtip and thus affected aerodynamic forces. The flexural stiffness of a bumblebee's wing was artificially strengthened in [56], and the vertical aerodynamic force after strengthening was reduced by 8.6%, indicating that the passive deformation of the wing resulted from flexible wing design may enhance lift production of bumblebees.

2.2.2 3D printed biomimetic wing

Figure 2.7 (a) illustrates the planar design of the biomimetic wing [57], featuring a 3D printed frame that consists of four wing shafts, supporting a stretchable membrane. The leading-edge shaft (indicated in yellow), serving as the main shaft, incorporates a torsional arm inspired by the wrist joint of a hummingbird's wing, as depicted in Figure 2.7 (b). This main shaft is fabricated using PET CF (carbon fiber reinforced polyethylene terephthalate) (3F PET CF 9780 BK, Lehmann & Voss & Co. KG., Germany), a material chosen for its

relatively large Young's modulus. The fabrication is done using a 3D printer, the Ultimaker S5 (Ultimaker B.V., The Netherlands). The remaining shafts (indicated in blue) are constructed using the material of PLA (polylactide) (Black Tough PLA, Ultimaker B.V., The Netherlands), chosen for its smaller Young's modulus. The wing's membrane is laser cut from an 8-um-thick urethane elastomer film (Silklon NES85, Okura Industrial Co., Ltd., Japan), chosen for its stretchability and durability. The 3D printed wing frame is meticulously adhered to the membrane using an elastic glue (Super X Hyper Wide, Cemedine Co., Ltd., Japan).

The planar design of the wing in this study mirrors the outline of a real Amazilia hummingbird's (Amazilia amazilia) wing [49]. However, the wing surface area was proportionally scaled up to 126% of the original size, that is, the wing lengths and surface area of the actual hummingbird and the biomimetic wing in this study were 70 mm and 80 mm, 1406 mm^2 and 1767 mm^2, respectively. The biomimetic wing's shafts were designed with increasing thickness and flexural stiffness from tip to root, as depicted in Figure 2.7 (c), following the static bending test results from actual feather shafts of an Amazilia hummingbird's specimen [58]. The wing frame was glued only on one side of the wing membrane, while the other side of the membrane was clean. Hence, the wing was asymmetric in the ventral-dorsal direction. The wing frame was also asymmetric because it was flat on the membrane side and printed towards the other side. A downstroke was defined as a stroke from the membrane side to the wing frame side, while an upstroke referred to the reverse motion.

2.3 Soft limitation of passive feathering

2.3.1 Passive feathering of flapping wings

Hummingbirds are able to sustain hovering by generating lift during both the downstroke and upstroke. This is possible due to their flexible wing structure, which allows the wings to feather (i.e., to rotate around the spanwise axis) and maintain appropriate AoA in each stroke [1–3]. The utilization of passive feathering has become prevalent in the design of flapping-wing robots of hummingbird size, because the wing structure can be simple and lightweight with no need for active spanwise rotation [20–26]. Typically, passive feathering is achieved through torsion of the wing surface. In some robots, the leading-edge spar rotates around the spanwise axis at the wing base to facilitate large amplitude feathering, while excess

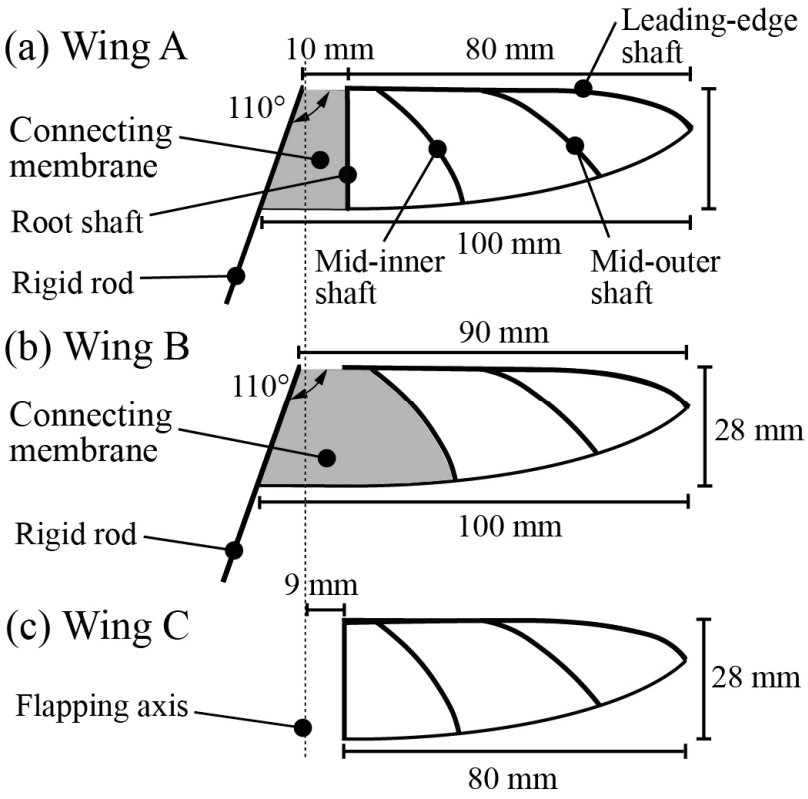

Figure 2.8 Planar outline designs of Wing A, B, C when the wings are placed on a flat surface without any loosening nor stretching [76]. (a) Wing A features a connecting membrane integrated into the wing that has four shafts, (b) Wing B features a connecting membrane integrated into the wing that has the root shaft removed, (c) Wing C features no connecting membrane integrated.

rotation is prevented by stoppers [59, 60]. However, the hard collision between the rigid stopper and the wing may cause unfavorable vibration and discontinuous behavior of the wing, leading to unsmooth and inefficient flapping. Some flapping-wing robots employed elastically flexural hinge to realize passive and elastic feathering [14, 61–63]. Possible drawback of the flexural hinge is that the hinge has to withstand not only the intended flexion, but also unintentional torsion.

Flight control can be possible by active control of the amplitude of the passive feathering. Previous flapping-wing robots capable of hovering changes the degree of loosening of the wing made of non-stretchable polymer films to vary the aerodynamic force of the wing [20–26, 29, 64–66]. The more the wing get loosened, the more feathering deformation occurs during flapping, varying the AoA and

aerodynamic force, resulting in smaller drag. Nonetheless, employing non-stretchable wing films presents a similar problem as the rigid stopper, resulting in abrupt cessation of feathering due to the complete expansion of the wing film, which consequently induces vibration.

2.3.2 Wing design and fabrication

This section introduces the concept of integrating an elastic connecting membrane into the 3D-printed biomimetic wing, as described in the previous section. This integration aims to achieve a soft and direct limitation of the wing's passive feathering to improve lift generation and power efficiency. The connecting membrane is designed as an extension at the base of the stretchable wing membrane, connecting to a rigid rod that is fixed at the body side of the flapping mechanism. This direct connection between the wing membrane and the body side via the soft elastomeric membrane avoids abrupt cessation of feathering and prevents unfavorable vibration and discontinuous behavior of the wing. The allowable amplitude of the feathering is adjusted by the initial loosening of the connecting membrane.

The planar outline designs of the three wings tested in this section, named as Wing A, B, and C, are shown in Figure 2.8. The wings consist of elastomeric membrane supported by 3D printed flexible shafts (leading-edge shaft, mid-outer shaft, mid-inner shaft, and chordwise root shaft) and CFRP (carbon fiber reinforced plastic) rigid rod, except for Wing C which does not have a rigid rod (Figure 2.8 (c)). The rigid rod was glued to the membrane and not directly connected to the leading-edge shaft. The angle between the rigid rod and the leading-edge shaft was 110° at initial state when the wing was placed on a flat surface without any loosening nor stretching (Figure 2.8 (a, b)). In installation of the wing to the flapping mechanism, the rigid rod was fixed to the body side, so that the angle between the rigid rod and the leading-edge shaft at the wing root was 90° (Figure 2.9). This arrangement results in the loosening of the connecting membrane. The connecting membrane directly binds the body-side edge of the wing surface and the body. Free feathering rotation of a wing connector around the spanwise axis is allowed by the initial loosening of the connecting membrane (Figure 2.9 (a)). The viscoelasticity of the connecting membrane absorbs the stopping shock at full stretch of the connecting membrane (Figure 2.9 (b)).

The fabricated Wing A, Wing B, and Wing C are shown in Figure 2.10. In Wing

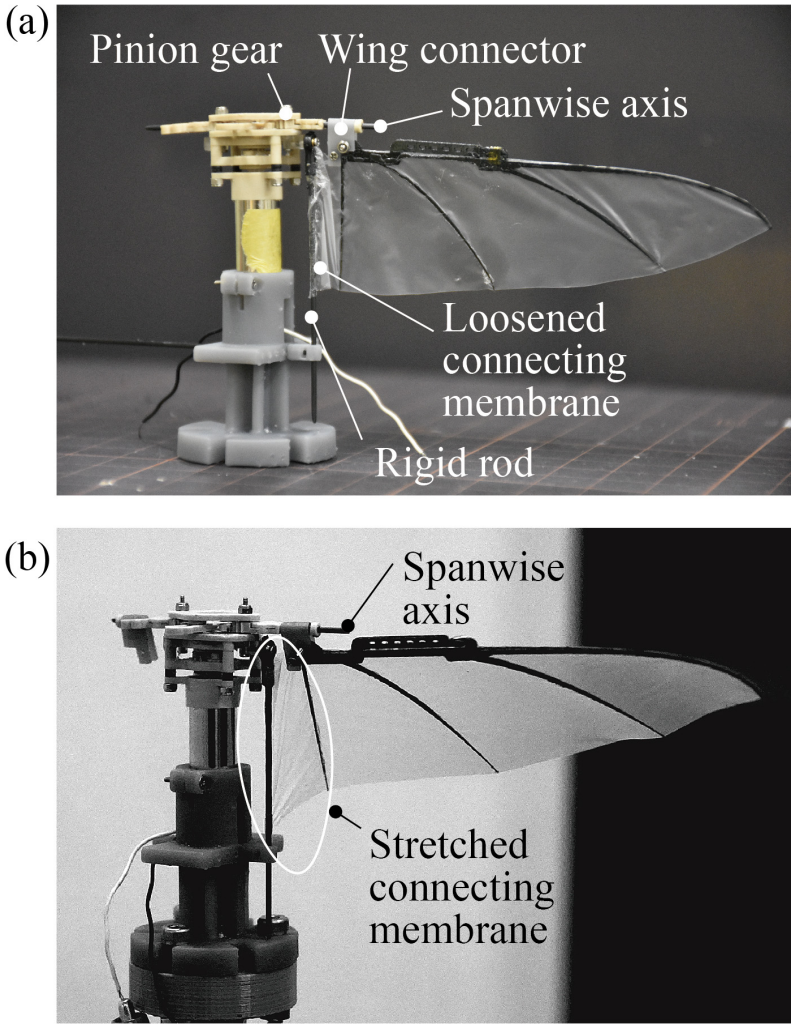

Figure 2.9 Wing A connected to the flapping mechanism via a wing connector. (a) Static state makes the connecting membrane loose in the neutral position, (b) the connecting membrane fully stretches and stops the feathering rotation around the spanwise axis during flapping.

Table 2.1 Mass and area of the fabricated wings

Wing	A	B	C
Mass (mg)*	206	203	205
Surface area (mm^2)	2103	2103	1767

*Mass of the rigid rod is not included.

A, the limits of free feathering angle were −23° and 23°, which was confirmed by

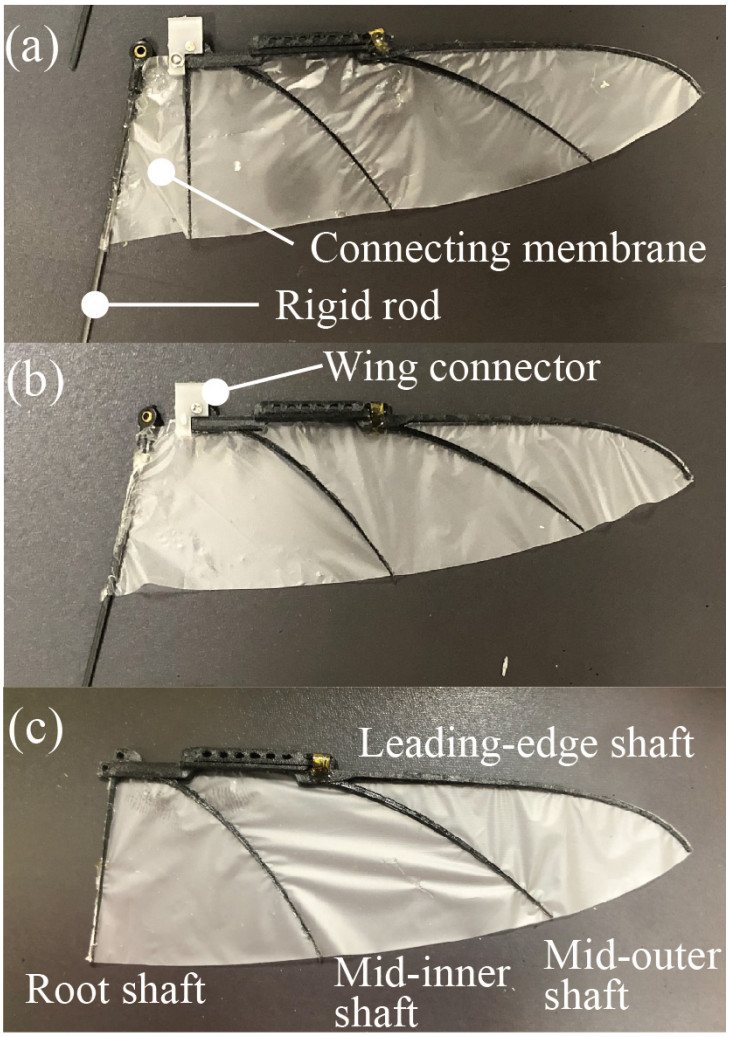

Figure 2.10 Fabricate wings: Wing A (a), Wing B (b), and Wing C (c). Wing A and Wing B have a connecting membrane integrated, and the root shaft of Wing B has been removed.

manually rotating the wing around the spanwise axis so that the connecting membrane fully expanded but did not stretch (Figure 2.11 (a)). Wing B had larger limits of −30° and 30° due to the larger connecting membrane (Figure 2.11 (b)). In the following experiments, the connecting membrane was compared with a rigid limiter attached to the spanwise axis (Figure 2.12 (a)). The wing can rotate around the spanwise axis until the wing connector hits the left or right inner bottom edge of the rigid limiter (Figure 2.12 (b, c)), allowing for a maximum rotation angle of

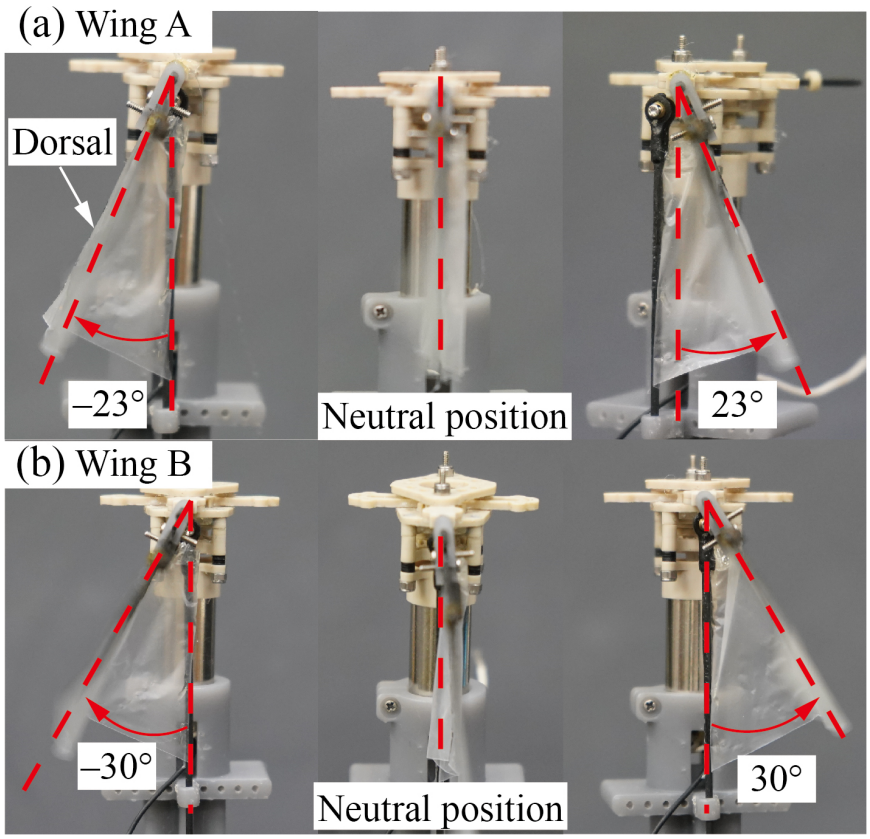

Figure 2.11 Side views of Wing A (a) and Wing B (b) demonstrating their limits of feathering.

±23° (Figure 2.12 (d)). This limit value of ±23° was determined through preliminary experiments with smaller and larger limits to maximize the lift.

Table 2.1 shows measured weight of the three wings and the designed surface area including the connecting membrane, where the weight of the rigid rod is not included. The surface area of Wing A and B were the same: 2103 mm^2. The surface area of Wing C was 1767 mm^2 which is 88% of Wing A and B. The weight varies between 203 mg and 206 mg. In comparison to Wing A, the absence of the root shaft in Wing B led to a reduction in weight by 3 mg. Wing C, lacking the connecting membrane, experiences a weight reduction of 1 mg.

2.3.3 Performance evaluation

A single wing was attached to the flapping mechanism through a wing connector, and the flapping frequency was manually adjusted to 12, 15, 18, 21, and 24 Hz by changing the input voltage. The flapping mechanism was placed on an

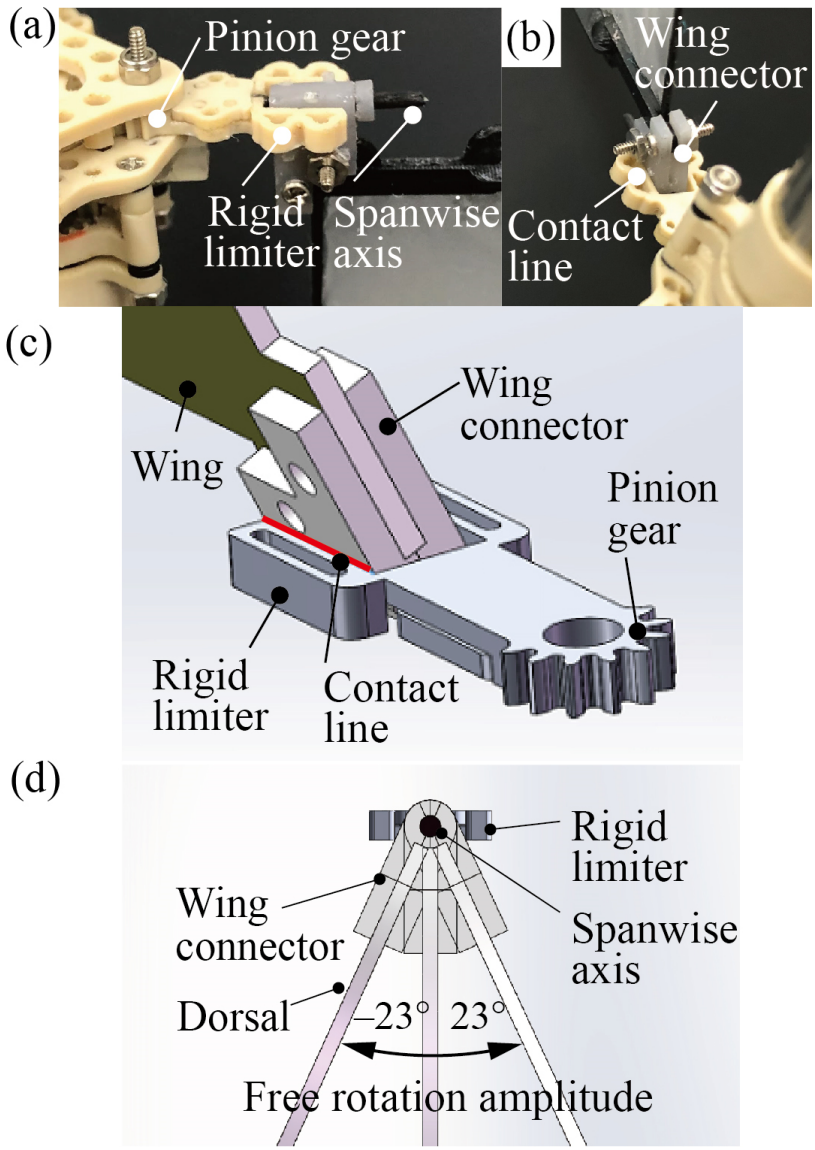

Figure 2.12 Schematics of the rigid limiter. (a) A top-down view of the spanwise axis featuring an integrated rigid limiter. (b) A bottom-up view of the spanwise axis highlighting the contact line between the wing connector and the rigid limiter. (c) A close-up schematic highlighting the contact line (red color) between the wing connector and the rigid limiter. (d) Cross-section schematic of the rigid limiter showing the free rotation amplitude of the rigid limiter.

electric balance (UW1020H, Shimadzu Corporation, Japan) via a 240-mm-long vertical steel rod. The input current and voltage were measured by reading the

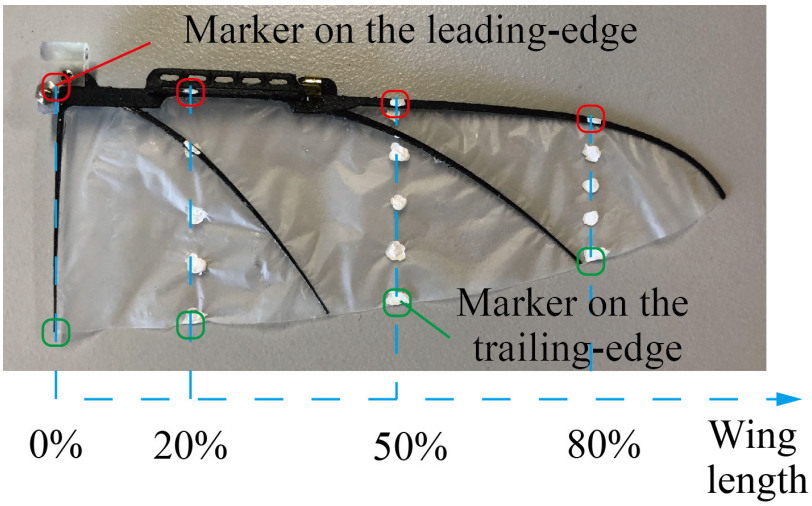

Figure 2.13 The wing was marked for 3D motion analysis, including markers on the leading edge (red circle) and trailing edge (green circle) to determine the wing chord and calculate the feathering angle. Additional markers were placed along the wing chords, from the leading-edge shaft to the trailing edge, at positions of 20%, 50%, and 80% of the wing length.

display of the power supply. Average lift, F (mN), was measured by reading the display of the electric balance. These values on the display were almost constant during flapping. Input power, P (W), was calculated by multiplying the current and voltage values. Since it is difficult to measure the output aerodynamic power by flapping, we assessed the efficacy of lift generation as a lift per input power. The efficacy, η (mN/W), was defined as

$$\eta = F/P \quad (2).$$

This metric of efficacy was also used in previous studies using electric flapping mechanisms [52, 67, 68].

The wing motion and deformation were observed and measured using three synchronized high-speed video cameras (Fastcam-MiniAX100, Photron Limited, Japan), with a frame rate and image resolution of 2000 frames/s and 1024×1024 pixels, respectively. The exposure time for each frame was set to 1/10000 s to avoid motion blur. Five markers were painted with white ink on each wing chords at the positions of 20%, 50%, and 80% of the wing length (Figure 2.13). The 3D positions of each marker were obtained using 3D motion analysis software (DIPP-Motion V,

DITECT Corporation Limited, Japan). The feathering angle was defined as the angle between each wing chord and the vertical vector. The spanwise twist angle was calculated by subtracting the feathering angle at 0%-wing-length from the feathering angle at 80%-wing-length. T (s) was defined as the total duration of a complete flapping cycle, while t (s) denotes a specific moment within this cycle. To pinpoint the start and end of a flapping cycle ($t = 0$ and $t = T$), we referred to high-speed video frames where the velocity at the tip of the spanwise axis reached zero. To evaluate the wing deformation during each stroke, we defined the downstroke and upstroke as the durations of 0.1–0.4 t/T and 0.6–0.9 t/T, respectively, by excluding the durations of each stroke reversal from the flapping cycle.

2.3.4 Results and discussion

Figure 2.14 presents the average lift and efficacy of each experiment at all flapping frequencies, while Table 2.2 provides a summary of the average lift and efficacy of each experiment at the flapping frequency of 24 Hz. Wing A generated an average lift of 116 mN with an efficacy of 41mN/W at 24 Hz. With the additional rigid limiter, the average lift and efficacy decreased to 106 mN and 33 mN/W, respectively. Wing B generated an average lift of 104 mN with an efficacy of 37 mN/W at 24 Hz. With the additional rigid limiter, the average lift slightly increased to 108 mN, while the efficacy decreased to 33 mN/W. Wing C, which had no connecting membrane integrated, generated an average lift of 107 mN with an efficacy of 33 mN/W with the rigid limiter at 24 Hz. Without the rigid limiter, Wing C randomly rotated around the spanwise axis and did not generate sufficient lift at any of the flapping frequencies.

The feathering angles of Wing A, Wing A with an additional rigid limiter, Wing B, Wing B with an additional rigid limiter, and Wing C with a rigid limiter are shown in Figure 2.15. The average feathering and twist angles for each stroke are summarized in Table 2.3. In all the experiments, the feathering angle increased from the 0%-wing-length chord to 80%-wing-length chord, indicating that all the wings twisted during flapping. However, the twist magnitudes differ among the wings. For Wing A, the average feathering angles at the 80%-wing-length chord were 72° and −73° during the downstroke and upstroke, respectively, while the twist angles were 52° and −54° (Figure 2.15 (a)). For wing B, the average feathering angles at the 80%-wing-length chord were 82° and −81° during the downstroke and upstroke, respectively, while the twist angles were 60° and −64° (Figure 2.15 (c)). In contrast,

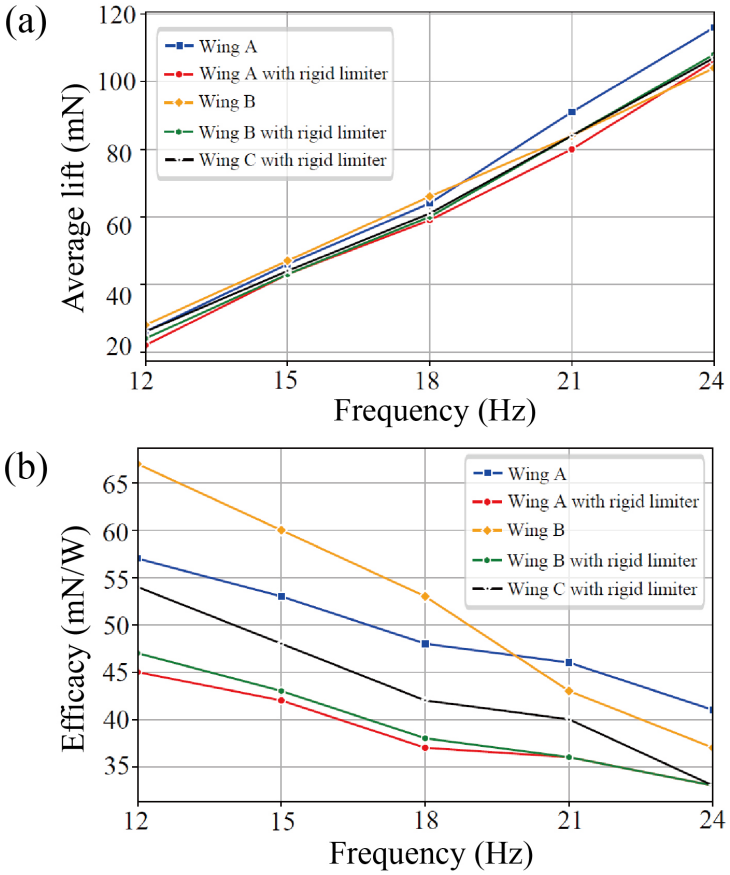

Figure 2.14 Average lift (a) and efficacy (b) of Wing A (blue line), Wing A with rigid limiter (red line), Wing B (yellow line), Wing B with rigid limiter (green line), and Wing C with rigid limiter (black line) from 12 to 24-Hz flapping.

Table 2.2 Average lift, current, voltage, input power, and efficacy at 24-Hz flapping frequency

Wing	A		B		C
Rigid limiter	-	With a rigid limiter	-	With a rigid limiter	With a rigid limiter
F (mN)	116	106	104	108	107
Current (A)	0.8	0.94	0.8	0.94	0.91
Voltage (V)	3.5	3.4	3.5	3.5	3.5
P (W)	2.8	3.2	2.8	3.3	3.2
η (mN/W)	41	33	37	33	33

Wing C has a rigid limiter, and the average feathering angles at the 80%-wing-

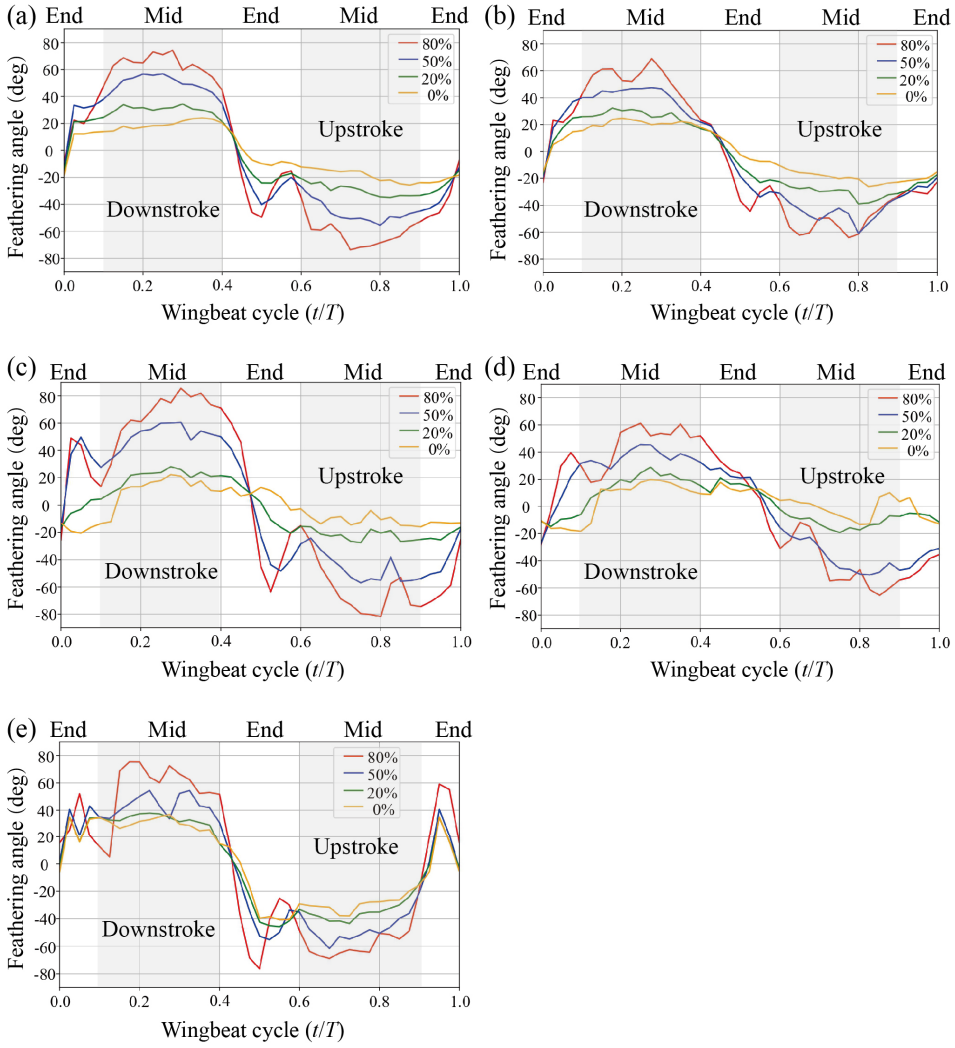

Figure 2.15 Feathering angles of Wing A (a), Wing A with rigid limiter (b), Wing B (c), Wing B with rigid limiter (d), and Wing C with rigid limiter (e) at 24-Hz flapping. Grey regions (0.1–0.4 *t/T* and 0.6–0.9 *t/T*) indicate downstroke and upstroke periods, respectively.

length chord were 72° and −73° during the downstroke and upstroke, respectively, while the twist angles were 27° and −32° (Figure 2.15 (e)). When the rigid limiter was added to Wing A, the average feathering angles at the 80%-wing-length chord became 65° and −63° during the downstroke and upstroke, respectively, while the twist angles became 38° and −38° (Figure 2.15 (b)). When the rigid limiter was added to Wing B, the average feathering angles at the 80%-wing-length chord

Table 2.3 Average feathering and twist angles around the mid-stroke.

Wing	A		B		C
Rigid limiter	-	With a rigid limiter	-	With a rigid limiter	With a rigid limiter
Avg. feathering angle at 80% (Downstroke, upstroke)	72°, −73°	65°, −63°	82°, −81°	60°, −63°	72°, −73°
Avg. feathering angle at 0% (Downstroke, upstroke)	20°, −19°	27°, −25°	22°, −17°	18°, −18°	45°, −41°
Avg. twist angle (Downstroke, upstroke)	52°, −54°	38°, −38°	60°, −64°	42°, −45°	27, −32°

become 60° and −63° during the downstroke and upstroke, respectively, while the twist angles become 42° and −45° (Figure 2.15 (d)). The difference in the average feathering angles and twist angles between the downstroke and upstroke in each flapping experiment may be attributed to the asymmetry of the dorsal and ventral side of the wing structure. This asymmetry results in different bending behaviors of the wing in the ventral and dorsal directions.

Wing A without the rigid limiter generated higher lift and efficacy than Wing C with the rigid limiter, at all the frequencies. Particularly, at 24 Hz, Wing A produced 24.2% higher efficacy and 8.4% more lift compared to Wing C (Table 2.2). The larger lift of Wing A than that of Wing C was not due to the increase of the surface area by the connecting membrane. In fact, lift and efficacy of Wing A with the rigid limiter (106 mN, 33 mN) was almost the same as those of Wing C with the rigid limiter (106 mN, 33 mN) as shown in Table 2.2. That is, the increase in the surface area did not lead to increase in lift and efficacy. Therefore, wing deformation can be attributed to the increase in lift and efficacy of Wing A without a rigid limiter.

As shown in Table 2.3, the average feathering angles at 80%-wing-length chord of Wing A (72°, −73°) were the same as those of Wing C (72°, −73°). On the

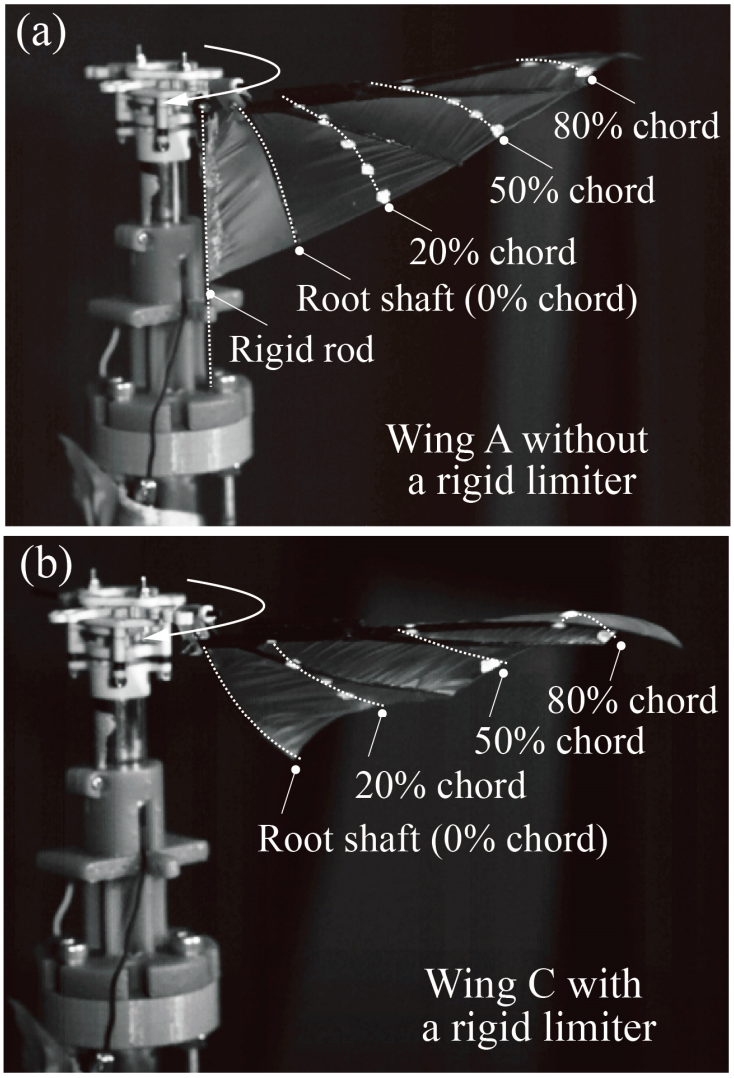

Figure 2.16 Wing deformation of Wing A without a rigid limiter (a) and Wing C with a rigid limiter (b) at $t/T = 0.2$.

contrary, average feathering angles at 0%-wing-length of Wing A (20°, −19°) were smaller than those of Wing C (45°, −41°), resulting in the larger twist angles of Wing A (52°, −54°) than those of Wing C (27°, −32°). This small feathering at 0%-wing-length of Wing A can be attributed to the fact that the connecting membrane restricted excess chordwise bending of the root shaft as observed in Figure 2.16 (a). Moreover, the connecting membrane also created positive camber at the root shaft, 20% chord, and 50% chords. On the contrary, removal of the connecting membrane led to large bending of the root shaft, accompanied by negative camber at the root

shaft, 20% chord, and 50% chords (Figure 2.16 (b)). It is assumed that this positive camber created by the connecting membrane enhanced the lift and efficacy in Wing A.

Fluctuation in feathering angles at the end of each stroke of Wing A was smaller than that of Wing C with the rigid limiter (Figure 2.15 (a, e)), indicating that the connecting membrane also reduced the vibration at the stroke reversal. In addition, the large twist by the connecting membrane possibly stored elastic energy, which might promote a quick stroke reversal by releasing the elastic energy.

Wing B which had no root shaft showed a larger free feathering amplitude (±30°) than Wing A (±23°). As a result, Wing B generated similar lift but with higher efficacy than Wing A when the flapping frequency was 18 Hz or lower. The efficacy at 18 Hz was 53 mN/W for Wing B and 48 mN/W for Wing A (Figure 2.14 (b)).

Conversely, when the flapping frequency was 21 Hz or higher, Wing A generated larger lift with higher efficacy. At a flapping frequency of 24 Hz, the lift and efficacy of Wing A were 10.8% and 11.5% higher than those of Wing B (Table 2.2), respectively. At 24 Hz, Wing B experienced more twisting at mid-stroke than Wing A (Figure 2.15 (a, b)). Without the root shaft, the connecting membrane of Wing B tends to vibrate and become unstable, resulting in lower lift generation and inefficiency.

When the rigid limiters are added to Wing A and Wing B, which already have the connecting membrane integrated, the rigid limiter firstly limits the feathering rotation around the spanwise axis before the connecting membrane stretches. Consequently, Wing A without the rigid limiter generated higher lift and higher efficacy at all frequencies than Wing A with the rigid limiter (Figure 2.14). Particularly, at 24 Hz flapping, a 24.2% higher efficacy and 9.4% higher lift were recorded (Table 2.2). This result indicates that the rigid limiter reduces the effectiveness of the connecting membrane on both lift and efficacy for Wing A. The same tendency was found for Wing B, except that the lift with the rigid limiter was 3.8% higher than that without the rigid limiter when the flapping frequency was 24 Hz (Figure 2.14 (a)). This could be because the rigid limiter suppressed excess feathering of Wing B at 24 Hz (Figure 2.15 (d)).

2.3.5 Conclusions

In conclusion, the connecting membrane that softly and directly limits passive

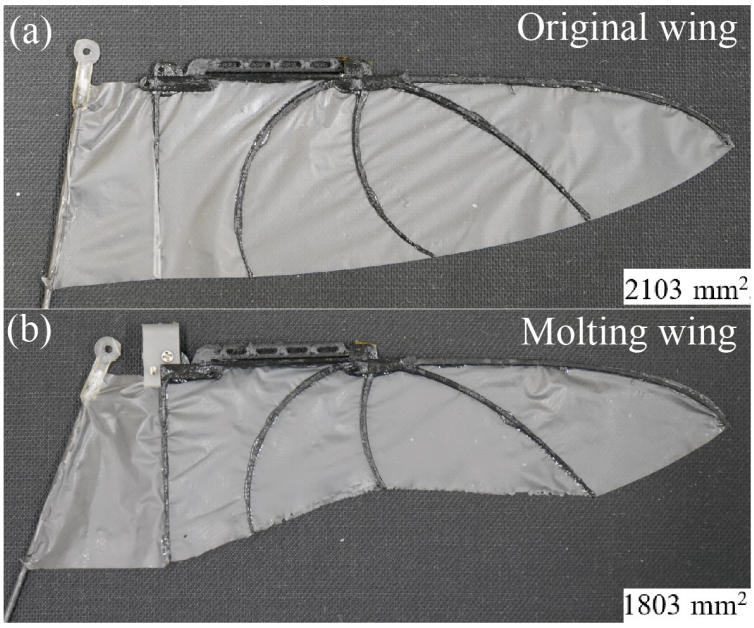

Figure 2.17 (a) The original wing designed based on the evolution of Wing A described in Chapter 2.3.2, (b) the molting wing designed based on the molting pattern of a hummingbird wing.

feathering at wing root of flapping wings was found to augment wing torsion by curbing feathering in the wing's root chord during the mid-stroke compared with a conventional rigid stopper that stops the feathering rotation around the spanwise axis rigidly. As a result, 24.2% higher efficacy and 8.4% higher lift than the conventional rigid stopper were achieved at 24 Hz. Additionally, the wing's chordwise root shaft was found to suppress vibration of the connecting membrane at the end of each stroke. The lift and efficacy can be improved by removal of the chordwise root shaft for flapping frequency of 18 Hz and lower by allowing larger free feathering amplitude. The payload of the robot depends on the operational frequency or input power, with a payload range of 5-7 grams at 30 Hz.

2.4 Artificial molting wing

Molting of flight feathers is a vital process for birds to maintain their wings throughout the lifetime. All flight feathers are annually replaced with new ones [69, 70]. Typically, molting starts from the inner feathers and progresses to the outer feathers over two months. Despite the partial loss of the wing surface due to molting,

birds including hummingbirds can adapt to this defect of the wing, maintaining their ability to fly during molting period [77].

Inspired by the molting of bird wings, we designed an artificial molting wing to test the robustness of our control method which is explained in the following section. The original wing, an evolution of Wing A as described in the previous section, has a design featuring a wing area of 2103 mm^2, as illustrated in Figure 2.17 (a). The artificial molting wing was created by cutting off a portion of the original wing at the trailing mimicking the hummingbird wing during molting [71], as depicted in Figure 2.17 (b). The wing area of the molting wing was 1803 mm^2 which was 14.1% smaller than that of the original wing, resulting a 11.3% reduction in lift generation at 20 Hz.

2.5 Summary

This chapter primarily focused on the development of a rack-pinion-based flapping mechanism, fabricated through CNC milling of a PEEK plate. A dual-layer planetary gear reducer was employed, with experiments conducted using two different gear ratios of 12 and 16. It was observed that the gear ratio of 16 enabled the flapping mechanism to achieve higher frequency and lift at the same electric power consumption compared to the gear ratio of 12. Additionally, the mechanism was tested with two flapping amplitudes, 158° and 178°. The findings revealed that while the 178° amplitude generated more lift at the same frequency, the 158° amplitude was more efficient in terms of lift generation per unit of electric power consumption. The kinematics of the flapping mechanism were monitored using an encoder set at a flapping frequency of 10 Hz. The motor angle displayed a waveform pattern during a single wingbeat cycle, reflecting variations in angular velocity at different phases, while the flapping angle predominantly adhered to a sinusoidal function.

Then, the insights from the wings of hummingbirds and insects were introduced, leading to the design of a biomimetic wing that mimics the flexural stiffness of the hummingbird's wing. The biomimetic wing is composed of a 3D printed shaft that supports an elastic membrane, which is precisely cut from an 8-um-thick urethane elastomer film using a laser cutting machine. A connecting membrane that directly and softly limit the passive feathering was integrated into the biomimetic wing and its effects on lift generation were investigated. It was found that the soft limitation

of passive feathering using the elastic connecting membrane increased lift generation and improved electric power efficacy compared to the hard limitation using a rigid limiter. This is achieved by curbing feathering in the wing's root chord while promoting feathering in the wing's tip chord, which augmented total wing torsion during the mid-stroke.

Drawing inspiration from the natural molting process of hummingbird wings, an artificial molting wing was developed to assess the robustness of our control method in response to changes in the robot's body configuration. The molting wing was created by strategically cutting a portion of the original wing which was designed based on the evolution of Wing A, leading to a reduction in wing area by 14.1% and a consequent 11.3% decrease in lift at 20 Hz.

Chapter 3
Control mechanism

3.1 Attitude control through wing modulation

3.1.1 Design and fabrication

Figure 3.1 (a) shows the components of the flapping-wing aerial robot developed in this study, with the forward direction, as well as roll, pitch, and yaw rotations of the robot's body, being defined as illustrated in Figure 3.1 (b). The robot has a total weight of 17.5 g and a wingspan of 185 mm, with a detailed weight breakdown presented in Figure 3.2. The attitude control mechanism of the robot is

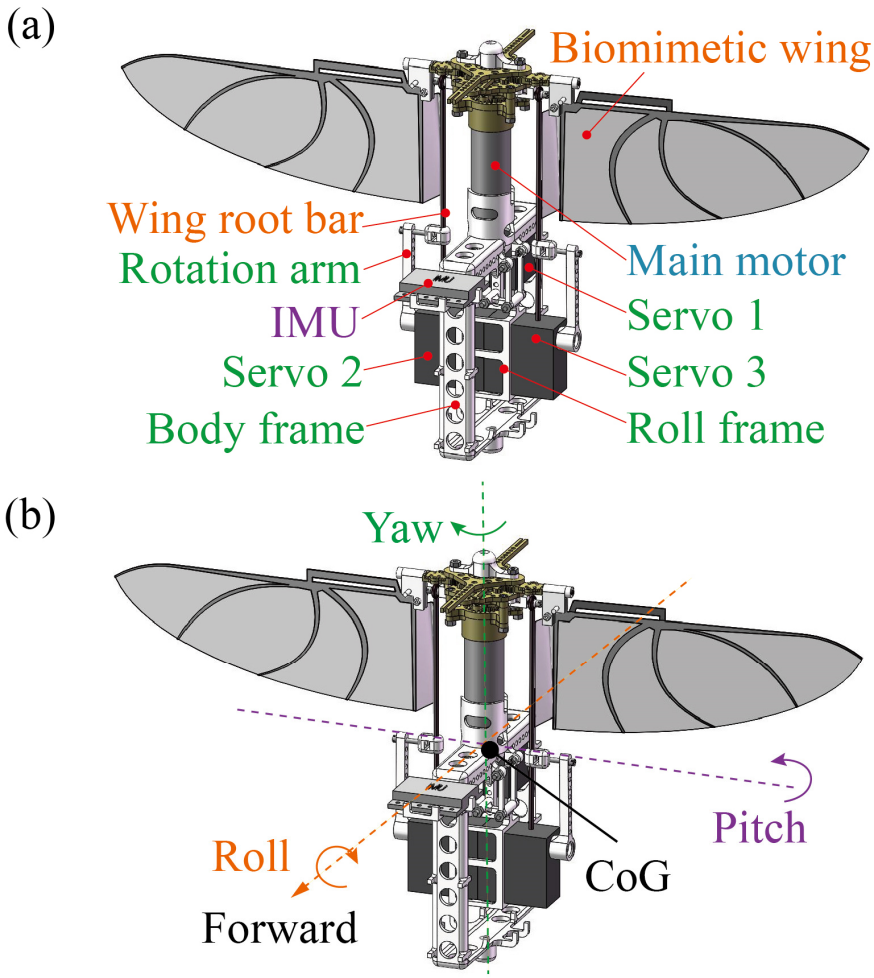

Figure 3.1 Schematic of the flapping robot. (a) The components of the robot, including the flapping mechanism, the biomimetic wings, the control mechanism, and an IMU sensor, (b) the definition of roll, pitch, and yaw rotations around the CoG of the robot and the forward direction.

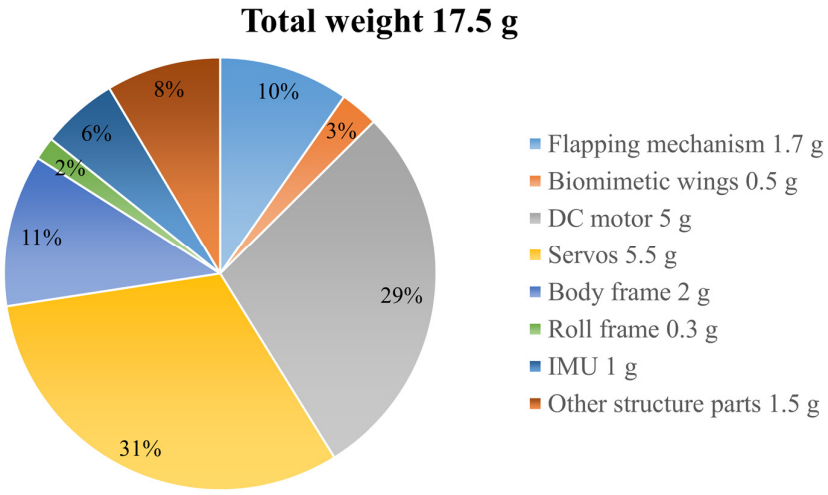

Figure 3.2 Weight breakdown of the robot.

Table 3.1 Rotation range of each servo and the wing root bars in left-right and forward-backward directions.

	Left-right	Forward-backward
Servo 1	$-35°\sim35°$	$0°$
Servo 2/3	$0°$	$-60°\sim60°$
Wing root bars	$-6°\sim6°$	$-25°\sim25°$

composed of three digital servo motors integrated into a body frame. This frame was produced using UV (ultraviolet) curable resin (Clear Resin, Formlabs Inc., USA) through a LFS (low force stereolithography) 3D printing process, utilizing the Form 3+ printer (Formlabs Inc., USA). The frame was then securely glued to the DC motor powering the flapping mechanism. Its vertical position was manually adjusted to ensure there was sufficient space for the unimpeded movement of the wing root bars. Servo 1 (FH-1083, Flash Hobby Technology Co., Ltd., China) was mounted onto the body frame, while Servos 2 and 3 (FH-2502, Flash Hobby Technology Co., Ltd., China) were held by a roll frame and hung from Servo 1 via a four-bar linkage system, enabling Servo 1 to control the lateral movement of Servos 2 and 3.

3.1.2 Control principles

Figure 3.3 illustrates the mechanisms for generating control torques around the CoG of the robot's body by modulating wing tension and the neutral position of

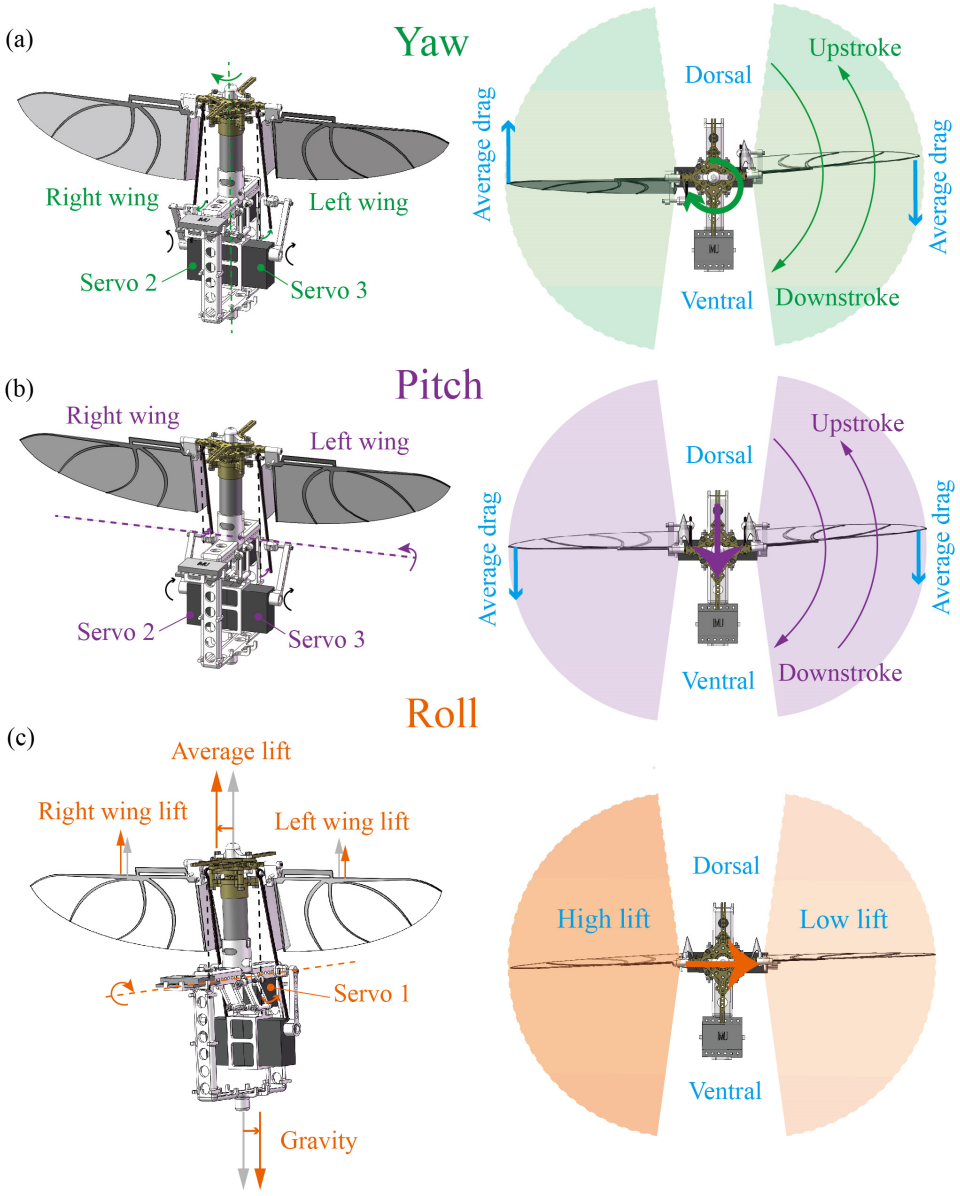

Figure 3.3 Control mechanisms and principles for yaw (a), pitch (b), and roll (c). The neutral positions of wing torsion were modulated by Servos 2 and 3 to generate yaw and pitch torque, the wing tension and lateral positions of Servos 2 and 3 were modulated by Servo 1 to generate roll torque.

wing torsion. The rotation arms of Servos 2 and 3 are loosely connected with the wing root bars via a slider-crank mechanism so that rotations of Servos 1, 2, and 3 move the wing root bars left or right, forward or backward, realizing modulation of

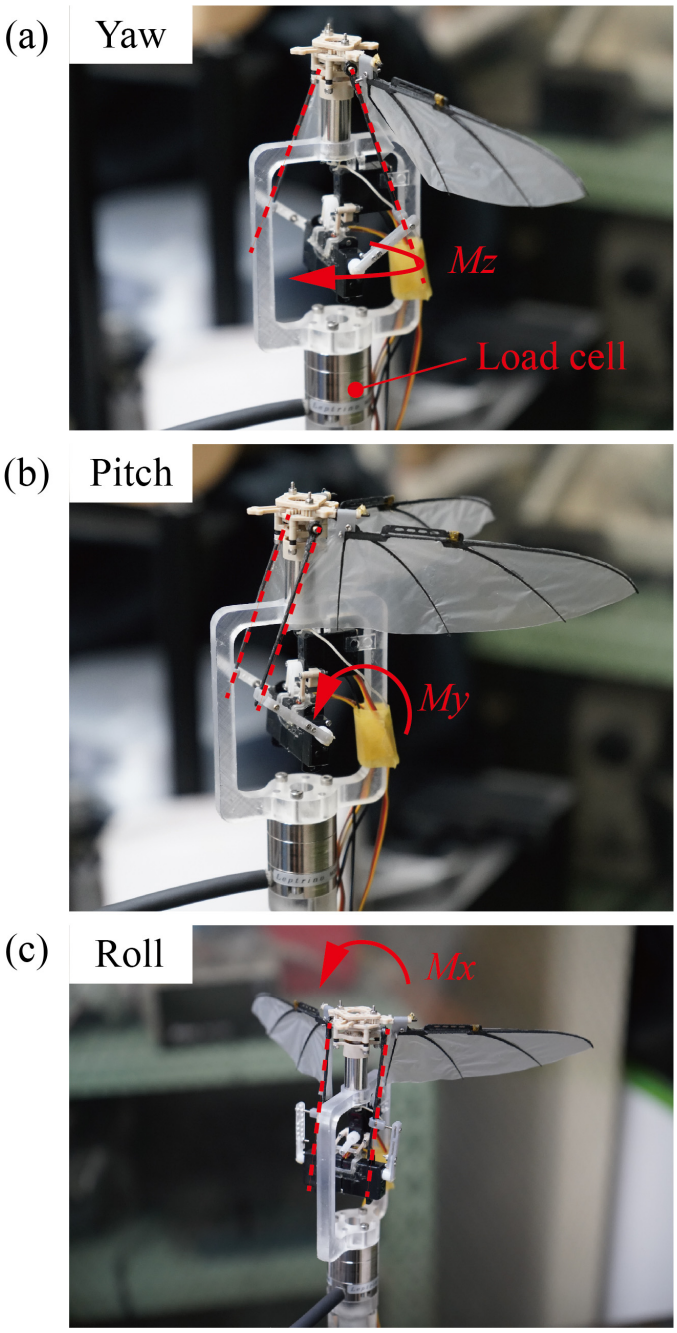

Figure 3.4 Experiment setup to measure yaw torque (a), pitch torque (b), and roll torque (c). The robot was mounted on a 6-axis load cell and the rotation angles of the servos were manually controlled.

the tension of the wing membrane and neutral position of the wing torsion. The

specific rotation range for each servo motor and the wing root bars, in both left-right and forward-backward directions, is detailed in Table 3.1.

In our flapping wing design, increasing wing torsion results in a smaller AoA, leading to reduced drag. On the other hand, increasing tension of the wing membrane increases lift. These characteristics were utilized to generate torque for attitude control as follows. As depicted in Figure 3.3 (a), applying opposite torsion to the left and right wings causes opposite average drag, thus generating yaw torque. Figure 3.3 (b) shows that applying torsion in the same direction causes average drag in the same direction, generating pitch torque. As seen in Figure 3.3 (c), varying the tension between the left and right wings through the actuation of Servo 1 causes asymmetrical lift, thereby generating roll torque. Additionally, the shift in CoG caused by the lateral movement of Servos 2 and 3 also contributes to the roll torque generation. The above control principles are similar to those discussed in the previous study [72].

3.2 Force and torque measurement

3.2.1 Experiment setup

To thoroughly evaluate the effectiveness of the attitude control mechanism, the robot was vertically mounted on a 6-axis load cell (PSF020, Leptrino Co., Ltd., Japan) to measure the lift and torque during flapping, as shown in Figure 3.4. The CoG of the robot was aligned on the *Fz* axis and the robot's forward direction was aligned parallel to the Fx axis of the load cell, ensuring accurate measurement of the key forces and torques involved: *Mx* for roll torque, *My* for pitch torque, *Mz* for yaw torque, and *Fz* for lift force.

During the measurement process, the flapping frequency of the robot was consistently maintained at 20 Hz. This specific frequency was selected following preliminary tests, which demonstrated its ability to generate sufficient lift while remaining within the safe operational range of the biomimetic wing. Additionally, the rotation angles of the wing root bars were manually adjusted within their ranges, from 0° to the maximum value, for each axis of control.

3.2.2 Results

The measurement data was collected under controlled conditions to ensure repeatability and accuracy. Each set of measurement was recorded over multiple flapping cycles to account for any variations or anomalies in the robot's

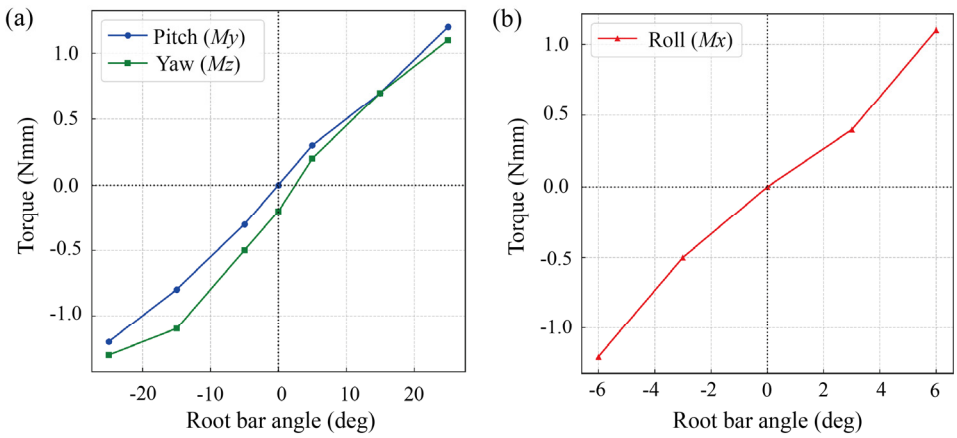

Figure 3.5 Measurement results of yaw torque (a), pitch torque (a), and roll torque (b).

performance. The data from the load cell was logged and then processed via a low-pass filter using a specialized software. The measurement results are shown in Figure 3.5. The control mechanism generated a maximum roll toque of 1.2 Nmm, a maximum pitch torque of 1.2 Nmm, and a maximum yaw torque of 1.3 Nmm at the frequency of 20 Hz. These torque values exhibited a generally linear increase corresponding to the escalating rotation angles of the wing root bars.

3.3 Summary

This chapter introduced the development of an attitude control mechanism for the flapping-wing aerial robot, focusing on the design, fabrication, principles of wing modulation, and evaluation. It details the fabrication of the control mechanism using 3D printed components and three digital servo motors, which facilitate precise control over wing tension and neutral positions of wing torsion. The effectiveness of this mechanism is evaluated using a 6-axis load cell, with results indicating a linear correlation between the rotation angle of wing root bars and the generated torques. The findings, shown in Figure 3.5, demonstrated the mechanism's capability in generating control torques for attitude control.

Chapter 4
Attitude controller

4.1 Architecture of the controller

4.1.1 Three-loop feedback structure

In this chapter, the core focus is on the development and implementation of an attitude controller that employs a three-loop feedback structure (3L-DOB) [74]. Block diagram of this controller is shown in Figure 4.1, it features three loops including the first loop, the second loop, and the adaptive loop. The first loop processes feedback from the attitude angle error, functioning analogously to the proportional element in a PID controller. The second loop utilizes feedback from the angular rate error, paralleling the derivative component of a PID controller. The core part of the controller is the adaptive loop, it incorporates an adaptive term based on a disturbance observer [78]. This loop is the key differentiator from conventional PD and PID controllers, providing the system with the ability to adapt in real-time to unknown disturbances and modeling errors. Update rates of these controllers are set to 50 Hz.

Specifics of the 3L-DOB controller are detailed as follows. The closed-loop dynamics can be formulated as

$$u = Gain_2(\omega_c - \omega) - \Delta, \tag{3}$$

$$\omega_c = Gain_1(\theta_c - \theta), \tag{4}$$

where ω is a present angular velocity (rad/s), u is the controller output to the servo motors (deg), $Gain_2$ is the gain of the second loop, ω_c is the target angular velocity (rad/s), Δ is the model uncertainty, $Gain_1$ is the gain of the first loop, θ_c is the target attitude angle (deg), θ is the present attitude angle (deg).

Given the complexity and difficulty in precisely calculating actual model uncertainty, $\hat{\Delta}$ is introduced as the estimated model uncertainty. It is assumed that the model uncertainty varies slowly in comparison to the observer dynamics. Thus,

$$\dot{\Delta} = 0. \tag{5}$$

The observer error is defined as

$$\tilde{\Delta} \triangleq \Delta - \hat{\Delta}. \tag{6}$$

The desired error dynamics for the observer error is chosen as first-order system,

$$\dot{\tilde{\Delta}} + K\tilde{\Delta} = 0, \tag{7}$$

where K is the adaptive loop gain. To ensure the observer error adheres to the desired dynamics, the disturbance observer is structured as

$$\dot{\hat{\Delta}} = K\left(\Delta - \hat{\Delta}\right) = K\left(u - Gain_2(\omega_c - \omega) - \hat{\Delta}\right). \tag{8}$$

An auxiliary variable z is defined as

$$z = \hat{\Delta} + K(\omega_c - \omega). \tag{9}$$

The time derivative of z is then expressed as

$$\dot{z} = \dot{\hat{\Delta}} - Ku + L\dot{K} = -K\left(Gain_2(\omega_c - \omega) + \hat{\Delta}\right). \tag{10}$$

Then, the estimated model uncertainty $\hat{\Delta}$ is given by

$$\hat{\Delta} = z - K(\omega_c - \omega). \tag{11}$$

By replacing the model uncertainty Δ with the estimated one $\hat{\Delta}$, the control input u is expressed as

$$u = Gain_2(Gain_1(\theta_c - \theta) - \omega) - \hat{\Delta}. \tag{12}$$

4.1.2 Conventional PD and PID controller

To facilitate a comparative analysis of control performance, conventional PD and PID controllers were also implemented alongside the attitude controller. The block diagram for these conventional controllers is depicted in Figure 4.2. The PD controller consists of a proportional element and a derivative element. The control action in a PD controller is a combination of these two elements acting on the error signal, which is the difference between the target and actual attitude angles. The proportional component produces an output that is proportional to the current error. The *Kp* (proportional gain) determines the ratio of output response to the error signal. Higher *Kp* values result in a larger response to the error, leading to faster system response but potentially causing overshoot and instability. The derivative component reacts to the rate of change of the error, providing a predictive control action. It helps in damping the system response and reducing overshoot. The *Kd* (derivative gain) adjusts the sensitivity of the controller to the rate of change of the error.

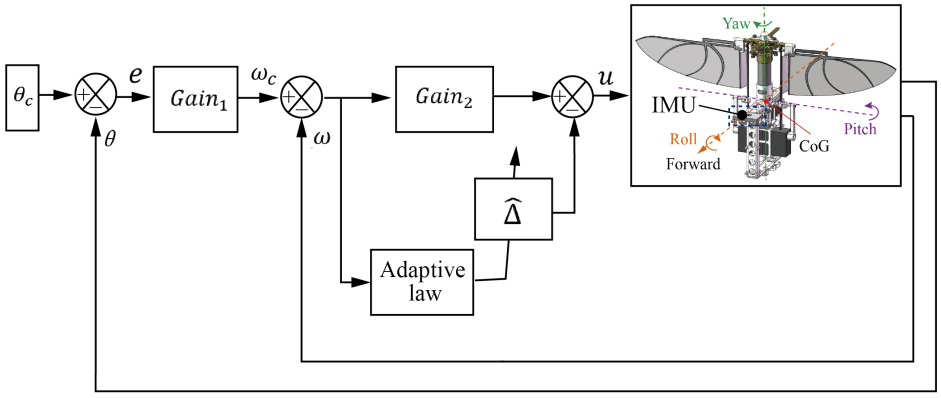

Figure 4.1 Block diagram of the attitude controller employing a three-loop feedback structure.

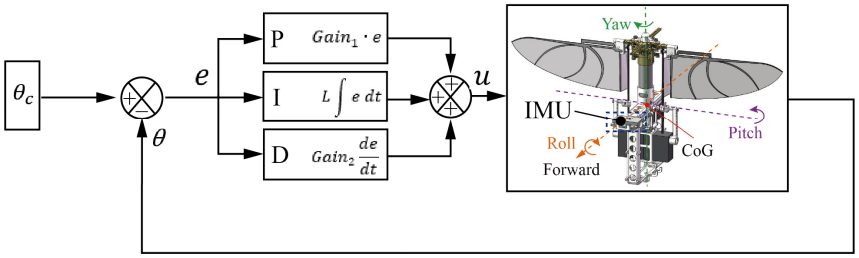

Figure 4.2 Block diagram of the conventional PD/PID controllers.

The PID controller adds an integral component to the PD control structure. The integral component addresses the accumulation of past errors, providing a corrective action that depends on the cumulative error over time. It helps eliminate steady state errors and improves control accuracy. The *Ki* (integral gain) determines how aggressively the controller reacts to accumulated errors.

The PD controller is easier to tune compared to the PID controller. They are effective in systems where rapid response is essential, and steady-state error is not a critical concern. Their predictive nature, due to the derivative term, aids in stabilizing systems prone to overshoot. However, the absence of an integral term means PD controllers cannot completely eliminate steady-state errors. They might not be suitable for systems where long-term accuracy is critical.

The inclusion of the integral term allows the PID controller to correct steady-state errors, leading to higher accuracy in systems where long-term precision is essential. The PID controller provide a balanced approach, suitable for a wide range

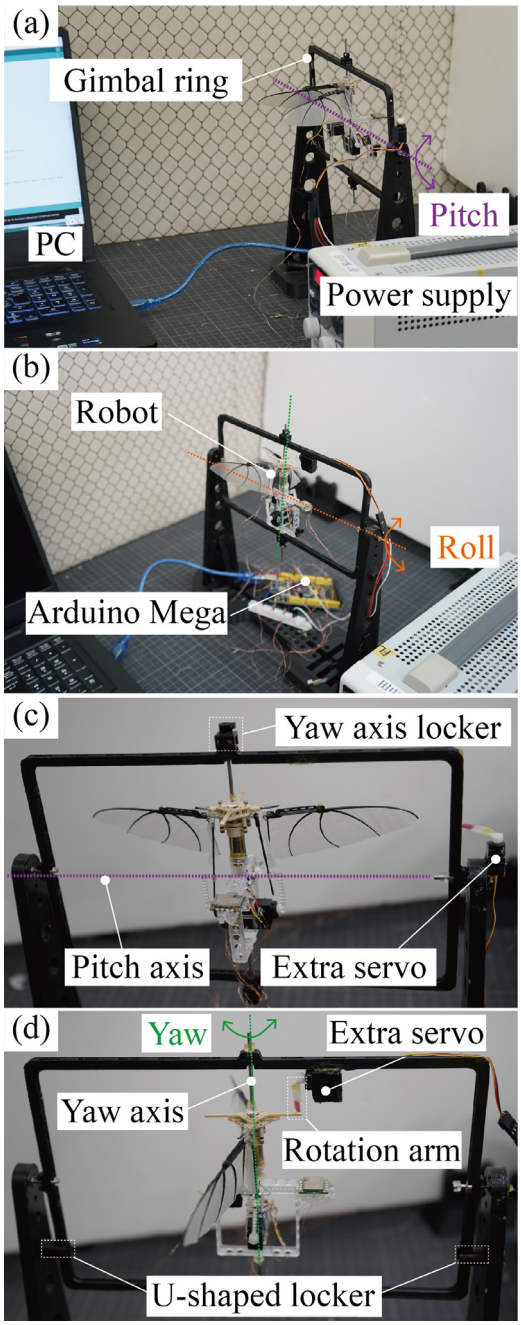

Figure 4.3 Semi-tethered experiment setup using a gimbal mechanism. (a) and (c) show the overview and detailed view of the pitch experiment setup, (b) and (d) present the overview and detailed view of the roll and yaw experiment setup.

of control applications. However, the complexity in tuning a PID controller is higher,

especially in systems with dynamic changes. Incorrect tuning can lead to poor performances, such as oscillation, slow response, and overshoot.

4.2 Performance evaluation through semi-tethered experiments

4.2.1 Gimbal mechanism

The developed flapping-wing aerial robot was mounted on a 3D printed gimbal mechanism to evaluate the controllers' performance as similar to the previous work by Phan *et al*. [20] and Shimura *et al*. [75]. The gimbal mechanism allowed roll, pitch, and yaw rotations, while translations were restricted. The robot was mounted at the gimbal ring's mid-vertical axis via two metal rods (Figure 4.3 (a)). These rods were supported by bearings in the gimbal ring, permitting free yaw rotation (Figure 4.3 (d)). The CoG of the robot was aligned on the yaw axis. The yaw, pitch, and roll rotations of the gimbal were mechanically limited to –90°, –75°, and –75°, respectively.

The DC motor was connected to an external power supply (PA18-2B, Texio Technology Co., Ltd., Japan). The servo motors and the IMU were connected to an Arduino Mega 2560 microcontroller board via 600-mm-long enameled wires of 0.1-mm diameter. The microcontroller board was placed on the floor just beneath the robot with sufficient room for the gimbal to rotate. The microcontroller supplied power to the servo motors and the IMU, collected translational acceleration, angular velocity, and geomagnetic field strength data from the IMU, computed the attitude angle by fusing the collected 9-axis data through an attitude estimation algorithm provided by the manufacturer, run the controller code to generate the control input, and sent the control input to the servo motors to stabilize the attitude.

4.2.2 Experiment design

Roll, pitch, and yaw experiments were separately conducted, that is, a single-axis rotation was permitted while the other two axes were restrained using mechanical lockers. In yaw experiments, the gimbal ring was completely fixed using two U-shaped lockers (Figure 4.3 (d)), allowing rotation solely around the yaw axis. An extra servo motor on the top of the gimbal ring provided an instantaneous disturbance in yaw to the robot by hitting the robot with the rotation arm.

For pitch and roll experiments, the yaw axis was locked using the yaw axis

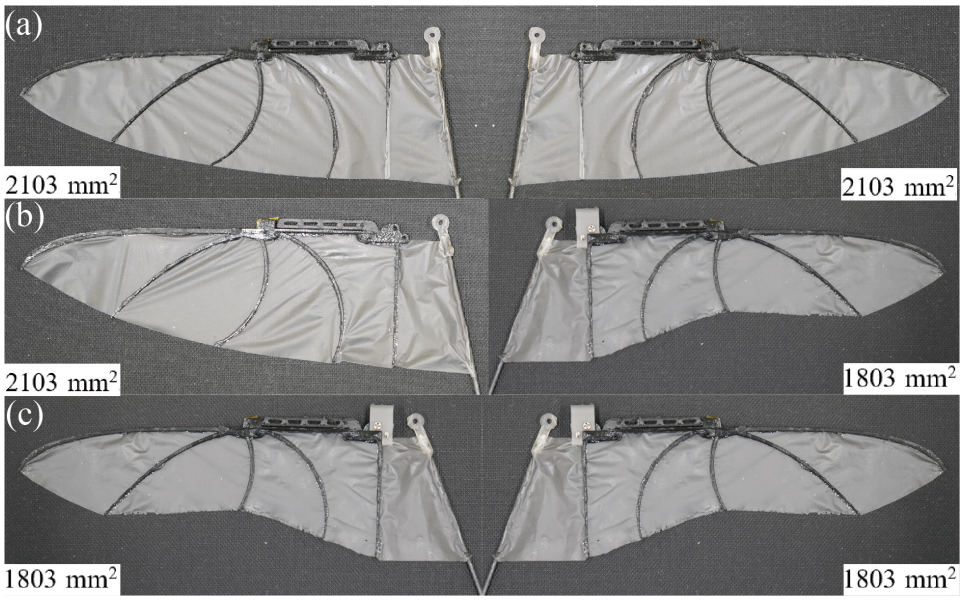

Figure 4.4 (a) Wing Set 1 (no area loss): a pair of original wings, (b) Wing Set 2 (asymmetrical area loss): left wing is original wing, right wing is molting wing, (c) Wing Set 3 (symmetrical area loss): a pair of molting wings.

locker. To allow pitch rotation, the robot was fixed so that the front-back direction was vertical to the roll and yaw axes (Figure 4.3 (c)). In roll experiments, the front-back direction was parallel to the roll axis (Figure 4.3 (b)). The position of the robot was adjusted so that CoG was on the pitch and roll axes. An extra servo motor was used to provide disturbance as same as the yaw experiments.

Three different sets of wings were tested in this chapter. Wing Set 1 was a pair of original wings (Figure 4.4 (a)). In Wing Set 2, left wing was the original wing and right wing was the molting wing (Figure 4.4 (b)). Wing Set 3 was a pair of molting wings (Figure 4.4 (c)). To measure the average lift and control torque generated by each Wing Set, the robot was vertically mounted on the load cell, utilizing the same experiment setup as described in Chapter 3.2.1. The results, presented in Figure 4.5, revealed that Wing Set 2 generated 7.1% less lift compared to Wing Set 1, while Wing Set 3 produced 11.3% less lift than Wing Set 1 when operating at the flapping frequency of 20 Hz.

As introduced in Chapter 4.1, three controllers were tested: the conventional PD and PID controllers and the 3L-DOB controller. Each controller was tested with three different Wing Sets for each rotation (i.e., yaw, pitch, and roll). Three trials

Table 4.1 Controller parameters for each rotation.

		PD	PID	3L-DOB
Yaw	$Gain_1$ (no unit or $\frac{\text{rad/s}}{\text{deg}}$)*	0.32	0.33	0.35
	$Gain_2$ (s or $\frac{\text{deg}}{\text{rad/s}}$)**	0.03	0.025	0.03
	L (1/s)	0	0.01	0.01
Pitch	$Gain_1$ (no unit or $\frac{\text{rad/s}}{\text{deg}}$)*	0.41	0.38	0.4
	$Gain_2$ (s or $\frac{\text{deg}}{\text{rad/s}}$)**	0.025	0.03	0.03
	L (1/s)	0	0.01	0.015
Roll	$Gain_1$ (no unit or $\frac{\text{rad/s}}{\text{deg}}$)*	0.12	0.13	0.12
	$Gain_2$ (s or $\frac{\text{deg}}{\text{rad/s}}$)**	0.02	0.01	0.015
	L (1/s)	0	0.01	0.01

*PD and PID controllers have no physical unit. 3L-DOB controller has the physical unit of $\frac{\text{rad/s}}{\text{deg}}$.

**PD and PID controllers have the physical unit "s". 3L-DOB controller has the physical unit of $\frac{\text{deg}}{\text{rad/s}}$.

were conducted for each experiment to obtain average data. All experiments were performed at a consistent flapping frequency of 20 Hz. The recording started at 0 s, followed by manual start of the flapping. Then, the disturbance was applied at 3 s. The initial attitudes of yaw, pitch, and roll are shown in Figure 4.3. The primary control objective was to recover from the extra disturbance and maintain the initial attitude. Gains, shown in Table 4.1, for each controller in all motions were manually tuned with Wing Set 1 as follows. Firstly, I and D gains (L, $Gain_2$) were set to be zero, and P gain ($Gain_1$) was increased from zero until an overshoot occurred, followed by fine tuning around that value. Then, I gain was increased so that residual error after long period was minimized. Finally, D gain was increased to minimize the overshoot and settling time. These tuned feedback gains were consistently applied to subsequent Wing Sets to test the controllers' robustness to wing defects.

The control performance was evaluated by recovery rate (deg/s), RMS (root mean square) error (deg), and overshoot (deg), similar metrics were also used in previous work by Lee *et al*. [47] and Shiomura *et al.* [75]. The recovery rate reflects

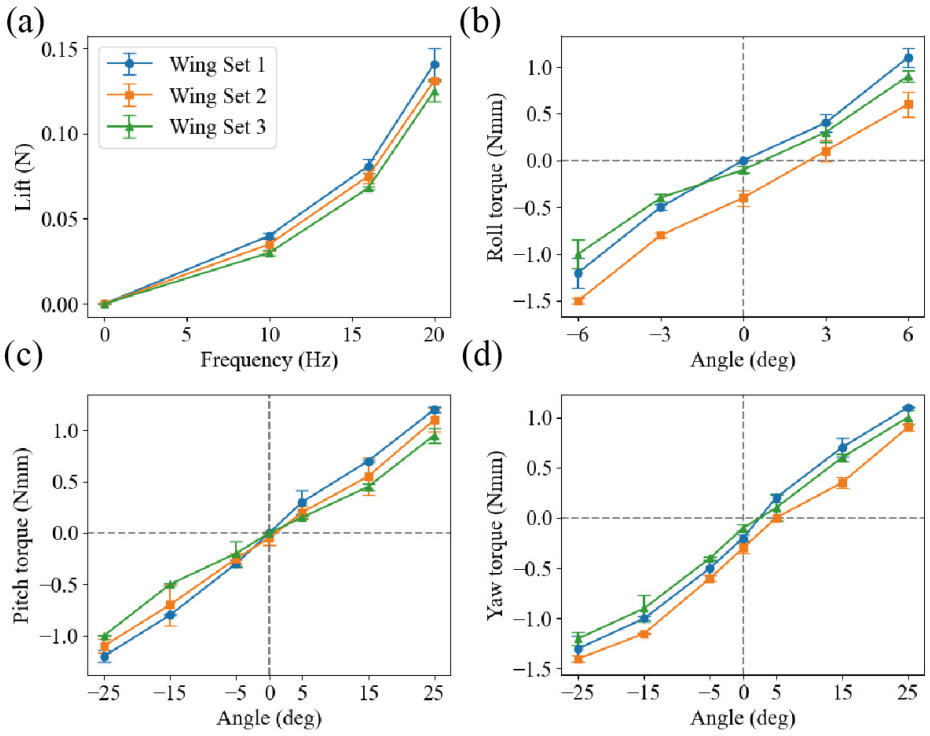

Figure 4.5 Measured lift (a), roll torque (b), pitch torque (c), and yaw torque (d) for each Wing Set. Each error bar indicates the standard deviation.

the robot's speed in returning to the initial state from the point of maximum attitude error, serving as an indicator of the controller's responsiveness. For yaw control, given the robot's rapid recovery, the recovery rate was calculated by dividing the maximum attitude error by the recovery time, defined as the duration from the moment of peak error to the moment when the attitude error firstly reached zero before overshooting. For pitch and roll control (Figure 4.6), the attitude error sometimes did not return to zero before 5.5 s. In that case, the recovery rate was calculated based on the duration from the timing when the error was maximized to 5.5 s. The RMS error was calculated based on the period of 5 to 8 s as a metric for accuracy. Overshoot, which indicates the controller's stability, is determined by the maximum positive attitude error: before 4.5 s for yaw control, and before 6 s for pitch and roll control. Together, these three metrics offer a comprehensive evaluation of the controller's performance, capturing both its responsiveness, accuracy, and stability in maintaining the initial attitude under varying conditions.

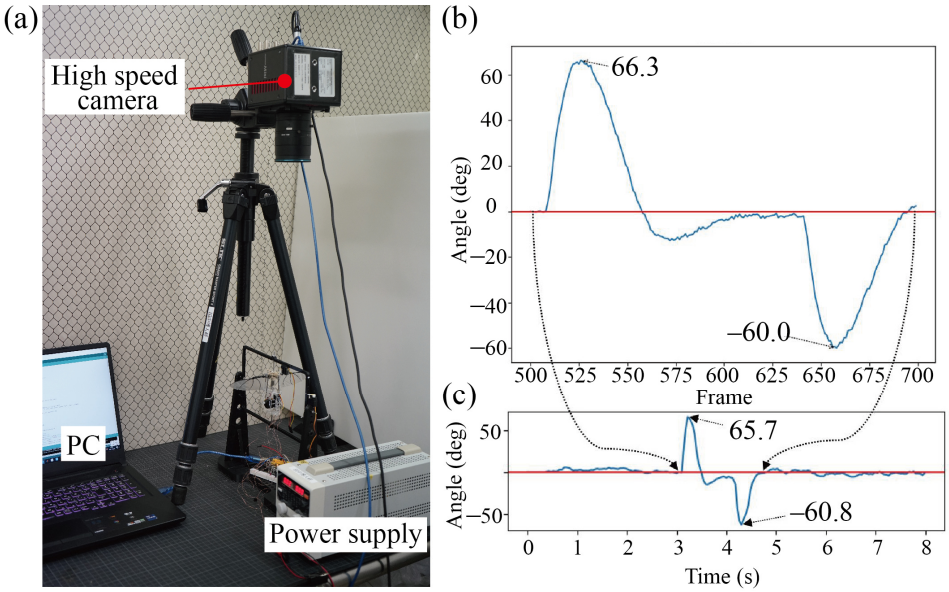

Figure 4.6 Verification of the attitude angle calculated from IMU. (a) Experiment setup using a high-speed video camera, (b) the attitude angle calculated from motion analysis, (c) the attitude angle calculated from IMU.

4.2.3 Attitude angle calculation and verification

The attitude angle of roll, pitch, and yaw were calculated by fusing data from the accelerometer, gyroscope, and magnetometer of the IMU sensor, encompassing linear acceleration, angular rate, and magnetic field vectors. To validate the calculated attitude angles, a motion analysis of the attitude rotation was performed using a high-speed video camera as depicted in Figure 4.6 (a), employing a methodology similar to the wing motion analysis detailed in Chapter 2.3.3. Specifically, the high-speed camera was positioned above the robot to capture yaw rotation from a top view, operating at a frame rate of 2000 frames/s and an image resolution of 1024×1024 pixels. The yaw angle was subsequently calculated using Dipp Motion software. The yaw angle change as determined from the IMU sensor data is presented in Figure 4.6 (c), while the yaw angle change ascertained from motion analysis is depicted in Figure 4.6 (b). The comparative results demonstrate a maximum error of less than 1° at the maximum and minimum error positions, demonstrating the accuracy of the calculation method using IMU.

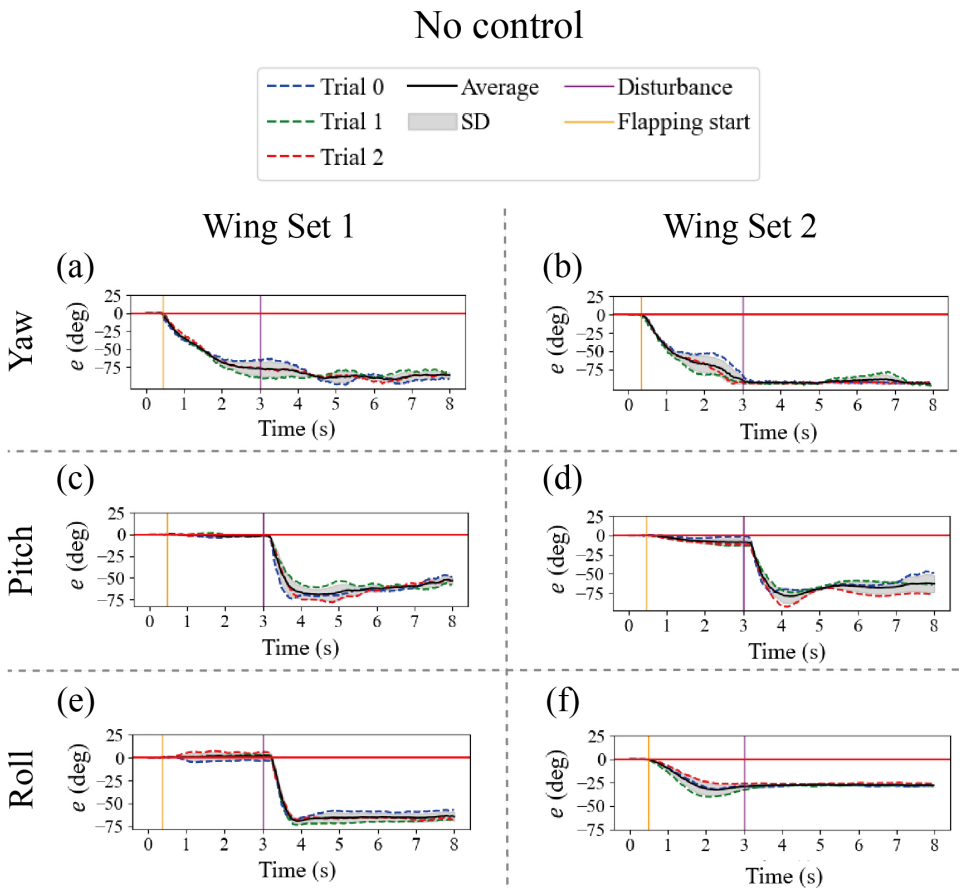

Figure 4.7 Attitude error e without feedback control with Wing Set 1 in yaw (a), pitch (c), and roll (e), and with Wing Set 2 in yaw (b), pitch (d), and roll (f).

4.2.4 Attitude change without control

Figure 4.7 demonstrates response of the robot with Wing Set 1 and Wing Set 2 when there is no feedback control. Flapping frequency was set to be 20 Hz. The recording started at 0 s, followed by manual start of flapping. The disturbance was provided at 3 s except for the yaw rotation of Wing Set 1 and roll rotation of Wing Set 2, where the robot failed to maintain its initial attitude before 3 s. Measurement was conducted 3 ti mes for each rotation. In pitch and roll rotations with Wing Set 1 (Figure 4.7 (c, e)), the robot maintained the initial attitude before the disturbance was provided (0–3 s). After the application of the disturbance (3 s), the robot kept on rotating until reached the limitation angle and did not recover to the initial attitude. In yaw reaction (Figure 4.7 (a)), the robot started rotating from 0 s and

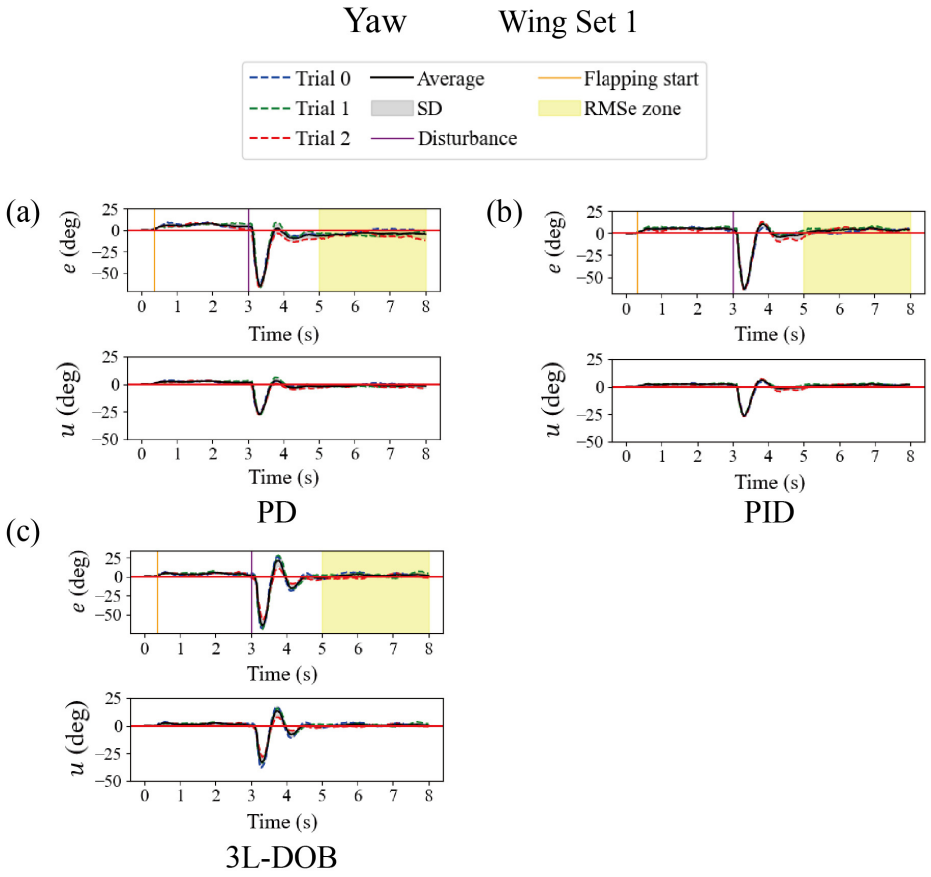

Figure 4.8 Attitude error e and control input u in yaw experiments with Wing Set 1. PD controller (a), PID controller (b), and 3L-DOB controller (c).

stopped at the limitation angle, that is assumed to be due to asymmetry between left and right wing structures and motions attributed to fabrication error. With Wing Set 2, initial roll rotation before the disturbance was more notable and the initial yaw rotation seemed to be faster (Figure 4.7 (f, b)), these are assumed to be due to the increased asymmetry by the wing defect.

4.2.5 Results and discussion

A. Yaw experiments

The time variations in the yaw angle and output to the yaw servo motor with Wing Sets 1, 2, and 3 are shown in Figure 4.8, Figure 4.9, and Figure 4.10, the performance is summarized in Table 4.2. The reaction of the 3L-DOB controller

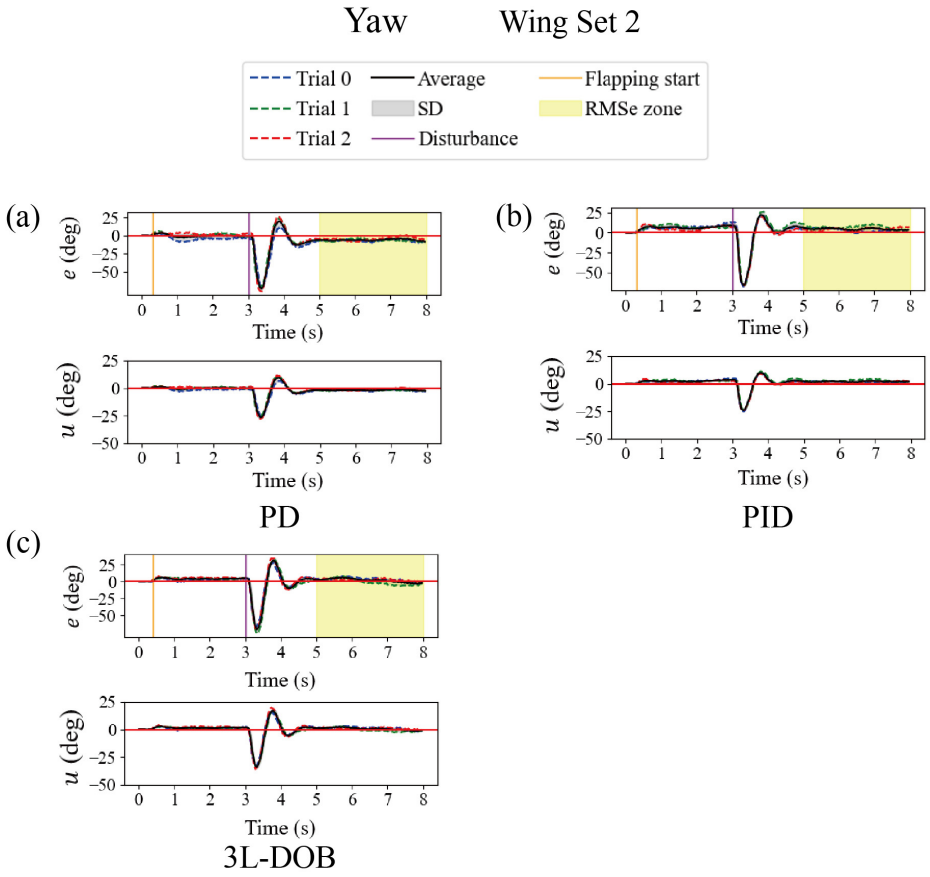

Figure 4.9 Attitude error e and control input u in yaw experiments with Wing Set 2. PD controller (a), PID controller (b), and 3L-DOB controller (c).

emerged as the most responsive, achieving recovery rates between 221.4 to 241.2 deg/s across all Wing Sets, highlighted by the highest pooled mean recovery rate of 231.7 deg/s and the lowest pooled standard deviation of 8.1 deg/s (Table 4.2). This consistency underscores the 3L-DOB controller's robustness to different wing defects. Conversely, the PD and PID controllers exhibited more variation in the recovery rate, indicating high sensitivity to wing defects. The asymmetry in Wing Set 2 initiated a yaw torque, contributing to its superior recovery rate under PD control.

In terms of accuracy, a gradual increase in RMS error was noted from Wing Set 1 to Wing Set 3 for all controllers (Table 4.2), indicating a correlation between the wing defect and control accuracy. The 3L-DOB controller consistently

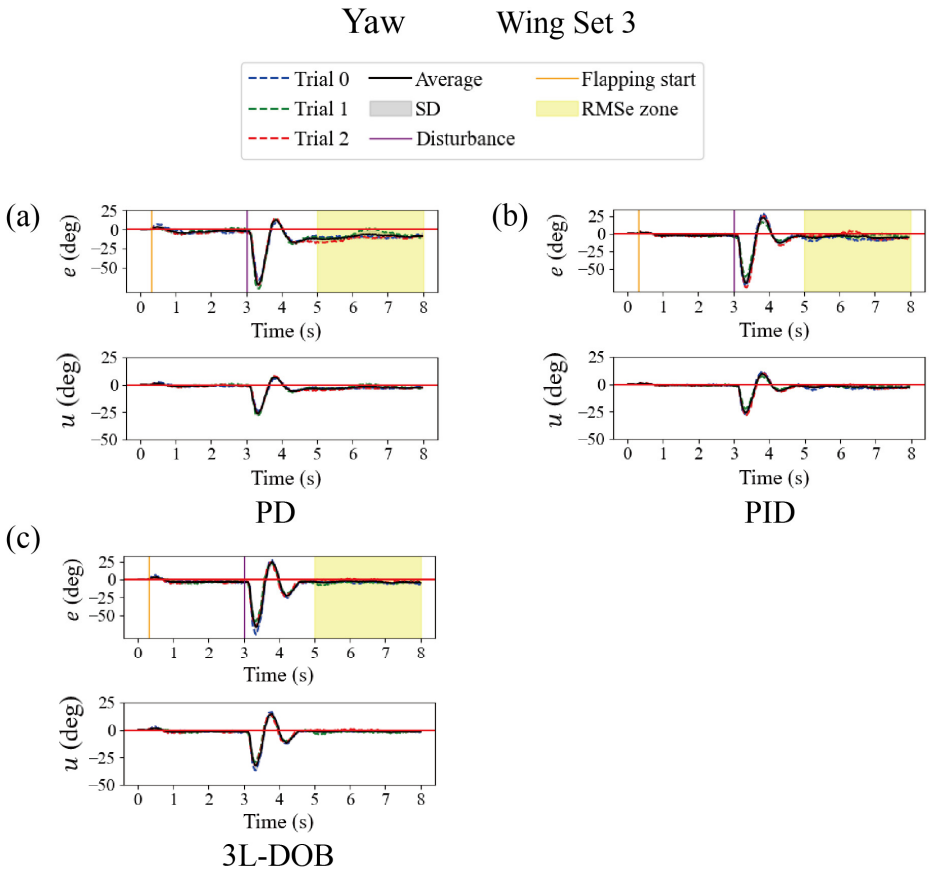

Figure 4.10 Attitude error e and control input u in yaw experiments with Wing Set 3. PD controller (a), PID controller (b), and 3L-DOB controller (c).

demonstrated the lowest RMS error among the three controllers for all Wing Sets, where its pooled mean was 3.1 degrees. The standard deviation of the pooled mean was also the smallest, that is 0.6 degrees. Thus, the 3L-DOB controller combines both robustness and accuracy in yaw control. On the other hand, PID controller also showed the same standard deviation in the pooled mean of RMS error (0.6 degrees), indicating its robustness to wing defects.

Despite the 3L-DOB controller's good performance in responsiveness and accuracy, its higher overshoot figures, especially in Wing Sets 2 and 3, indicate an area for improvement. The observed increase in overshoot across all controllers when transitioning from Wing Set 1 to Wing Sets 2 and 3 underscores the significant

Table 4.2 Means and standard deviations of the recovery rates, RMS errors, and overshoot for three measurements in yaw experiments. Pooled mean and its standard deviation for the mean values were also shown.

		PD	PID	3L-DOB
Recovery rate (deg/s)	Wing Set 1	155.9 (100%) ± 20.3	174.9 (100%) ± 2.9	221.4 (100%) ± 15.3
	Wing Set 2	216.6 (139%) ± 21.9	216.7 (124%) ± 7.8	232.3 (105%) ± 9.8
	Wing Set 3	198.7 (127%) ± 25.8	208.5 (119%) ± 31.1	241.2 (109%) ± 11.7
	Pooled mean*	190.4	200.0	231.7
	Pooled s.d.*	25.4	18.1	8.1
RMS error (deg)	Wing Set 1	4.6 (100%) ± 1.9	3.6 (100%) ± 1.1	2.3 (100%) ± 0.38
	Wing Set 2	6.0 (130%) ± 1.1	4.3 (119%) ± 1.5	3.4 (148%) ± 0.7
	Wing Set 3	9.4 (204%) ± 2.1	5.0 (139%) ± 1.7	3.7 (161%) ± 1.3
	Pooled mean*	6.7	4.4	3.1
	Pooled s.d.*	2.0	0.6	0.6
Overshoot (deg)	Wing Set 1	3.7 (100%) ± 4.0	10.3 (100%) ± 2.9	21.4 (100%) ± 7.5
	Wing Set 2	20.6 (557%) ± 5.8	22.4 (217%) ± 2.6	31.2 (146%) ± 2.6
	Wing Set 3	12.9 (349%) ± 1.5	23.1 (224%) ± 5.0	25.1 (117%) ± 1.5
	Pooled mean*	12.4	18.6	25.9
	Pooled s.d.*	6.9	5.9	4.0

*Calculated from the mean values for Wing Sets 1 to 3.

impact of wing defects on the robot's aerodynamic profile and the resultant challenges in disturbance counteraction. This increased overshoot reflects the controllers' struggle to efficiently stabilize the robot amidst the altered aerodynamic forces and moments, highlighting a critical consideration for control strategy

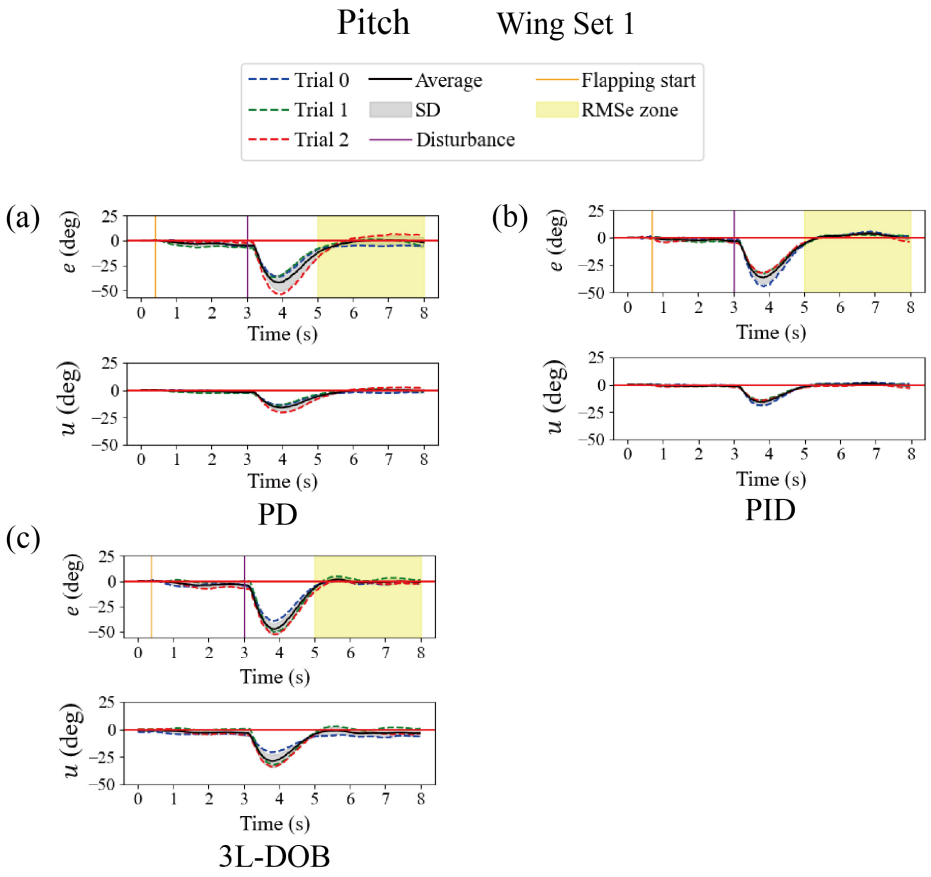

Figure 4.11 Attitude error e and control input u in pitch experiments with Wing Set 1. PD controller (a), PID controller (b), and 3L-DOB controller (c).

optimization.

B. Pitch experiments

The pitch experiment results with Wing Sets 1, 2, and 3 are illustrated in Figure 4.11, Figure 4.12, and Figure 4.13, the performance is summarized in Table 4.3. Despite the increased weight imposed by the gimbal ring, all controllers facilitated recovery from disturbances, exhibiting varying degrees of recovery rate, RMS error, and overshoot.

The findings highlighted the 3L-DOB controller's superior recovery rate across all Wing Sets, achieving a pooled mean recovery rate of 28.1 deg/s, thereby underscoring its responsiveness in pitch control under conditions of wing defects.

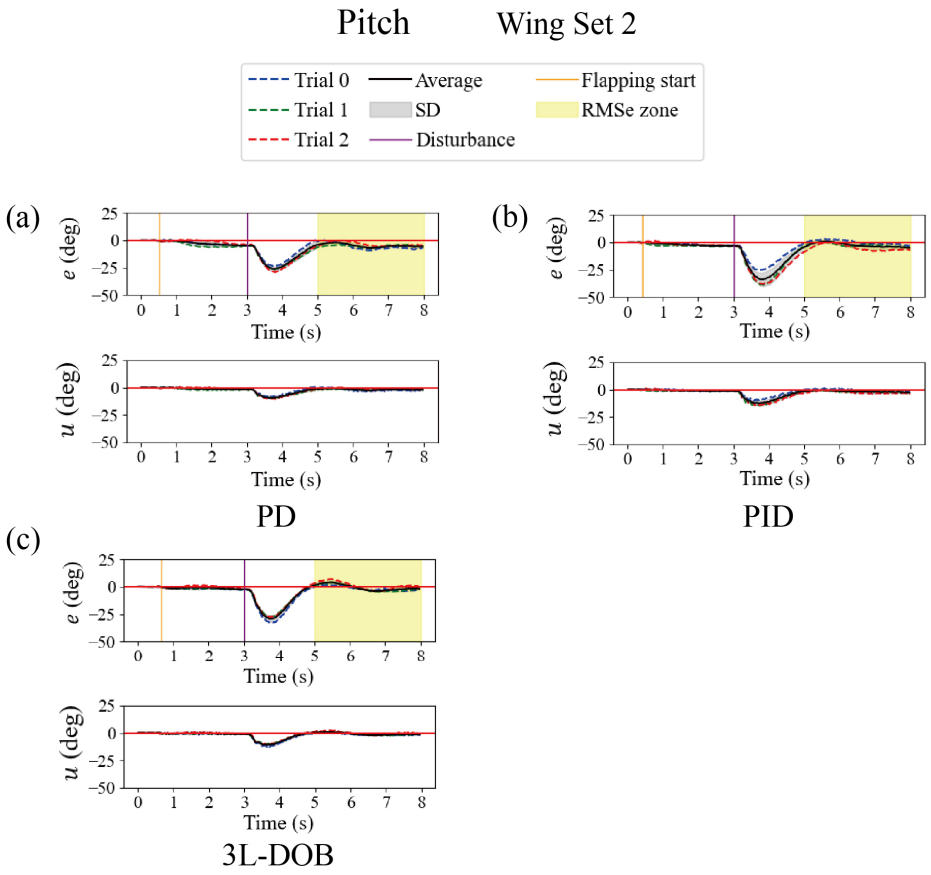

Figure 4.12 Attitude error e and control input u in pitch experiments with Wing Set 2. PD controller (a), PID controller (b), and 3L-DOB controller (c).

This is noteworthy given the increased weight of the gimbal ring, which inherently limits recovery rates in pitch and roll experiments relative to yaw. The PID controller, while trailing behind the 3L-DOB controller in pooled mean recovery rate (22.9 deg/s), showed the lowest pooled standard deviation (1.1 deg/s), reflecting its consistent performance and enhanced robustness in pitch control across varied wing defects. An intriguing observation was the universally lower recovery rates with Wing Set 2 across all controllers, suggesting that asymmetrical wing defect poses a potential challenge to pitch recovery. Conversely, the similarity in recovery rates between Wing Sets 1 and 3 indicates that symmetrical wing defect has a less pronounced effect on pitch control.

In terms of accuracy, as gauged by RMS error, the 3L-DOB controller showed

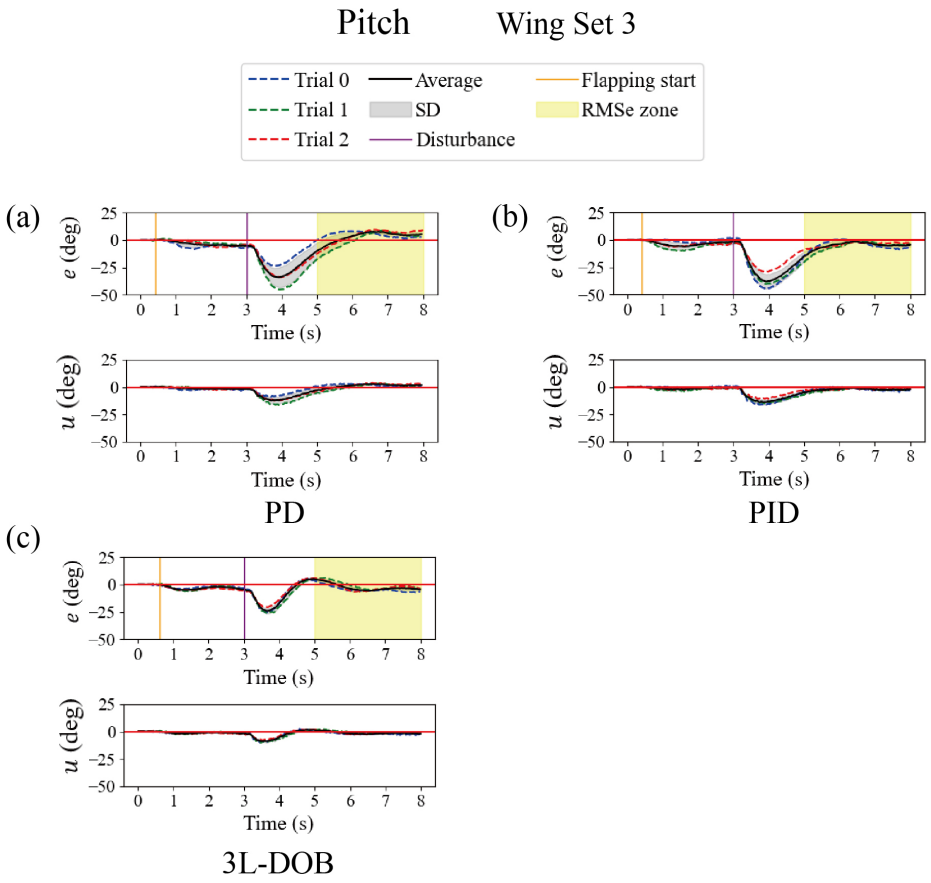

Figure 4.13 Attitude error e and control input u in pitch experiments with Wing Set 3. PD controller (a), PID controller (b), and 3L-DOB controller (c).

slightly better performance than PD and PID controllers across all Wing Sets, achieving the lowest pooled mean RMS error of 2.9 degrees. Interestingly, all three controllers displayed similar pooled standard deviation in RMS error, indicating their robustness in pitch control accuracy to wing defects.

While the PD and PID controllers exhibited minimal overshoot across all Wing Sets, the 3L-DOB controller's overshoot increased from Wing Set 1 to Wing Set 3, with a pooled mean of 3.9 degrees and a pooled standard deviation of 1.5 degrees. This trend underscores a potential area for improvement in the 3L-DOB controller's design, particularly in minimizing overshoot while maintaining responsiveness and accuracy.

Table 4.3 Means and standard deviations of the recovery rates, RMS errors, and overshoot for three measurements in pitch experiments. Pooled mean and its standard deviation for the mean values were also shown.

		PD	PID	3L-DOB
Recovery rate (deg/s)	Wing Set 1	26.8 (100%) ± 6.3	22.4 (100%) ± 3.3	30.9 (100%) ± 6.6
	Wing Set 2	16.3 (61%) ± 2.2	21.9 (98%) ± 3.2	25.4 (82%) ± 1.8
	Wing Set 3	21.8 (81%) ± 6.3	24.5 (109%) ± 3.8	28.2 (91%) ± 1.5
	Pooled mean*	21.6	22.9	28.1
	Pooled s.d.*	4.3	1.1	2.2
RMS error (deg)	Wing Set 1	4.4 (100%) ± 1.6	2.3 (100%) ± 0.4	2.2 (100%) ± 0.2
	Wing Set 2	4.8 (92%) ± 1.0	3.0 (130%) ± 1.4	2.7 (123%) ± 0.4
	Wing Set 3	5.9 (134%) ± 0.8	5.0 (217%) ± 0.6	3.9 (177%) ± 0.7
	Pooled mean*	5.0	3.5	2.9
	Pooled s.d.*	0.6	1.2	0.7
Overshoot (deg) **	Wing Set 1	-	-	1.9 (100%) ± 1.0
	Wing Set 2	-	-	4.3 (385%) ± 2.2
	Wing Set 3	-	-	5.6 (603%) ± 0.5
	Pooled mean*	-	-	3.9
	Pooled s.d.*	-	-	1.5

*Calculated from the mean values for Wing Sets 1 to 3.

**The symbol '-' means that the measurement or calculation was not possible.

C. Roll experiments

The results of roll experiment with Wing Sets 1, 2, and 3 are presented in Figure 4.14, Figure 4.15, Figure 4.16, the performance is summarized in Table 4.4. While all controllers demonstrated effectiveness in recovering the robot's roll for

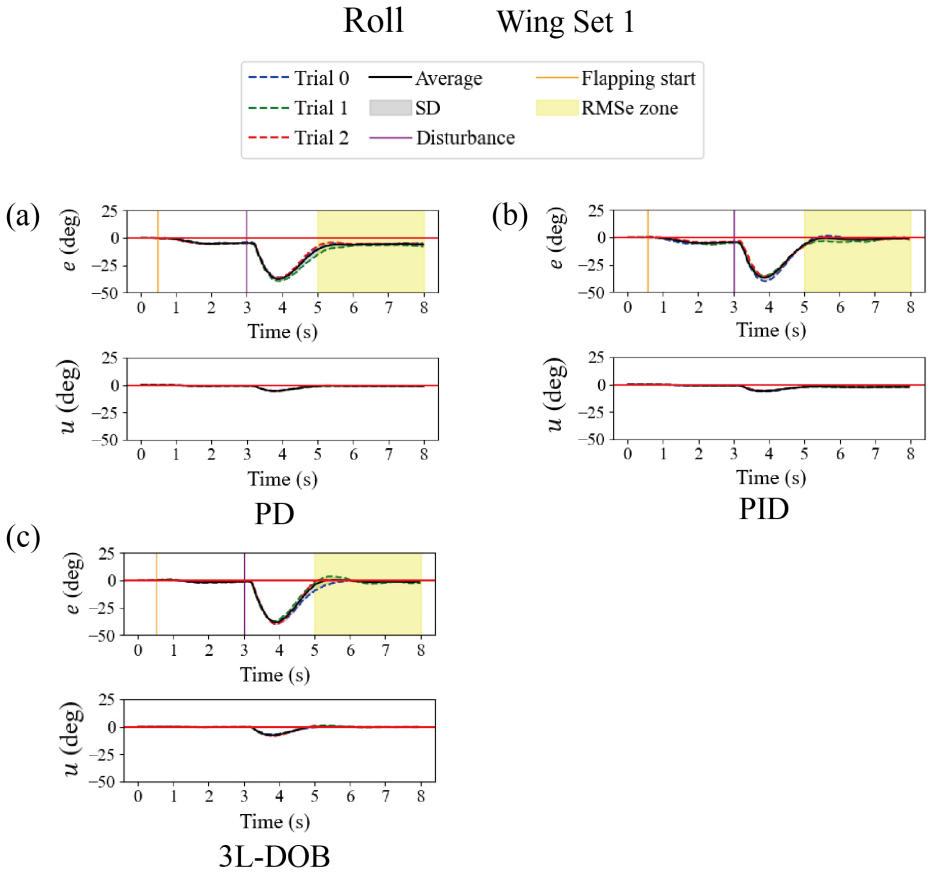

Figure 4.14 Attitude error e and control input u in roll experiments with Wing Set 1. PD controller (a), PID controller (b), and 3L-DOB controller (c).

the majority of Wing Sets, the PD controller's performance on Wing Set 2, characterized by asymmetrical wing defect, highlights a limitation in its effectiveness. The struggle of the PD controller with Wing Set 2 underscores its limitations in compensating for asymmetrical wing defect and the associated initial roll torque. Both the PID and 3L-DOB controllers experienced a negative shift during the initial 0–3 s in the presence of Wing Set 2's challenging conditions, yet their eventual recovery underscores a degree of resilience. This period of noticeable oscillation, particularly pronounced in the 5–8 s interval, elucidates the intricate balance required for accurate roll control amidst asymmetrically altered aerodynamics.

The 3L-DOB controller's performance, with the highest pooled mean recovery

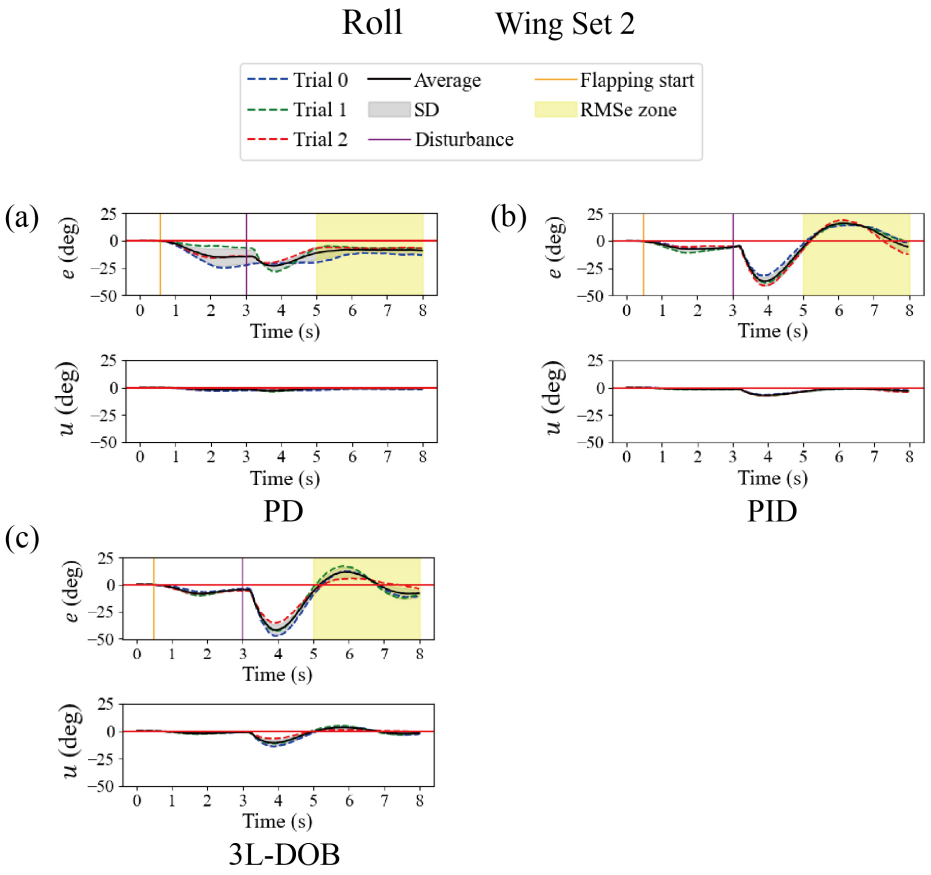

Figure 4.15 Attitude error e and control input u in roll experiments with Wing Set 2. PD controller (a), PID controller (b), and 3L-DOB controller (c).

rate of 28.6 deg/s, affirms its enhanced responsiveness in roll control. Conversely, the PID controller's lowest pooled standard deviation of 0.4 deg/s in recovery rate highlights its robustness to wing defects.

In terms of control accuracy evaluated by RMS error, both the PID and the 3L-DOB controllers showed increased error with Wing Set 2, directly correlating the challenges of asymmetrical wing defect with diminished roll control accuracy. Despite these hurdles, the 3L-DOB controller maintained the lowest RMS error across all Wing Sets, with a pooled mean RMS error of 4.2 degrees and the lowest pooled standard deviation of 2.3 degrees, underscoring its robustness in managing roll control under diverse wing defects.

The issue of overshoot, particularly with the 3L-DOB controller in Wing Set 2,

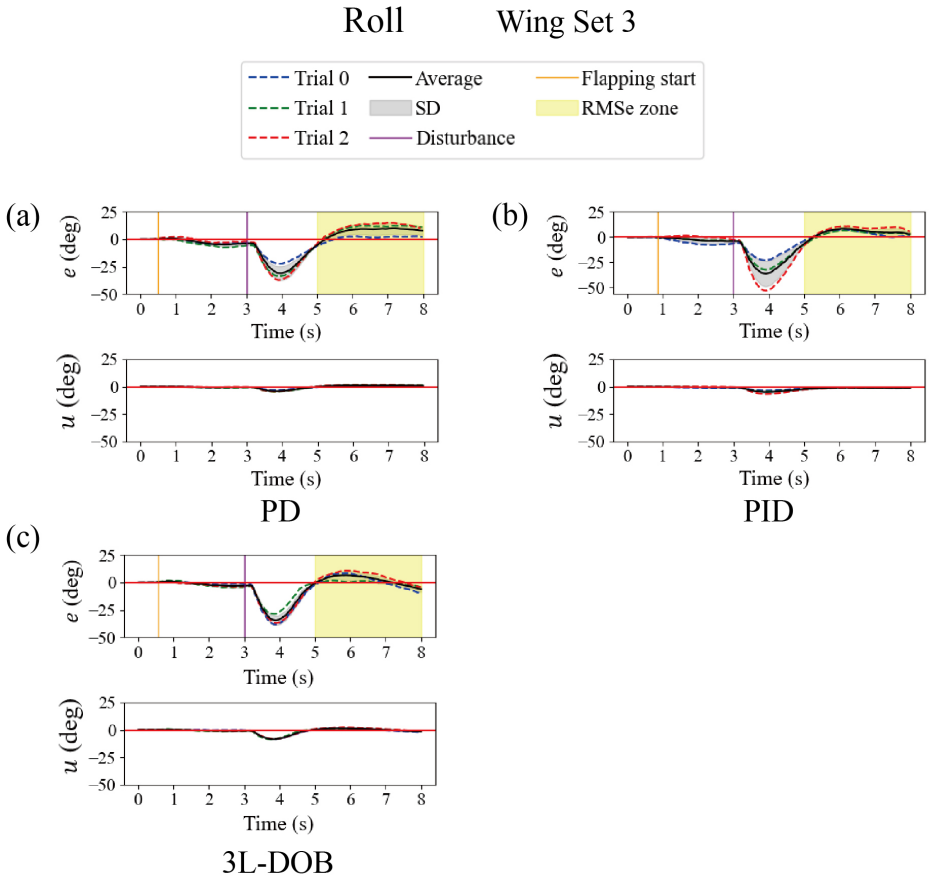

Figure 4.16 Attitude error e and control input u in roll experiments with Wing Set 3. PD controller (a), PID controller (b), and 3L-DOB controller (c).

brings to light the nuanced challenge of balancing responsiveness with stability in roll control. While the PD and PID controllers exhibited minimal overshoot across all conditions, the 3L-DOB controller's increased overshoot in the asymmetrical wing defect indicates a potential area for optimization, emphasizing the need for enhanced damping mechanisms or control strategies to mitigate such instabilities.

D. Practicable application

Active control is necessary to maintain stable hovering even without disturbance. Without control, fabrication error of the mechanism and wings caused notable yaw rotation and the wing defect caused roll rotation as shown in Figure

Table 4.4 Means and standard deviations of the recovery rates, RMS errors, and overshoot for three measurements in roll experiments. Pooled mean and its standard deviation for the mean values were also shown.

		PD	PID	3L-DOB
Recovery rate (deg/s)	Wing Set 1	23.5 (100%) ± 1.0	23.9 (100%) ± 1.6	26.9 (100%) ± 5.4
	Wing Set 2	-	23.5 (98%) ± 2.5	31.6 (117%) ± 6.5
	Wing Set 3	19.8 (84%) ± 4.3	22.9 (96%) ± 7.9	27.4 (102%) ± 4.5
	Pooled mean*	-	23.4	28.6
	Pooled s.d.*	-	0.4	2.1
RMS error (deg)	Wing Set 1	6.3 (100%) ± 1.1	1.9 (100%) ± 1.0	1.5 (100%) ± 0.7
	Wing Set 2	-	9.4 (495%) ± 0.8	7.0 (467%) ± 2.9
	Wing Set 3	7.8 (124%) ± 4.0	5.2 (274%) ± 2.0	4.0 (267%) ± 2.1
	Pooled mean*	-	5.5	4.2
	Pooled s.d.*	-	3.1	2.3
Overshoot (deg) **	Wing Set 1	-	-	1.5 (100%) ± 0.6
	Wing Set 2	-	-	9.8 (534%) ± 3.2
	Wing Set 3	-	-	4.2 (288%) ± 1.7
	Pooled mean*	-	-	5.2
	Pooled s.d.*	-	-	3.5

*Calculated from the mean values for Wing Sets 1 to 3.

**The symbol '-' means that the measurement or calculation was not possible.

4.7 (a, b, f). The 3L-DOB controller and the PID controller successfully supressed those yaw and roll rotation. For the sudden disturbance such as collision in our experiments, recovery time would be 1 to 2 seconds. Thus, sufficient altitude for dropping for 1 to 2 seconds would be necessary, that could be acceptable for many applications. For example, a palm-sized flapping-wing robot takes 2 to 3 seconds to recover from the 2 m/s wind disturbance [47]. However, for applications

requiring quicker response or low altitude, shorter recovery time would be necessary.

Due to the limitation of semi-tethered experimental setup, the direct applicability of the control parameters derived from this study to practical application remains uncertain. In addition, yaw, pitch, and roll control are separately investigated in this study, possibly requiring a further investigation on multi-axis control for practical application. While the 3L-DOB controller theoretically supports multi-axis control, practical implementation for full three-dimensional flight introduces several complexities. These include increased computational demands, the necessity for advanced sensor systems to precisely monitor three-dimensional movements, and the management of cross-axis interactions which could affect control fidelity. These challenges will be addressed in future work. Nevertheless, the results obtained from this study can serve as a reference for parameter identification in free-flight experiments that do not involve a gimbal, potentially reducing the requisite number of flight tests and narrowing down the parameter search space. A similar study using gimbal experiments was discussed by Shimura *et al.* [75].

Future research will focus on refining the controller's performance through algorithmic improvements, more efficient computational methods, and hardware advancements. Moreover, the performance of multi-axis control is expected to be investigated and the electronics are expected to be integrated onboard for untethered experiments.

4.3 Summary

This chapter introduced the implementation and evaluation of the 3L-DOB attitude controller. This controller was designed based on a three-loop feedback structure and incorporated an adaptive term derived from a disturbance observer to improve the responsiveness, accuracy, and robustness of the robot. It calculated the real-time attitude angle by fusing the data collected from an onboard 9-axis IMU sensor, the control output was sent to the control mechanism to achieve attitude control.

The performance of the controller was evaluated by flying with three Wing Sets that have different wing area loss through semi-tethered experiments using a gimbal mechanism, with external disturbances applied through an extra servo motor. The

results revealed that the 3L-DOB controller not only successfully recovered from the external disturbances and maintained the target attitude across all motions with all Wing Sets, but also surpassed conventional PD and PID controllers in terms of responsiveness and accuracy, demonstrating its robustness to wing area loss.

Chapter 5
Conclusions and future prospects

5.1 Conclusions

A hummingbird-mimetic flapping-wing aerial robot equipped with a 3L-DOB attitude controller was developed, with primary goals to increase the lift capacity and enhance the responsiveness, accuracy, and robustness of the robot when encountering potential changes in dynamic configuration. It has a weight of 17.5 g and a wingspan of 185 mm. The development of the robot began with the design of a rack-pinion-based flapping mechanism, noted for its lightweight and compactness, capable of achieving a large flapping amplitude. Subsequent efforts centered on the creation of a biomimetic wing, featuring an elastic connecting membrane that is crucial for softly limiting passive feathering, thereby increasing lift and efficacy. Following that, the control mechanism was designed, incorporating three servo motors and a 3D printed body frame. These servo motors are tasked with adjusting wing tension and the neutral positions of wing torsion, thereby facilitating the generation of control torques for roll, pitch, and yaw motions. The last step was the implementation and evaluation of a 3L-DOB attitude controller that features a three-loop feedback structure and an adaptive term, enabling the robot to recover from external disturbances and maintain at the target attitude across various body configurations without retuning the feedback gains.

5.1.1 Major findings and contributions

The major contributions of this study are summed as follows:

Development of the rack-pinion-based flapping mechanism paired with a dual-layer planetary gear reducer. A major contribution of this work was the creation of the flapping mechanism based on rack-pinion mechanism and the implementation of a dual-layer planetary gear reducer. This mechanism, characterized by its lightweight, compactness, and reliability, successfully achieved a flapping amplitude of 158°, contributing to the enhanced flight capabilities of the robot.

Development of the biomimetic wing integrated with an elastic connecting membrane. The connecting membrane, an extended elastomeric section located at the root of the wing, was designed to softly limit passive feathering. It effectively augmented wing torsion by curbing feathering in the wing root chord while promoting feathering in the wing tip chord during the mid-stroke, in comparison to a conventional rigid stopper that stops the feathering rotation around the spanwise axis rigidly. Integration of the connecting membrane resulted in a notable improvement in aerodynamic performance, with the biomimetic wing achieving

24.2% higher efficacy and 8.4% higher lift at 24 Hz compared to wings using conventional rigid stoppers. Additionally, the chordwise root shaft of the wing played a crucial role in damping the vibrations of the connecting membrane at the end of each stroke, contributing to the overall stability and efficiency of the wing's motion.

Development of the control mechanism based on wing modulation. A mechanism composed of three servo motors integrated into a 3D printed body frame was developed for attitude control. These servo motors manipulate the wing root bars to modulate the tension of the wing membranes and the neutral positions of wing torsion, enabling the robot to produce control torques around its CoG for roll, pitch, and yaw movements. Performance of the control mechanism was evaluated by mounting the robot on a 6-axis load cell, the results revealed that it produced a maximum roll, pitch, and yaw torques of 1.2 Nmm, 1.2 Nmm, and 1.3 Nmm respectively at the flapping frequency of 20 Hz. The produced torques scale linearly with increasing rotation angles of the wing root bars, demonstrating the mechanism's effectiveness in modulating wing tension and torsion to generate the necessary control torques for stable and controlled flight.

Development of the 3L-DOB attitude controller to enhance robustness of the robot. A major contribution of this research was the development of the attitude controller, which employs a three-loop feedback structure. An adaptive term derived from a disturbance observer was incorporated to enhance the responsiveness, accuracy, and robustness of the controller, enabling the robot to effectively counter against the external disturbances and maintain precise control, even when experiencing alterations in its body configuration, (i.e., wing area loss). The controller's performance was evaluated through semi-tethered experiments using a gimbal mechanism. The external disturbance was generated using an extra servo motor to give an initial rotation moment around the motion axis, thereby displacing the robot from its initial orientation. The results demonstrated the 3L-DOB attitude controller's capability in countering against disturbances and maintaining stability, surpassing the performance of conventional PD and PID controllers. This superiority was consistent across all Wing Sets that feature both asymmetrical and symmetrical wing area loss, demonstrating the controller's robustness with different body configurations.

5.1.2 Implications of this research

The implications of this research are extensive and diverse:

Enhanced operational capabilities of flapping-wing aerial robots: The findings from this research have direct applications in enhancing the operational capabilities of flapping-wing aerial robots, particularly in challenging environments like confined indoor spaces or intricate outdoor areas. The increase in lift capacity opens new possibilities for expanded onboard functionalities, for instance, a larger battery or extra sensors could be integrated, thereby broadening the robot's operational scope and utility. Furthermore, the 3L-DOB controller plays an important role in countering against external disturbances and stabilizing the robot in complex operation environments. This contributes to safer and more reliable operations, enhancing the robot's performance and robustness in diverse operational scenarios.

Contribution to the field of robotics: This research makes contributions to the field of robotics, particularly in its detailed exploration and implementation of biomimetic design principles and feedback control strategies. It exemplifies the potential benefits of incorporating biological concepts into robotic design, demonstrating how these principles can lead to significant enhancements in performance and efficiency of robotic systems. This work bridges the gap between biological inspiration and practical robotic applications, setting a reference for future innovations in the field.

Broader applications: The findings presented in this research not only have implications in the realm of robotics, but also provide contributions to the fields of biomimetics and biology. The technologies and methodologies developed in this research have the potential for diverse applications across multiple sectors. They could be particularly impactful in areas such as surveillance, where discreet and agile observation is crucial, and in environmental monitoring, where precise and flexible data collection is needed. Additionally, these advancements hold promise for the entertainment industry, offering new avenues for creating engaging and interactive experiences. The cross-disciplinary applicability of this research underscores its significance and the broad scope of its potential impact.

In summary, this thesis represents a step forward in the exploration of bio-inspired flapping-wing aerial robots, blending principles of biomimetics with practical robotic applications. The development of the hummingbird-mimetic flapping-wing aerial robot, equipped with a 3L-DOB attitude controller, brings new

possibilities into the domains of robotics and biomimetics. The discoveries and methodologies developed in this work serve as new references for future innovations and applications, highlighting the endless possibilities that lie at the intersection of nature-inspired design and engineering excellence. The journey of discovery and innovation continues, with this research contributing a valuable chapter to the ever-evolving narrative of biomimetic robotics.

5.2 Future prospects

5.2.1 Advancements in materials

Evolving materials for wing and mechanism: Future iterations of the flapping-wing aerial robots could significantly benefit from advancements in material science. Lightweight and durable materials like carbon fiber composites and advanced polymers could replace current components, offering substantial improvements in flight efficiency and durability. These materials could further reduce the overall weight of the robot, allowing for extended flight durations and less energy consumption.

Exploration of bio-inspired materials: Investigating bio-inspired materials that mimic the properties of hummingbird feathers and insect exoskeletons could lead to wings that are not only lightweight but also capable of self-repair [79] or environmental adaptability. This approach can pave the way for robots that are more resilient to environmental factors such as humidity or temperature fluctuations.

5.2.2 Control system optimization

AI and machine learning for flight control: The incorporation of machine learning algorithms into the robot's control system presents an exciting avenue for research [80]. By training these systems with vast datasets on flight patterns and environmental interactions, the robot could autonomously adapt to new situations, improving its responsiveness and decision-making in complex scenarios.

Advanced sensory integration: Enhancing the robot with sophisticated sensors, such as advanced optical flow sensors with small size and light weight, could significantly improve its perception of the environment. This integration would allow the robot to navigate more effectively in cluttered or dynamic spaces, increasing its applicability in tasks like search and rescue or environmental monitoring.

5.2.3 Expanded application scenarios

Aquatic applications: Given the robot's biomimetic design, exploring adaptations for aquatic environments could open new research and application possibilities. Modifications like waterproofing and buoyant materials could enable the robot to operate in both aerial and aquatic settings, making it valuable for marine biological studies or underwater infrastructure inspection [81].

Collaboration with IoT devices: Integrating the robot with IoT (Internet of Things) devices could create a networked system capable of performing complex tasks. For instance, a swarm of these robots could work in concert with ground-based sensors for large-scale environmental monitoring, agricultural management, or coordinated search operations.

5.2.4 Integration with other technologies

Renewable energy sources: Exploring the integration of renewable energy sources, such as miniature solar panels [82], could extend the operational time and reduce the carbon footprint of the robot. This adaptation would be particularly advantageous for long-duration missions like wildlife tracking or continuous environmental monitoring.

5.2.5 Investigate the performance with wind disturbance

This study primarily investigated the performance of tested controllers with the impact of wing area loss. However, it is essential to acknowledge that wind disturbances also play a significant role in practical applications. Studies such as those by Shimura *et al*. [75] and Lee *et al*. [47] have demonstrated that wind disturbances can result in RMS errors up to 15 degrees and recovery times up to 3 seconds. This highlights the importance of considering environmental factors that our robot may encounter in real-world scenarios.

Moving forward, this research will expand to include investigations into the effects of wind disturbances. By exploring both types of disturbances, structural (wing area loss) and environmental (wind), we aim to develop a more robust and adaptable flapping-wing robot. This dual approach will ensure that our robot can maintain optimal performance and stability under a variety of challenging conditions, thereby enhancing its practical applicability in diverse environments.

These prospects highlight the dynamic and evolving nature of research in biomimetic flapping-wing aerial robots. By building on the foundational work presented in this thesis, subsequent studies can push the boundaries of what is

currently possible, leading to robots that are not only more efficient and versatile but also more harmonious with the environments they are designed to operate in. The journey of innovation and discovery in biomimetic robotics is ongoing, and the potential applications and advancements are as boundless as the natural world that inspires them.

Reference

[1] Warrick, D., Hedrick, T., Fernández, J.M., Biewener, A., 2012. Hummingbird flight. Current Biology. doi: 10.1016/j.cub.2012.04.057.

[2] Hedrick, T.L., Tobalske, B.W., Ros, I.G., Warrick, D.R., Biewener, A.A., 2012. Morphological and kinematic basis of the hummingbird flight stroke: Scaling of flight muscle transmission ratio. Proceedings of the Royal Society B: Biological Sciences 279, 1986–1992. doi:10.1098/rspb.2011.2238.

[3] Song, J., Luo, H., Hedrick, T.L., 2015. Wing-pitching mechanism of hovering Ruby-throated hummingbirds. Bioinspiration and Biomimetics 10. doi:10.1088/1748-3190/10/1/016007.

[4] Wells, D.J., 1993. Muscle Performance in Hovering Hummingbirds. Journal of Experimental Biology 178, 39–57. doi:10.1242/jeb.178.1.39.

[5] Ingersoll, R., Lentink, D., 2018. How the hummingbird wingbeat is tuned for efficient hovering. Journal of Experimental Biology 221. doi:10.1242/jeb.178228.

[6] Warrick, D.R., Tobalske, B.W., Powers, D.R., 2009. Lift production in the hovering hummingbird. Proceedings of the Royal Society B: Biological Sciences 276, 3747–3752. doi:10.1098/rspb.2009.1003.

[7] Epting, R.J., 1980. Functional Dependence of the Power for Hovering on Wing Disc Loading in Hummingbirds. Physiological Zoology 53, 347–357. doi:10.1086/physzool.53.4.30157873.

[8] Weis-Fogh, T., 1972. Energetics of Hovering Flight in Hummingbirds and in Drosophila. Journal of Experimental Biology 56, 79–104. doi:10.1242/jeb.56.1.79.

[9] Warrick, D.R., Tobalske, B.W., Powers, D.R., 2005. Aerodynamics of the hovering hummingbird. Nature 435, 1094–1097. doi:10.1038/nature03647.

[10] Altshuler, D.L., Dudley, R., Ellington, C.P., 2004. Aerodynamic forces of revolving hummingbird wings and wing models. Journal of Zoology 264, 327–332. doi:10.1017/S0952836904005813.

[11] Michelson, R.C., 2004. Novel approaches to miniature flight platforms. Proceedings of the Institution of Mechanical Engineers, Part G: Journal of Aerospace Engineering 218, 363–373. doi:10.1243/0954410042794911.

[12] Michelson, R.C., 2002. The Entomopter, in: Neurotechnology for Biomimetic Robots. The MIT Press, pp. 481–510. doi:10.7551/mitpress/4962.003.0036.

[13] Zdunich, P., Bilyk, D., MacMaster, M., Loewen, D., DeLaurier, J., Kornbluh, R., Low, T., Stanford, S., Holeman, D., 2007. Development and testing of the mentor flapping-wing micro air vehicle. Journal of Aircraft 44, 1701–1711. doi:10.2514/1.28463.

[14] Wood, R.J., 2007. Liftoff of a 60mg flapping-wing MAV, in: IEEE International Conference on Intelligent Robots and Systems. pp. 1889–1894. doi:10.1109/IROS.2007.4399502.

[15] De Croon, G.C., de Clercq, K., Ruijsink, R., Remes, B., De Wagter, C., 2009. Design, Aerodynamics, and Vision-Based Control of the DelFly. International Journal of Micro Air Vehicles 1, 71–97. doi:10.1260/175682909789498288.

[16] Keennon, M., Klingebiel, K., Won, H., Andriukov, A., 2012. Development of the nano hummingbird: A tailless flapping Wing Micro Air Vehicle, in: 50th AIAA Aerospace Sciences Meeting Including the New Horizons Forum and Aerospace Exposition. doi:10.2514/6.2012-588.

[17] De Croon, G.C., Groen, M.A., De Wagter, C., Remes, B., Ruijsink, R., Van Oudheusden, B.W.H.E., 2012. Design, aerodynamics and autonomy of the DelFly. Bioinspiration and Biomimetics 7. doi:10.1088/1748-3182/7/2/025003.

[18] De Croon, G.C., Perçin, M., Remes, B., Ruijsink, R., De Wagter, C., 2015. The delfly: Design, aerodynamics, and artificial intelligence of a flapping wing robot, The DelFly: Design, Aerodynamics, and Artificial Intelligence of a Flapping Wing Robot. Springer Netherlands. doi:10.1007/978-94-017-9208-0.

[19] Karasek, M., Muijres, F.T., Remes, B., De Croon, G.C., 2018. A tailless aerial robotic flapper reveals that flies use torque coupling in rapid banked turns. Science 361, 1089–1094. doi:10.1126/science.aat0350.

[20] Phan, H.V., Kang, T., Park, H.C., 2017. Design and stable flight of a 21 g insect-like tailless flapping wing micro air vehicle with angular rates feedback control. Bioinspiration and Biomimetics 12. doi:10.1088/1748-3190/aa65db.

[21] Phan, H.V., Aurecianus, S., Kang, T., Park, H.C., 2019. KUBeetle-S: An insect-like, tailless, hover-capable robot that can fly with a low-torque control mechanism. International Journal of Micro Air Vehicles 11. doi:10.1177/1756829319861371.

[22] Tu, Z., Fei, F., Zhang, J., Deng, X., 2020. An at-scale tailless flapping-wing hummingbird robot. I. Design, optimization, and experimental validation. IEEE Transactions on Robotics 36, 1511–1525. doi:10.1109/TRO.2020.2993217.

[23] Tu, Z., Fei, F., Deng, X., 2020. Untethered Flight of an At-Scale Dual-Motor Hummingbird Robot with Bio-Inspired Decoupled Wings. IEEE Robotics and Automation Letters 5, 4194–4201. doi:10.1109/LRA.2020.2974717.

[24] Fei, F., Tu, Z., Zhang, J., Deng, X., 2019. Learning extreme hummingbird maneuvers on flapping wing robots, in: Proceedings - IEEE International Conference on Robotics and Automation. Institute of Electrical and Electronics Engineers Inc., pp. 109–115. doi:10.1109/ICRA.2019.8794100.

[25] Roshanbin, A., Altartouri, H., Karásek, M., Preumont, A., 2017. COLIBRI: A hovering flapping twin-wing robot. International Journal of Micro Air Vehicles 9, 270–282. doi:10.1177/1756829317695563.

[26] Coleman, D., Benedict, M., Hrishikeshavan, V., Chopra, I., 2015. Design, development and flight-testing of a robotic hummingbird, in: Annual Forum Proceedings - AHS International. American Helicopter Society, pp. 132–149.

[27] Ma, K.Y., Chirarattananon, P., Fuller, S., Wood, R.J., 2013. Controlled flight of a biologically inspired, insect-scale robot. Science 340, 603–607. doi:10.1126/science.1231806.

[28] Nguyen, Q.V., Chan, W.L., 2019. Development and flight performance of a biologically-inspired tailless flapping-wing micro air vehicle with wing stroke plane modulation. Bioinspiration and Biomimetics. 2019;14. doi: 10.1088/1748-3190/aaefa0.

[29] Phan, H.V., Park, H.C., 2016. Generation of Control Moments in an Insect-like Tailless Flapping-wing Micro Air Vehicle by Changing the Stroke-plane Angle. Journal of Bionic Engineering 13, 449–457. doi:10.1016/S1672-6529(16)60318-9.

[30] Chan, W.L., Nguyen, Q.V., Debiasi, M., 2014. Pitch and yaw control of tailless flapping wing MAVs by implementing wing root angle deflection. Proceedings of International Micro Air Vehicle Conference and Competition; 2014.

[31] Ding, L., Wang, F., Yan, J., Zhao, J., 2022. Experimental optimization of wing lift for a hummingbird-like micro flapping-wing robot, in: 2022 IEEE International Conference on Mechatronics and Automation, ICMA 2022.

Institute of Electrical and Electronics Engineers Inc., pp. 1239–1244. doi:10.1109/ICMA54519.2022.9856237.

[32] Olejnik, D.A., Muijres, F.T., Karásek, M., Honfi Camilo, L., De Wagter, C., De Croon, G.C., 2022. Flying Into the Wind: Insects and Bio-Inspired Micro-Air-Vehicles With a Wing-Stroke Dihedral Steer Passively Into Wind-Gusts. Frontiers in Robotics and AI 9. doi:10.3389/frobt.2022.820363.

[33] Verboom, J.L., Tijmons, S., De Wagter, C., Remes, B., 2015. Attitude and altitude estimation and control on obard a flapping wing micro air vehicle. Proceedings of IEEE International Conference on Robotics and Automation; 2015. p. 5846–5851.

[34] Roshanbin, A., Preumont, A., 2019. Yaw control torque generation for a hovering robotic hummingbird. International Journal of Advanced Robotic Systems 16. doi:10.1177/1729881418823968.

[35] Tijmons, S., De Croon, G.C., Remes, B., De Wagter, C., Ruijsink, R., Chu, Q., 2013. Stereo Vision Based Obstacle Avoidance on Flapping Wing MAVs, in: Advances in Aerospace Guidance, Navigation and Control. Springer Berlin Heidelberg, pp. 463–482. doi:10.1007/978-3-642-38253-6_28.

[36] Duhamel, P.E.J., Pérez-Arancibia, N.O., Barrows, G.L., Wood, R.J., 2012. Altitude feedback control of a flapping-wing microrobot using an on-board biologically inspired optical flow sensor, in: Proceedings - IEEE International Conference on Robotics and Automation. Institute of Electrical and Electronics Engineers Inc., pp. 4228–4235. doi:10.1109/ICRA.2012.6225313.

[37] De Wagter, C., Tijmons, S., Remes, B., De Croon, G.C., 2014. Autonomous flight of a 20-gram Flapping Wing MAV with a 4-gram onboard stereo vision system, in: Proceedings - IEEE International Conference on Robotics and Automation. Institute of Electrical and Electronics Engineers Inc., pp. 4982–4987. doi:10.1109/ICRA.2014.6907589.

[38] Bermudez, F.G., Fearing, R., 2009. Optical flow on a flapping wing robot, in: 2009 IEEE/RSJ International Conference on Intelligent Robots and Systems, IROS 2009. pp. 5027–5032. doi:10.1109/IROS.2009.5354337.

[39] Kitamura, I., Tanaka, H., Maeda, M., Liu, H., 2015. Assessing aerodynamic performance of hummingbird-inspired flapping system, in: 27th Bioengineering Conference of Japan Society of Mechanical Engineers.

[40] Tanaka, H., Suzuki, H., Kitamura, I., Maeda, M., Liu, H., 2013. Lift generation

of hummingbird wing models with flexible loosened membranes, in: IEEE International Conference on Intelligent Robots and Systems. pp. 3777–3783. doi:10.1109/IROS.2013.6696896.

[41] Park, H., Bae, G., Kim, I., Kim, S., Oh, H., 2023. Development of flapping wing robot and vision-based obstacle avoidance strategy. PeerJ Computer Science 9, e1201. doi:10.7717/peerj-cs.1201.

[42] He, W., Yan, Z., Sun, C., Chen, Y., 2017. Adaptive Neural Network Control of a Flapping Wing Micro Aerial Vehicle with Disturbance Observer. IEEE Transactions on Cybernetics 47, 3452–3465. doi:10.1109/TCYB.2017.2720801.

[43] Cheng, B., Deng, X., 2012. A neural adaptive controller in flapping flight. Journal of Robotics and Mechatronics 24, 602–611. doi:10.20965/jrm.2012.p0602.

[44] Mou, J., Zhang, W., Wu, C., Guo, Q., 2022. Adaptive Control of Flapping-Wing Micro Aerial Vehicle with Coupled Dynamics and Unknown Model Parameters. Applied Sciences (Switzerland) 12. doi:10.3390/app12189104.

[45] Chirarattananon, P., Ma, K.Y., Wood, R.J., 2014. Adaptive control of a millimeter-scale flapping-wing robot. Bioinspiration and Biomimetics 9. doi:10.1088/1748-3182/9/2/025004.

[46] Chand, A.N., Kawanishi, M., Narikiyo, T., 2016. Adaptive pole placement pitch angle control of a flapping-wing flying robot. Advanced Robotics 30, 1039–1049. doi:10.1080/01691864.2016.1196609.

[47] Lee, J., Ryu, S., Kim, H.J., 2020. Stable Flight of a Flapping-Wing Micro Air Vehicle under Wind Disturbance. IEEE Robotics and Automation Letters 5, 5685–5692. doi:10.1109/LRA.2020.3009064.

[48] Tu, Z., Fei, F., Liu, L., Zhou, Y., Deng, X., 2021. Flying with Damaged Wings: The Effect on Flight Capacity and Bio-Inspired Coping Strategies of a Flapping Wing Robot. IEEE Robotics and Automation Letters 6, 2114–2121. doi:10.1109/LRA.2021.3059626.

[49] Maeda, M., Nakata, T., Kitamura, I., Tanaka, H., Liu, H., 2017. Quantifying the dynamic wing morphing of hovering hummingbird. Royal Society Open Science 4. doi:10.1098/rsos.170307.

[50] Ishihara, D., Yamashita, Y., Horie, T., Yoshida, S., Niho, T., 2009. Passive maintenance of high angle of attack and its lift generation during flapping

translation in crane fly wing. Journal of Experimental Biology 212, 3882–3891. doi:10.1242/jeb.030684.

[51] Wu, P., Stanford, B.K., Sällström, E., Ukeiley, L., Ifju, P.G., 2011. Structural dynamics and aerodynamics measurements of biologically inspired flexible flapping wings. Bioinspiration and Biomimetics 6. doi:10.1088/1748-3182/6/1/016009.

[52] Nan, Y., Karásek, M., Lalami, M., Preumont, A., 2017. Experimental optimization of wing shape for a hummingbird-like flapping wing micro air vehicle. Bioinspiration and Biomimetics 12. doi:10.1088/1748-3190/aa5c9e.

[53] Du, G., Sun, M., 2010. Effects of wing deformation on aerodynamic forces in hovering hoverflies. Journal of Experimental Biology 213, 2273–2283. doi:10.1242/jeb.040295.

[54] Nakata, T., Noda, R., Liu, H., 2018. Effect of twist, camber and spanwise bending on the aerodynamic performance of flapping wings. Journal of Biomechanical Science and Engineering 13. doi:10.1299/jbse.17-00618.

[55] Yang, S., Zhang, W., 2015. Numerical analysis of the three-dimensional aerodynamics of a hovering rufous hummingbird (Selasphorus rufus). Acta Mechanica Sinica/Lixue Xuebao 31, 931–943. doi:10.1007/s10409-015-0450-5.

[56] Mountcastle, A.M., Combes, S.A., 2013. Wing flexibility enhances load-lifting capacity in bumblebees. Proceedings of the Royal Society B: Biological Sciences 280. doi:10.1098/rspb.2013.0531.

[57] Fujii, T., Dang, J., Tanaka, H., 2023. Hummingbird-bat hybrid wing by 3-D printing, in: Proceedings - IEEE International Conference on Robotics and Automation. Institute of Electrical and Electronics Engineers Inc., pp. 3404–3410. doi:10.1109/ICRA48891.2023.10160819.

[58] Kawahara, A., Aizawa, M., Yamasaki, T., Tanaka, H., 2019. Fabrication of a hummingbird-mimetic flexible flapping wings. Proceedings of MHS; 2019.

[59] Phan, H.V., Nguyen, Q.V., Truong, Q.T., Van Truong, T., Park, H.C., Goo, N.S., Byun, D., Kim, M.J., 2012. Stable Vertical Takeoff of an Insect-Mimicking Flapping-Wing System Without Guide Implementing Inherent Pitching Stability. Journal of Bionic Engineering 9, 391–401. doi:10.1016/S1672-6529(11)60134-0.

[60] Roll, J.A., Bardroff, D.T., Deng, X., 2016. Mechanics of a scalable high

frequency flapping wing robotic platform capable of lift-off, in: Proceedings - IEEE International Conference on Robotics and Automation. Institute of Electrical and Electronics Engineers Inc., pp. 4664–4671. doi:10.1109/ICRA.2016.7487666.

[61] Zou, Y., Zhang, W., Zhang, Z., 2016. Liftoff of an Electromagnetically Driven Insect-Inspired Flapping-Wing Robot. IEEE Transactions on Robotics 32, 1285–1289. doi:10.1109/TRO.2016.2593449.

[62] Fei, F., Roll, J.A., Deng, X., 2015. Design principle of wing rotational hinge stiffness, in: Proceedings - IEEE International Conference on Robotics and Automation. Institute of Electrical and Electronics Engineers Inc., pp. 1049–1054. doi:10.1109/ICRA.2015.7139306.

[63] Ma, K.Y., Felton, S.M., Wood, R.J., 2012. Design, fabrication, and modeling of the split actuator microrobotic bee, in: IEEE International Conference on Intelligent Robots and Systems. pp. 1133–1140. doi:10.1109/IROS.2012.6386192.

[64] Phan, H.V., Park, H.C., 2018. Design and evaluation of a deformable wing configuration for economical hovering flight of an insect-like tailless flying robot, in: Bioinspiration and Biomimetics. Institute of Physics Publishing. doi:10.1088/1748-3190/aab313.

[65] Karásek, M., Hua, A., Nan, Y., Lalami, M., Preumont, A., 2014. Pitch and roll control mechanism for a hovering flapping wing MAV, in: International Journal of Micro Air Vehicles. Multi-Science Publishing Co. Ltd, pp. 253–264. doi:10.1260/1756-8293.6.4.253.

[66] Karásek, M., Nan, Y., Romanescu, I., Preumont, A., 2013. Pitch moment generation and measurement in a robotic hummingbird, in: International Journal of Micro Air Vehicles. pp. 299–309. doi:10.1260/1756-8293.5.4.299.

[67] Tanaka, H., Okada, H., Shimasue, Y., Liu, H., 2015. Flexible flapping wings with self-organized microwrinkles. Bioinspiration and Biomimetics 10. doi:10.1088/1748-3190/10/4/046005.

[68] Colmenares, D., Kania, R., Zhang, W., Sitti, M., 2020. Bio-inspired flexible twisting wings increase lift and efficiency of a flapping wing micro air vehicle. arXiv 2–9.

[69] Wagner, H.O., 1955. The Molt of Hummingbirds. The Auk. 72(3), 286–291, doi:10.2307/4081607.

[70] Achache, Y., Sapir, N., Elimelech, Y., 2018. Hovering hummingbird wing aerodynamics during the annual cycle. Ii. implications of wing feather moult. Royal Society Open Science 5. doi:10.1098/rsos.171766.

[71] Hiltonpond.org [Internet]. South California: Hilton Pond Center for Piedmont Natural History; Birds of a feather: Hummingbird molt. [cited 2021 Aug 10]. Available from: https://www.hiltonpond.org/ThisWeek210801.html.

[72] Dickinson, M.H., Lehmann, F.O., Sane, S.P., 1999. Wing rotation and the aerodynamic basis of insect right. Science 284, 1954–1960. doi:10.1126/science.284.5422.1954.

[73] Gong, D.H., Lee, D.W., Shin, S.J., Kim, S.Y., 2019. String-based flapping mechanism and modularized trailing edge control system for insect-type FWMAV. International Journal of Micro Air Vehicles 11. doi:10.1177/1756829319842547.

[74] Lee, C.H., He, S., Hong, J.H., 2020. Investigation on Physical Meaning of Three-loop Autopilot. International Journal of Control, Automation and Systems 18, 2709–2720. doi:10.1007/s12555-019-0434-5.

[75] Shimura, K., Aono, H., Kang, C., 2023. An Experimental Study on Response and Control of a Flapping-Wing Aerial Robot Under Wind Gusts. Journal of Bionic Engineering. doi:10.1007/s42235-023-00426-x.

[76] Dang, J., Fujii, T., Tanaka, H., 2023. Soft Limitation of Passive Feathering at Wing Root Improves Lift Generation Performance in Hummingbird-Mimetic Flapping Wings. Journal of Aero Aqua Bio-mechanisms. 2023;10:48-56. doi: 10.5226/jabmech.10.48.

[77] Chai, P., 1997. Hummingbird hovering energetics during moult of primary flight feathers. Journal of Experimental Biology 200, 1527–1536. doi:10.1242/jeb.200.10.1527.

[78] Ma, J., Li, P., Zheng, Z., 2018. Disturbance observer based dynamic surface flight control for an uncertain aircraft. Proceedings of the Institution of Mechanical Engineers, Part G: Journal of Aerospace Engineering 232, 729–744. doi:10.1177/0954410017691793.

[79] Qiu, X., Zhang, X., 2023. Self-healing polymers for soft actuators and robots. Journal of Polymer Science. doi:10.1002/pol.20230496.

[80] Goedhart, M.W., Van Kampeny, E.J., Armaniniz, S., De Visser, C., Chu, Q., 2018. Machine learning for flapping wing flight control, in: AIAA Information

Systems-AIAA Infotech at Aerospace, 2018. American Institute of Aeronautics and Astronautics Inc, AIAA. doi:10.2514/6.2018-2135.

[81] Chen, Y., Wang, H., Helbling, E., Jafferis, N., Zufferey, R., Ong, A., Ma, K., Gravish, N., Chirarattananon, P., Kovac, M., Wood, R.J., 2017. A biologically inspired, flapping-wing, hybrid aerial-aquatic microrobot. Science Robotics 2. doi:10.1126/scirobotics.aao5619.

[82] Zhang, W., Hu, C., 2016. Solar cell as wings of different sizes for flapping-wing micro air vehicles. International Journal of Micro Air Vehicles 8, 209–220. doi:10.1177/1756829316673849.

[83] Cheng, B., Tobalske, B., Powers, D., Hedrick, T., Wethington, S., Chiu, G., Deng, X., 2016. Flight mechanics and control of escape manoeuvres in hummingbirds. I. Flight kinematics. Journal of Experimental Biology 219, 3518–3531. doi:10.1242/jeb.137539.

[84] Li, Z., Suntharasantic, S., Bai, S., Chirarattananon, P., 2018. Aeromechanic models for flapping-wing robots with passive hinges in the presence of frontal winds. IEEE Access 6, 53890–53906. doi:10.1109/ACCESS.2018.2868066.

[85] Campolo, D., Azhar, M., Lau, G., Sitti, M., 2014. Can DC motors directly drive flapping wings at high frequency and large wing strokes? IEEE/ASME Trans. Mechatronics, vol. 19, no. 1, pp. 109–120. doi: 10.1109/TMECH.2012.2222432.

[86] Hines, L., Campolo, D., Sitti, M., 2014. Liftoff of a Motor-Driven, Flapping-Wing Microaerial Vehicle Capable of Resonance. IEEE Transactions on Robotics, vol. 30, no. 1, pp. 220-232. doi: 10.1109/TRO.2013.2280057.

[87] Zhang, J., Deng, X., 2016. Resonance principle for the design of flapping wing micro air vehicles. IEEE/RSJ International Conference on Intelligent Robots and Systems (IROS), Daejeon, Korea (South), pp. 2412-2418. doi: 10.1109/IROS.2016.7759376.

[88] Ravi, S., Crall, J., McNeilly, S., Gagliardi, S., Biewener, A., Combes, S., 2015. Hummingbird flight stability and control in freestream turbulent winds. Journal of Experimental Biology 218, 1444–1452. doi:10.1242/jeb.114553.

Publications

International journals

[1] Jinqiang Dang, Hwankyun You, Hiroto Tanaka, “An experimental study on attitude control of a tailless hummingbird-mimetic flapping-wing robot with defective wings,” Advanced Robotics, 2024.

[2] Jinqiang Dang, Tomoya Fujii, Hiroto Tanaka, “Soft limitation of passive feathering at wing root improves lift generation performance in hummingbird-mimetic flapping wings,” Journal of Aero Aqua Bio-mechanisms, Vol. 10, Issue 1, pp. 48–56, 2023, DOI: 10.5226/jabmech.10.48

International conferences

[1] Tomoya Fujii, Jinqiang Dang, Hiroto Tanaka, “Hummingbird-bat hybrid wing by 3-D printing,” IEEE International Conference on Robotics and Automation 2023 (ICRA 2023), pp. 3404–3410, 2023, DOI: 10.1109/ICRA48891.2023.10160819.

[2] Jinqiang Dang, Tomoya Fujii, Hiroto Tanaka, “Design of a hummingbird-mimetic flexible wing with elastic passive feathering rotation limitation structure,” Proceedings of the 8th International Symposium on Aero-aqua Bio-Mechanisms (ISABMEC 2022), pp. 97–100, 2022. (Student Award)

Domestic conferences

[1] 吉田颯, ダンジンシャン, 田中博人, “複数の風切羽で構成されるハチドリ規範羽ばたき翼,” 日本機械学会 2022 年度年次大会, J022-06, 2022.

[2] Jinqiang Dang, Hiroto Tanaka, “Study on a hummingbird-sized tailless flapping-wing aerial robot capable of pitch, roll and yaw control,” 2F1-03, 第 37 回日本ロボット学会学術講演会, 2019.

[3] Jinqiang Dang, Akio Kawahara, Hiroto Tanaka, “Design, fabrication, and test of a new control mechanism for a tailless flapping-wing aerial robot,” 1P1-F07,

ロボティクス・メカトロニクス講演会 2019, 2019.

Acknowledgement

First of all, I would like to express my deepest gratitude to my supervisor, Associate Professor Hiroto Tanaka, for the unwavering support and guidance throughout the journey of my PhD study. His insights and wisdom have been invaluable not only to my academic research but also to my personal growth. Professor Tanaka's expertise in biomimetics and biomechanics have been a constant source of inspiration and has fundamentally shaped the direction of my work. His patient mentorship and meticulous attention to detail have taught me the rigors of academic scholarship and the importance of perseverance. I am also profoundly thankful for the freedom he afforded me in exploring my research interests, while always being available for discussion and advice when I needed it most. His constructive criticism and encouragement have been instrumental in refining my work to its current form. Beyond academic guidance, I am grateful for the life lessons I have learned from him, which have prepared me to step into the future with confidence. His belief in my abilities and potential has been a significant motivator throughout my PhD journey. I am honored to have had him as my mentor and supervisor, and I hope that this thesis meets his expectations and stands as a testament to his profound impact on my academic career.

I extend my sincere thanks to the esteemed reviewers of my PhD study, whose expertise and insightful evaluations have significantly contributed to the enhancement of my thesis. I am grateful to Professor Suzumori, Professor Yamaura, Associate Professor Sugahara, and Associate Professor Miura for their thorough, insightful comments, and constructive critiques on my research work. Their engagement with my work and their willingness to share their valuable knowledge have not only improved the quality of my thesis but have also provided me with a clearer path for future research endeavors. Their challenging questions and suggestions have pushed me to sharpen my thinking and deepen my understanding of the subject matter. I appreciate the time and effort they have dedicated to reviewing my work, amidst their own demanding schedules.

I owe a debt of gratitude to my global mentor in the SSS (super smart society) project, Dr. Thomas Haustein, whose guidance has been a lighthouse in the voyage of my research. Our monthly meeting has not only been a cornerstone of my

progress but also a source of continuous learning and inspiration. His astute observations and invaluable feedback have been instrumental in navigating through the challenges encountered in my research. Even though in a different field, his expertise and practical advice have empowered me to overcome obstacles and refine my work to higher standards. I am especially grateful for the internship opportunity at Fraunhofer HHI in Berlin, Germany. This experience has been a significant milestone in my PhD journey, offering a platform to apply and expand my research skills in a world-renowned institution. The generosity of Thomas in sharing his time and wisdom is deeply appreciated. It has been an immense privilege to benefit from such dedicated mentorship, and I am inspired by the dedication he shows toward fostering the growth of an academic researcher.

My gratitude also goes out to my peers in the hummingbird group at Tanaka lab, whose camaraderie and collaborative spirit have been pivotal to my PhD journey. The synergy within the group, centered on related research topics, has fostered an environment of shared knowledge and mutual support that has been indispensable to my work. I am grateful for the significant contributions of Mr. Yoshida Hayato, Mr. Fujii Tomoya, and Mr. Hirotaka Kondo. Their outstanding work on the development of hummingbird-mimetic wings and the kinematics analysis of DC motors has been instrumental to this research. Their dedication and ingenuity have significantly enhanced the quality and scope of our collective research. I am also profoundly thankful for the contributions of Mr. Hwankyun You from KAIST, whose efforts in advancing the attitude control of our robot have been crucial. His technical expertise and commitment have played a vital role in the successes we have achieved. The journey towards completing my PhD has been made smoother and more enriching due to the help and encouragement of each member of our team. I am truly grateful for the spirit of collaboration that has underpinned our group's endeavors.

Above all, my deepest and most profound gratitude is reserved for my family. The past five years, marked by distance and the challenges of the pandemic, have undeniably been tough. Despite the miles that separated us and the time that has passed since our last meeting, their unwavering support and unconditional love have been the bedrock of my strength and perseverance. Their belief in me and their constant encouragement have been my guiding stars, lighting the path through the rigorous demands of PhD life. It is with their silent sacrifices and quiet fortitude in

mind that I have pursued my academic goals. Every milestone reached and every obstacle overcome is a testament to their immeasurable influence on my life. I am forever indebted to them for their patience, understanding, and for the countless ways they have supported me from afar. It is with the utmost love and appreciation that I dedicate the completion of my PhD journey to my dearest family.

Besides, I would like to express my sincere gratitude to the funding resources that have made my PhD study possible. The funding from the JSPS KAKENHI Grant-in-Aid for Scientific Research on Innovative Areas, which supported the "Science of Soft Robots" project, has been instrumental in the advancement of my research. I am also deeply thankful for the support from the Tokyo Tech Pioneering Doctoral Research Project, which has provided both financial backing and a platform for academic growth and exploration. This program has played a crucial role in shaping my research journey. Additionally, I wish to acknowledge the Tokyo Tech Academy for Super Smart Society for their support. The opportunities and resources they have provided have been invaluable in my pursuit of academic and professional excellence. The assistance and opportunities granted by these organizations have not only facilitated my research but have also greatly contributed to my personal and academic development. I am immensely grateful for their support.

In the final reflection of this PhD journey, I find myself overwhelmed with gratitude towards the myriad of individuals who have walked alongside me in this significant chapter of my life. Each person who has crossed my path during these formative years has left an indelible mark, contributing to both my professional growth and personal enrichment.

To every friend, colleague, mentor, and acquaintance who has offered support, shared wisdom, or simply been part of this journey, your impact has been immeasurable.

Your presence, in myriad ways, has enriched this experience, making it not just a scholarly pursuit, but a journey filled with learning, growth, and meaningful connections. It is with a deep sense of gratitude that I reflect on the contributions each one of you has made to my life during these years.

As this chapter of my life closes and another begins, I wish each of you a future filled with success, happiness, and fulfillment. May your paths be bright and your endeavors fruitful.

Thank you for being a part of my story.

2024.08
Dang Jinqiang

Appendix

A. Discussion on the natural frequency

Natural frequency is a critical consideration for flapping-wing robots, particularly those utilizing a motor direct-drive mechanism with a flexible rotation hinge (Figure A.1). In such systems, the flapping amplitude varies with frequency, and the maximum lift and angular velocity are achieved when operating at the natural frequency due to the benefits of flapping resonance [87]. These robots are typically smaller and lighter than our robot [14, 63, 81, 84–87].

Our robot, however, employs a different mechanism where the wing is driven not directly by the motor but through a pin-slot and rack-pinion mechanism. The flapping amplitude is fixed at 158°, and the components are made from PEEK using NC milling. This design results in a natural frequency significantly higher than our operational frequency range of 10–30Hz. Consequently, no resonance was observed at these operational frequencies for the wing attachment and passive rotation.

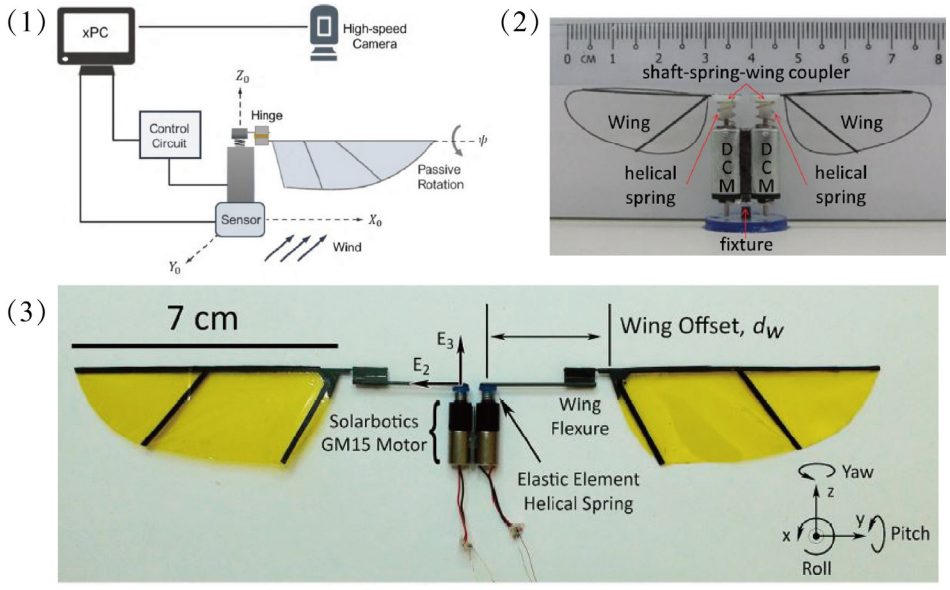

Figure A.1 Flapping-wing robots with a motor direct-drive mechanism: (1) Li *et al.* [84], (2) Campolo *et al.* [85], (3) Lindsey *et al.* [86].

B. Control mechanism of hummingbird

Hummingbirds control their attitude using rapid wing flapping, precise muscle control, and tail adjustments [1–3, 83]. Unlike most birds, hummingbirds can actively rotate their wings, allowing them to generate lift on both the upstroke and downstroke, providing exceptional control and maneuverability. By adjusting the angle of attack of their wings, they can control their pitch, roll, and yaw. Powerful pectoral muscles enable precise wing movements, while their tail acts as a stabilizer and control surface, making rapid adjustments for stability.

Although the flapping amplitude of our robot is fixed, differing from hummingbirds, we utilized a wing modulation method that can adjust the angle of attack of the left and right wings independently to generate pitch, roll, and yaw torques, similar to hummingbirds. Additionally, our biomimetic wings are inspired by hummingbird wings, mimicking their shape and flexural stiffness distribution [76].

C. Sequential snapshot of the semi-tethered experiment

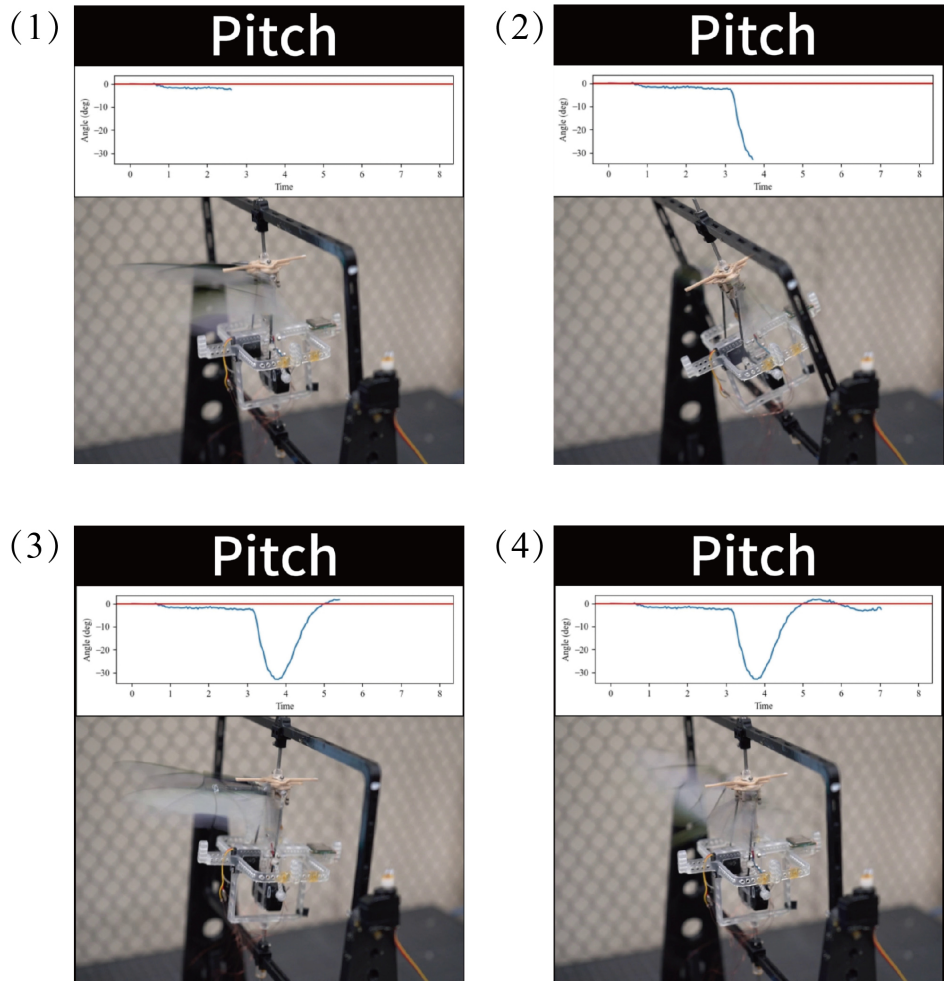

Figure C.1 Image sequence of pitch experiment with Wing Set 1 and 3L-DOB controller.

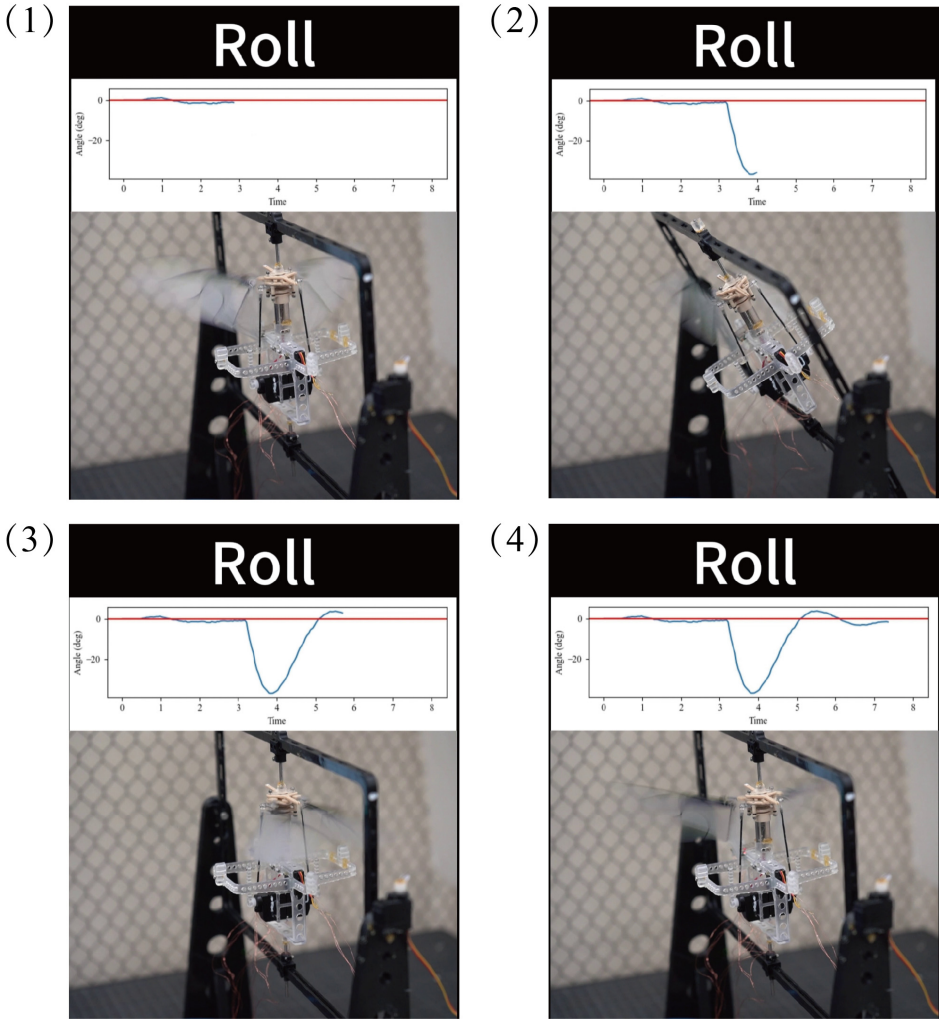

Figure C.2 Image sequence of roll experiment with Wing Set 1 and 3L-DOB controller.

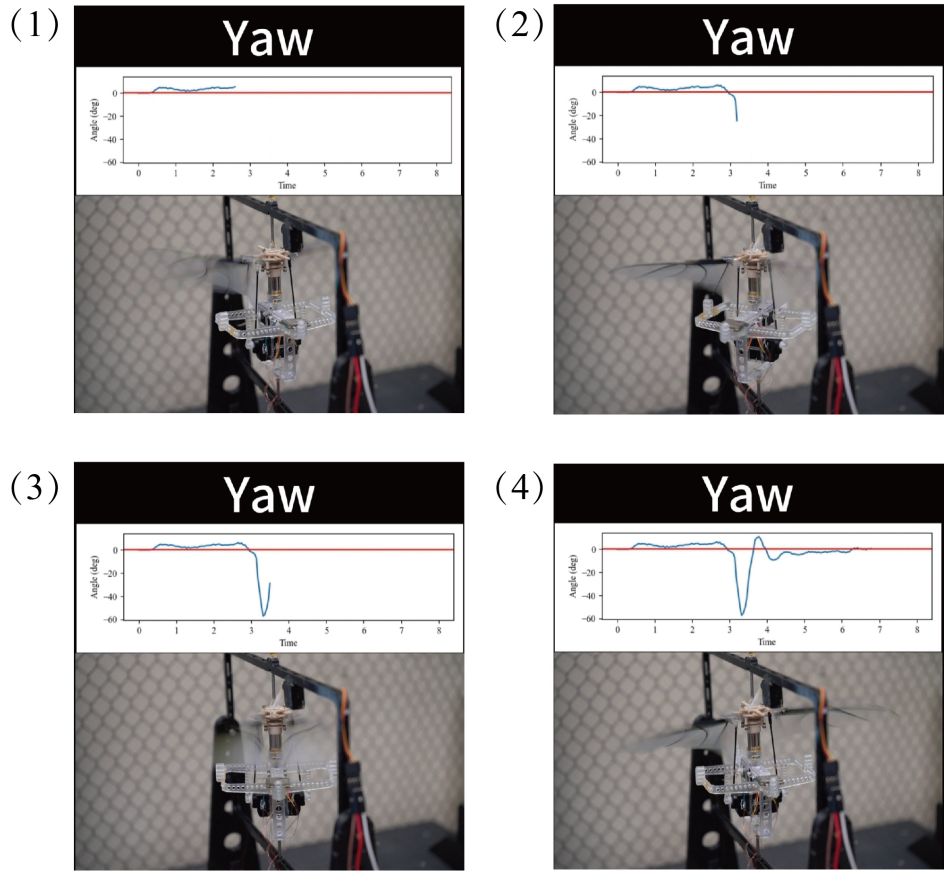

Figure C.3 Image sequence of yaw experiment with Wing Set 1 and 3L-DOB controller.

D. Comparison of lift and robustness with previous work

This study demonstrated a lift per area of 56.3 N/m^2 at the frequency of 25 Hz (Figure D.1), indicating an effective performance for the specific design and conditions. The Nano hummingbird achieved similar lift per area but required a higher frequency (30 Hz) to do so. The KUBeetle-S and Amazilia hummingbird exhibited lower lift per area under similar conditions.

The KUBeetle-S achieved the highest lift overall at 30 Hz, while this study and

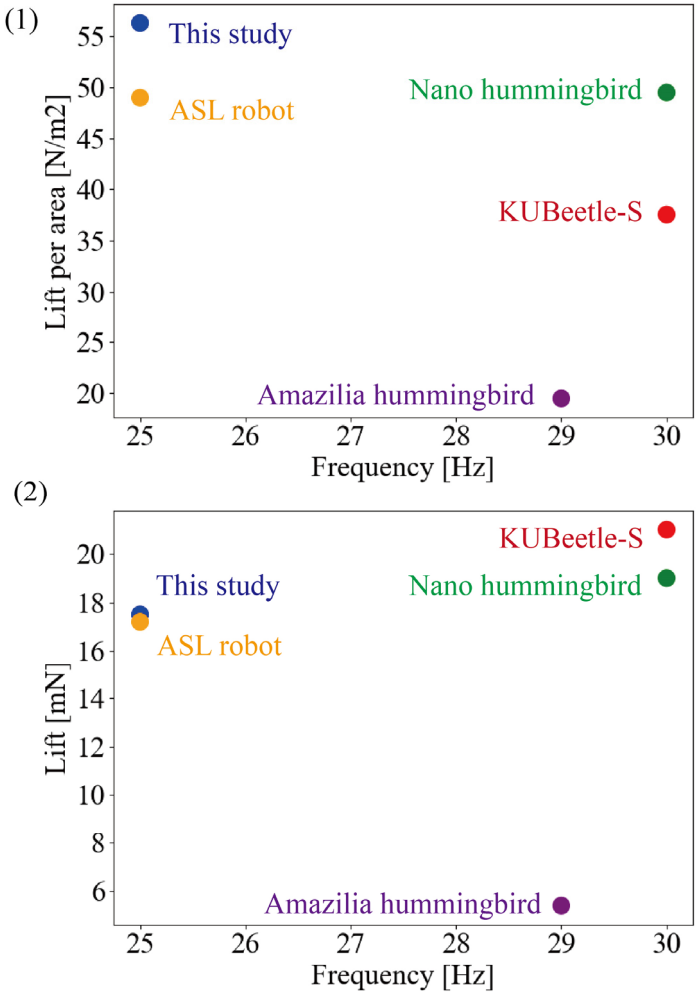

Figure D.1 Lift per area versus Frequency (1) and Lift versus Frequency (2) of this study, ASL robot [25], Nano hummingbird [16], KUBeetle-S [21], and Amazilia hummingbird [49].

Table D.1 A general comparison of robustness to disturbances in flapping-wing robots and hummingbird.

	Disturbance type	Disturbance level	RMS error [deg]	Recovery time [s]
This study	Wing area loss	7% / 14%	1–4	0.3–2
Deng *et al.* [48]	Wing area loss	5% / 10%	5–10	*
Shimura *et al.* [75]	Wind	< 1.5m/s	10–15	1.5–3
Lee *et al.* [47]	Wind	< 2m/s	2–4	2–3
Hummingbird [71, 88]	Wing area loss wind	22% < 11.2	*	0.1–0.5

the ASL robot showed comparable lift values at a lower frequency (25 Hz).

Overall, this study and the ASL robot showed effective performance at 25 Hz, with this study achieving higher lift per area. The KUBeetle-S, while operating at a higher frequency, achieved the highest lift, indicating a different performance characteristic. The Nano hummingbird balanced between these two performance metrics but at a higher operational frequency. The Amazilia hummingbird, with its lower lift and lift per area, provided a baseline for comparison.

Table D.1 provided a comparison of the robustness of various flapping-wing robots against different types of disturbances, specifically focusing on wing area loss and wind disturbances. The key metrics considered are the RMS error in degrees and the recovery time in seconds. This study showed low RMS errors (1–4 degrees) and quick recovery times (0.3–2 seconds) under wing area loss conditions. Deng *et al.* [48] reported higher RMS errors (5–10 degrees) but did not specify recovery times. The hummingbird had very rapid recovery times (0.1–0.5 seconds) for a significant wing area loss of 22% [71].

Lee *et al.* [47] demonstrated low RMS errors (2–4 degrees) and moderate recovery times (2–3 seconds) under wind disturbances. Shimura *et al*. [75], while handling slightly lower wind speeds (<1.5 m/s), had higher RMS errors (10–15 degrees) and longer recovery times (1.5–3 seconds). The hummingbird also showed rapid recovery times (0.1–0.5 seconds) under high wind conditions (<11.2 m/s) [88].

Overall, this study indicated effective performance in terms of both RMS error and recovery time under wing area loss conditions. For wind disturbances, Lee *et al.* managed to control RMS errors well, while the hummingbird consistently showed rapid recovery time under both disturbance types, suggesting a high level of robustness.